

PROPERTIES OF AURORAL KILOMETRIC RADIATION
FROM AN INTERFEROMETER ANALYSIS OF THE
ISEE-1 AND -2 PLASMA WAVE DATA

by

Mark Mason Baumbach

An Abstract

Of a thesis submitted in partial fulfillment
of the requirements for the Doctor of
Philosophy degree in Physics
in the Graduate College of
The University of Iowa

May 1986

Thesis supervisor: Professor Donald A. Gurnett
Professor Stanley D. Shawhan

ABSTRACT

The first satellite-satellite interferometry measurements of the auroral kilometric radiation (AKR) source region diameter are presented. By correlating the analog waveforms detected by ISEE-1 and ISEE-2, the size of the AKR source region is determined. Correlations have been measured at 125 and 250 kHz for projected baselines ranging from 20 to 3868 km.

High correlations are found at all projected baselines, with little or no tendency to decrease at long baselines. The correlation is lower for events with wide bandwidths than for events with narrow bandwidths. The magnitude of the correlation as a function of signal delay and the spectra of the individual bursts show that sometimes the bandwidth of AKR bursts varies rapidly and can be narrower than 20 Hz. The spectra observed by both spacecraft are nearly identical.

Correlation results are interpreted differently for incoherent radiation than for coherent radiation. If the radiation is incoherent, the visibility of the source region is the Fourier transform of the brightness distribution. Assuming incoherent radiation the average source region diameter for all analyzed bursts is less than 9.27 km. Source region diameters measured for individual bursts range from 1 to 16 km. Generation mechanisms that only amplify incoming radiation

cannot produce high correlations unless the source region diameter is smaller than 25 km. Such small source region diameters require growth rates that are too large to be explained by existing theories. This result strongly indicates that the radiation is coherent.

For coherent radiation, an upper limit to the source region diameter can be inferred from the angular width of the radiation pattern. The similarity of the spectra observed by both spacecraft indicates that the angular width of the radiation pattern for individual bursts is at least 2.5° . An angular width of 2.5° implies that the diameter of the brightness distribution is smaller than 20 km, but with refraction of the waves near the source region or from the plasmopause, the source region diameter could be as large as 100 km.

Abstract approved: Dale A. Gurnett
Thesis supervisor

Prof, Dept of Physics and Astronomy
Title and department

May 6, 1986
Date

PROPERTIES OF AURORAL KILOMETRIC RADIATION
FROM AN INTERFEROMETER ANALYSIS OF THE
ISEE-1 AND -2 PLASMA WAVE DATA

by

Mark Mason Baumbach

A thesis submitted in partial fulfillment
of the requirements for the Doctor of
Philosophy degree in Physics
in the Graduate College of
The University of Iowa

May 1986

Thesis supervisor: Professor Donald A. Gurnett
Professor Stanley D. Shawhan

Graduate College
The University of Iowa
Iowa City, Iowa

CERTIFICATE OF APPROVAL

PH.D. THESIS

This is to certify that the Ph.D. thesis of

Mark Mason Baumbach

has been approved by the Examining Committee
for the thesis requirement for the Doctor of
Philosophy degree in Physics at the May
1986 graduation.

Thesis committee:

Daniel A. Hummett
Thesis supervisor
Ronald Frank Vogel
Member
Christopher K. Gaj
Member
William R. Savage
Member
Dwight Nicholson
Member

ACKNOWLEDGMENTS

I wish to express my appreciation to the many people who have offered guidance and support during this project. I am grateful to Professors D. A. Gurnett and S. D. Shawhan for proposing this study and for their guidance and support throughout the project. Dr. W. Calvert is thanked for his stimulating discussions on Auroral Kilo-metric Radiation and for his encouragement during the course of this research. Dr. R. R. Anderson deserves a special acknowledgment. I have always been able to count on Dr. Anderson's help and support in any crisis. Dr. Anderson's help and friendship will never be forgotten. Dr. Wm. R. Savage is also thanked for the use of his spectrum analyzer and for help with interpreting the spectral data.

The preparation of a thesis requires the help of many people throughout the Physics Department. Mark Brown and John Birkbeck deserve mention for their work in preparing the figures for this thesis. R. Brechwald, T. Averkamp, and Wm. T. Robison are thanked for answering the many programming questions which arose. I also thank Kathy Kurth for her speed and efficiency in the typing of this manuscript.

Without the understanding, support, and encouragement from my parents and friends this research could not have been successfully completed.

This research was supported in part by the National Aeronautics and Space Administration under Contracts NAS5-26819 and NAS5-28701, Grants NAG5-118 NASA/HQ, NGL-16-001-002, and NGL-16-001-043 and by the Office of Naval Research under Grant N00014-85-K-0404.

ABSTRACT

The first satellite-satellite interferometry measurements of the auroral kilometric radiation (AKR) source region diameter are presented. By correlating the analog waveforms detected by ISEE-1 and ISEE-2, the size of the AKR source region is determined. Correlations have been measured at 125 and 250 kHz for projected baselines ranging from 20 to 3868 km.

High correlations are found at all projected baselines, with little or no tendency to decrease at long baselines. The correlation is lower for events with wide bandwidths than for events with narrow bandwidths. The magnitude of the correlation as a function of signal delay and the spectra of the individual bursts show that sometimes the bandwidth of AKR bursts varies rapidly and can be narrower than 20 Hz. The spectra observed by both spacecraft are nearly identical.

Correlation results are interpreted differently for incoherent radiation than for coherent radiation. If the radiation is incoherent, the visibility of the source region is the Fourier transform of the brightness distribution. Assuming incoherent radiation the average source region diameter for all analyzed bursts is less than 9.27 km. Source region diameters measured for individual bursts range from 1 to 16 km. Generation mechanisms that only amplify incoming radiation

cannot produce high correlations unless the source region diameter is smaller than 25 km. Such small source region diameters require growth rates that are too large to be explained by existing theories. This result strongly indicates that the radiation is coherent.

For coherent radiation, an upper limit to the source region diameter can be inferred from the angular width of the radiation pattern. The similarity of the spectra observed by both spacecraft indicates that the angular width of the radiation pattern for individual bursts is at least 2.5° . An angular width of 2.5° implies that the diameter of the brightness distribution is smaller than 20 km, but with refraction of the waves near the source region or from the plasmopause, the source region diameter could be as large as 100 km.

TABLE OF CONTENTS

	Page
LIST OF TABLES	viii
LIST OF FIGURES	ix
I. INTRODUCTION	1
A. The First Observations of Auroral Kilometric Radiation	1
B. Location of the AKR Source Region	4
C. Characteristics of the AKR Source Region	9
D. The AKR Generation Mechanism	10
E. Characteristics of AKR	12
II. DESCRIPTION OF INSTRUMENTATION	19
A. The Spacecraft Instrumentation	19
B. Ground-Recording Scheme	24
C. Description of Ground-based Instrumentation	25
III. VERY LONG BASELINE INTERFEROMETRY	31
A. Characteristics of a Cross-Correlation Interferometer	31
B. Satellite-Satellite Interferometry	42
IV. METHOD OF ANALYSIS	47
A. Introduction	47
B. Determination of the Correct Delay	48
C. Correction for One-bit Digitization	53
D. Determination of Signal-to-Noise Ratio	54
E. Field Aligned Coordinate System	56
F. Normalization of Source-Satellite Distance	57
G. Calculation of Statistical Source Size	58
H. Calculation of Spectral Density and Brightness Temperature	59
V. DISCUSSION OF THE EVENTS	61
A. Characteristics of the Bursts	61
B. The Size of the AKR Source Region	69

C. The Source Size of the Individual Bursts	71
D. The Brightness Temperature	72
E. Source Region Spectral Density	73
F. Source Region Amplification	73
G. Summary	74
VI. INTERPRETATION OF THE RESULTS	76
A. Properties of Incoherent and Coherent Radiation	76
B. AKR Source Region Models	78
C. Source Region Amplification	88
D. Ray-Tracing Results	90
E. Point Scattering of the Waves	91
F. Properties of the Correlation	93
G. Summary	96
VII. CONCLUSIONS	100
A. Results	100
B. Areas for Further Investigation	101
APPENDIX A: CALCULATION OF CROSS-CORRELATION FUNCTION	172
A. Cross-Correlation Function for an Arbitrary Power Spectra	172
B. Cross-Correlation Function for a White-Noise Power Spectra	183
C. Cross-Correlation Function for a Gaussian-Shaped Power Spectra	184
APPENDIX B: DERIVATION OF AN INTERFEROMETER'S RESPONSE TO AN EXTENDED SOURCE	187
A. Definition of Coordinate System and Parameters	188
B. Source Relative Baseline Projections	190
C. Response of an Interferometer to a Point Source	192
D. Response of an Interferometer to an Extended Source	193
APPENDIX C: RAY-TRACING RESULTS	201
A. The Ray-Tracing Program	202
B. The Apparent Source Size	206
C. The Ray-Tracing Results	209
D. Summary	228
REFERENCES	257

LIST OF TABLES

Table	Page
1. Slope of the Striations in Frequency-Time Correlograms, for Different ISEE-1 Signal Delays.	103
2. Correlation Results for Events at Long Baselines.	104
3. Amplifying Region Diameters for Different Illumination Cone Sizes, Assuming Diffraction Effects.	105
4. AKR Source Size Predicted by Single Amplifying Region Model.	106
5. AKR Source Size Predicted by Multiple Amplifying Region Model.	107
C-1. Spacecraft Coordinates Used in the Ray-Tracing Analysis. .	230

LIST OF FIGURES

Figure		Page
1.	The ISEE-1 plasma wave experiment block diagram (from Gurnett et al. [1978]), showing the narrow band sweep frequency receiver, the coarse resolution spectrum analyzer, the wave normal analyzer, the wideband receiver, the three electric dipole antennas, and the triaxial search coil magnetometer.	108
2.	A diagram of the ISEE-1 spacecraft (from Gurnett et al. [1978]) showing the physical locations of the six electric field antennas and the triaxial search coil magnetometer.	110
3.	A block diagram of the ISEE-1 wideband receiver electronics (from Shawhan [1979]). The ISEE-2 wideband receiver is identical to the ISEE-1 wideband receiver, except that no 40 kHz bandwidth mode exists, and the reference frequency mixed with the received signal is 15.125 kHz instead of 62.5 kHz.	112
4.	A block diagram of the ISEE-2 plasma wave experiment (from Gurnett et al. [1978]) showing the two electric dipole antennas, the coarse resolution spectrum analyzer, and wideband receiver.	114

5. A diagram of the ISEE-2 spacecraft (from Gurnett et al. [1978]) showing the physical locations of the two electric field antennas and the search coil magnetometer. 116
6. The ISEE interferometer tape recording scheme (from Shawhan [1979]). The analog data, frequency references, and time code information for one spacecraft are recorded on the same tape recorder track. The reference frequencies can be used to determine the exact local-oscillator frequency for each wideband receiver and the time code can be used for precise time alignment of the data. 118
7. The ISEE interferometer analog tape processing scheme. The analog tape can be processed to produce three types of outputs. Strip chart recordings can be produced, giving the correlation fringe amplitude, the digital output from a Nicolet UA-500 A spectrum analyzer is interfaced to a computer for further analysis of the spectral characteristics, and 70 mm survey plots and correlograms can be produced over large time intervals. The one-bit digitized data can also be computer processed to produce delay-time correlograms. 120

10. This figure is a delay-time correlogram for white-noise test signals with a 10 kHz bandwidth. The correlation is plotted as a function of time for different signal delays. The slope of the striations is a function of the center frequency of the signals and the local-oscillator frequency difference. The rate of decrease in the correlation is determined by the bandwidth of the signal. 126
11. This figure shows the correlation, for different signal delays and bandwidths, of a signal with a white-noise power spectral density. The wider the bandwidth, the faster the correlation decreases. 128
12. This figure shows the correlation, for different signal delays and bandwidths, of a signal with a Gaussian power spectral density. 130
13. This figure shows the correlation of a signal with a band-pass filtered Gaussian power spectral density, for different signal delays and ratios of filter bandwidth to signal bandwidth. The shape of the curves, for different filter bandwidth to signal bandwidth ratios, are very similar for correlations above 20 percent. This indicates that the bandwidth is more important in determining the rate of decrease in correlation, as a function of signal delay, than spectral shape. 132

14. This figure shows the correlation of a two-dimensional Gaussian brightness distribution as a function of the source size multiplied by the baseline. The source size is defined as the angular width of the points where the brightness has been reduced by a factor of $1/e$. An interferometer can directly measure the source size only for incoherent radiation. 134
15. The integration time constant of the correlator will lower the measured correlation if the fringe rate is comparable to the time constant. This figure shows the coherence, as a function of the integration time constant, for fringe frequencies of 6 Hz (the fringe rate at 250 kHz) and 3 Hz (the fringe rate at 125 kHz). The time constant used in the correlator is 10 ms, thus the correlation is reduced by 2 percent for the 125 kHz data and by 5 percent for the 250 kHz data. 136
16. This figure shows a series of correlograms that was produced by correlating identical signals with white-noise power spectral densities, obtained during spacecraft integration, with different signal delays. The slope of the striations is a function of the signal delay, and thus can be used to determine the signal delay required to maximize the correlation. 138

17. This figure is a plot of the reciprocal of the striation slope as a function of signal delay. From the slope of the striations, the desired signal delay can be determined to within ± 100 μ sec. 140
18. This figure shows the geometry of the field-aligned coordinate system chosen, to determine the projected baselines. The z axis of the source-centered coordinate system is along the source-baseline direction, and the magnetic field is in the y-z plane (the source-centered coordinate system can also be rotated so that the gradient of the magnetic field is in the y-z plane), to give baseline components parallel and perpendicular to the magnetic field (or gradient of the magnetic field). 142
19. Spectrograms and correlograms for an AKR event detected by ISEE-1 and -2 on June 12, 1978. The top two panels show the independent spectrograms of the signals received by ISEE-2 and -1. The second two panels are frequency-time correlograms for this event. Nearly vertical striations can be seen in the correlograms, indicating that the signals are close to being correctly time aligned. 144

20. This figure is a continuation of the event shown in Figure 19. This event has regions where the bandwidth is extremely narrow, e.g., between 1725:07 UT and 1725:15 UT, and other regions where the signal bandwidth is several kilohertz. Comparison of the correlograms, for the unfiltered and filtered signals, shows that in addition to having a higher correlation when filtered signals are correlated, small amplitude fringes can be observed in the filtered signal correlogram that were not observed in the unfiltered correlogram (e.g., between 1724:46 UT and 1724:48 UT). 146
21. Spectrograms of three events detected by ISEE-1 and -2 on February 20, 1979 between 0038 UT and 0052 UT. Comparison of the signal amplitudes received by both spacecraft may help determine the size of the solid angle that an individual AKR event is beamed into. 148
22. Spectrograms of three events detected by ISEE-1 and -2 on February 20, 1979 between 0307 UT and 0312 UT. The burst starting with a frequency near 4 kHz at 0308:10 appears to rapidly change bandwidth or amplitude. The burst rising in frequency at 0311:20 is another of the bursts analyzed. 150

Figure	Page
23. This figure is a delay-time correlogram for an AKR event detected on February 20, 1979. Since this burst has a very narrow bandwidth, the correlation remains large over a wide range of delays.	152
24. This figure is a time-delay correlogram for the same AKR burst as in Figure 23 but 1 second later. The abrupt phase changes in the correlation are presently not understood.	154
25. This delay-time correlogram shows the effect of signal bandwidth on the correlation for different signal delays. The correlation is maximized in the region where the striations are most uniform. There appears to be short time intervals where the bandwidth of the burst is narrower than at other times.	156
26. The vertical spacing of the fringes in a delay-time correlogram is a function of the center frequency of the correlated signals. As the frequency of the signals increases, the spacing of the fringes decreases.	158
27. The correlation as a function of baseline is fit to a model source brightness distribution for incoherent sources. The source region diameter is determined primarily by the correlation at the longest baseline. . .	160

28. This figure shows the geometry of the amplifying region model. If the size of the amplifying region is comparable to the wavelength of the radiation, the angular size Ω of galactic background illuminating the spacecraft through the amplifier can be larger than the angular size θ of the amplifier as viewed from the spacecraft. For large amplifying regions, the two angular sizes Ω and θ are equal. For this model, the correlation is related to the area of overlap between the illumination cones for each spacecraft. 162
29. This figure is a plot of the correlation predicted by the amplifier model for different ratios of spacecraft separation to the angular size of the illumination cone. The correlation goes to zero when the illumination cones no longer overlap. 164
30. This figure shows the angular size of the radiation pattern from a coherent Gaussian brightness distribution, for different angular diameters of the brightness distribution. The angular size of the radiation pattern remains narrow until approximately 25 km for an emission frequency of 250 kHz. 166

Figure	Page
31. The total wave growth, required to explain the observed intensity of AKR, is plotted as a function of source region diameter. Decreasing the source region diameter by a factor of 10, increases the required wave growth by 20 db.	168
32. The growth rate, required to explain the observed intensity of AKR, is plotted as a function of source region diameter. The growth rate within the source region is assumed to be constant. The growth rate increases very rapidly for source region diameters less than 10 km. . . .	170
B-1. This figure shows the source-baseline geometry, relative to a coordinate system moving with the spacecraft (primed system), and the coordinate system associated with the source region (unprimed system).	199
C-1. This figure shows the geometry of the AKR source region, the plasmopause, and the R-X mode cutoff surface. In the region where the waves are predicted to reflect, the R-X cutoff surface closely follows the plasmopause.	231
C-2. This figure shows the propagation time difference, as a function of magnetic local time, for waves which propagate directly to the spacecraft.	233

Figure	Page
C-3. This figure shows the propagation time difference, as a function of magnetic local time, for waves which reflect from the plasmopause at an L-value of 4.00.	235
C-4. This figure shows the projected baseline, as a function of magnetic local time, for waves which propagate directly to the spacecraft and for waves which reflect from the plasmopause at an L-value of 4.00. The projected baseline for waves which reflect from the plasmopause is larger than the projected baseline of waves which propagate directly to the spacecraft.	237
C-5. This figure shows the projected baseline for waves which reflect from the plasmopause at different L-values, and the projected baseline for waves which propagate directly to the spacecraft, with a source region located along a 70° Mlat field line.	239
C-6. This figure shows the size and shape of the source region image when the waves are reflected from the plasmopause. The size is normalized so that the source region has a diameter of one, for waves which propagate directly to the spacecraft. The shape of the source region image is approximately elliptical, for small source regions. . . .	241

- C-7. This figure shows the normalized AKR source region diameter for waves which propagate directly to the spacecraft. The source region diameter is larger for source region locations near 18.0 hrs MLT than for source region locations near 6.0 hrs MLT, with the same correlation. . . 243
- C-8. This figure shows the normalized AKR source region diameter for waves which reflect from the plasmopause at an L-value of 4.00. The curves are normalized so that a value of one is the same diameter as a source region located along a 70° Mlat field line at 21.0 hrs MLT, with the waves propagating directly to the spacecraft. . . . 245
- C-9. This figure shows the normalized source region diameter for waves which reflect from the plasmopause at different L-values, and for comparison, a plot of the normalized source region diameter for waves propagating directly to the spacecraft. The normalized source diameter changes only slightly for different L-values of the reflecting surface. 247
- C-10. This figure shows the wave-normal angle of the emitted waves which propagate directly to the spacecraft, and the wave-normal angle of the emitted waves which reflect from the plasmopause at an L-value of 4.0. 249

- C-11. This figure shows the wave-normal angle of the emitted waves which reflect from the plasmopause. An increase of 0.25 in L-value causes a maximum increase in the wave-normal angle of 5° , for plasmopause L-values between 3.75 and 4.00. 251
- C-12. This figure shows the normalized size and shape of the solid angle of amplified galactic background noise illuminating the spacecraft, for waves reflecting from the plasmopause. The radius is normalized so that a circle of radius equal to one is the solid angle of amplified galactic background noise illuminating the spacecraft when the waves propagate directly to the spacecraft. 253
- C-13. The flux density of the waves received at the spacecraft is proportional to the solid angle of amplified background noise illuminating the spacecraft. This figure is a plot of the solid angle of amplified background radiation illuminating the spacecraft. The flux density of the received signal is from 17.8 to 73.3 times greater for waves reflecting from the plasmopause than for waves propagating directly to the spacecraft. 255

I. INTRODUCTION

Auroral kilometric radiation (AKR) is the most intense electromagnetic radiation that is generated in the earth's magnetosphere. Ground-based interferometry has been used successfully for the study of astrophysical radio sources for the last forty years. Until the launch of the ISEE-1 and -2 spacecraft, the study of terrestrial radio sources using spacecraft interferometry had never been attempted. The purpose of this research is to develop the techniques necessary to perform satellite-satellite interferometry and to present the first interferometry measurements of the AKR source region diameter. In the last decade, AKR has generated considerable interest because of its similarities with other astrophysical radio sources, particularly Jovian decametric radiation [Kaiser and Stone, 1975]. An understanding of the generation mechanism and properties of AKR can lead to the understanding of other astrophysical radio sources, where in situ measurements are not possible.

A. The First Observations of Auroral Kilometric Radiation

Since kilometric wavelength radiation cannot penetrate the ionosphere, AKR was not detected until satellites were launched with plasma wave receivers aboard. AKR was first reported by Benediktov et al. [1965] from observations with the Elektron satellites, at frequencies

of 0.725 MHz and 1.5 MHz. Benediktov et al. [1965, 1968] reported that this radiation was associated with geomagnetic activity, and concluded that it must be generated near the earth. Dunckel et al. [1970] reported that this radiation was observed primarily in the local nighttime and was strongly correlated with the auroral electrojet (AE) index. Spacecraft observations over the last decade have revealed that AKR is closely associated with the auroral electron acceleration process.

Gurnett [1974] provided the first comprehensive study that showed AKR was directly correlated with auroral processes. Gurnett [1974] found a high correlation between the observation of AKR with the IMP-6 spacecraft and the presence of discrete auroral arcs in Dapp spacecraft auroral photographs. During bright auroral displays, Gurnett [1974] estimated the maximum power radiated could be as high as 10^9 watts. Since the discrete aurora had been directly associated with intense inverted-V electron precipitation [Frank and Ackerson, 1971; Ackerson and Frank, 1972], Gurnett [1974] deduced that AKR must also be associated with inverted-V electron precipitation. Gurnett [1974] also reported that the observed angular distribution of AKR could be explained by emission of the radiation at radial distances of less than 3.0 earth radii (R_E) along auroral field lines. Kurth et al. [1975] analyzed wave direction measurements from the IMP-8 and Hawkeye spacecraft and concluded that AKR was generated along auroral field lines near 21 hrs local time (LT). From an analysis of RAE-2 spacecraft measurements, Kaiser and Alexander [1976] determined that

probability of occurrence for AKR source region locations was sharply peaked between 21 hrs and 22 hrs LT and the source region locations appeared to trace out 70° magnetic latitude field lines.

After Gurnett's [1974] deduction that AKR was associated with inverted-V electron precipitation, a number of studies confirmed the relationship of AKR to auroral processes. Voots et al. [1977] found a correlation between high-altitude magnetic disturbances produced by the auroral electrojet current.

Green et al. [1979] used simultaneous observations of inverted-V electrons with the AE-D spacecraft, and remote detection of AKR with the Hawkeye spacecraft, to determine that AKR is statistically more closely correlated with inverted-V electrons than with plasma sheet precipitation. Since remote observations of AKR can simultaneously detect signals from many different source regions, and since the particle measurements can be made only at one location, Green et al. [1979] could not show a one-to-one correspondence between the presence of inverted-V electrons in a region and the generation of AKR in that same region. A good quantitative correlation was found between the intensity of AKR and the peak energy of the inverted-V events. Benson and Calvert [1979] reported simultaneous observations of AKR and inverted-V electrons during AKR source region encounters with ISIS-1. Benson et al. [1980] found examples with ISIS-1 where the AKR source region was identified with the edge of an inverted-V structure. In Benson and Calvert's [1979] previous study, the AKR source region appeared to be strongly associated with the peak of the inverted-V

structure, when the plasma density was low throughout the inverted-V structure. Benson et al. [1980] reported that the electron velocity distribution functions recorded by ISIS-1 always had a positive slope in the keV energy range near the peak of an inverted-V structure associated with an AKR source region encounter, even when the AKR source region correlated best with the edge of the inverted-V structure. Benson et al. [1980] concluded that in order for AKR to be generated it was necessary to have the coincidence of inverted-V electrons, with an energy distribution function containing positive slopes in the keV energy range, and regions of depleted electron density.

B. Location of the AKR Source Region

A number of techniques have been used to determine the location of the AKR source region. With most of the techniques, an average source region location is determined by an analysis of the characteristics of the radiation observed by remotely orbiting spacecraft. Several of the techniques have been able to determine a source region location for individual events. All of the techniques have found AKR source region locations that are consistent with generation along auroral field lines ($\sim 70^\circ$ magnetic latitude) in the local nighttime (~ 2000 to ~ 2400 local time) at radial distances of 1.5 to 3.5 R_E .

1. Spin Modulation Analysis

Kurth et al. [1975] analyzed the modulation, caused by spacecraft rotation, of the received AKR signal to determine the average source region location. Since this technique can only determine one

component of the source region location, a number of IMP-8 and Hawkeye observations, with the spacecraft located at different positions in local time, were combined to find an average source region location. Kurth et al. [1975] determined an average source region location, projected into the equatorial plane, of 21.25 hrs local time (LT) at $0.835 R_E$ from the polar axis, for radiation at 178 kHz.

2. Relative Signal Phase Measurements

Calvert [1985b] used the relative phase between the signals received by two orthogonal antennas on the DE-1 spacecraft to determine the AKR wave direction. The relative phase of the received signals is a function of the angle between the wave direction and the Z-axis antenna (oriented parallel to the spacecraft spin axis), the angle between the wave direction and X-axis antenna (oriented perpendicular to spacecraft spin axis), and the wave polarization [Calvert, 1985b].

From wave directions measured at two different spacecraft positions, Calvert [1985b] located the apparent AKR source region, as a function of frequency, by triangulation. Calvert [1985b] found that to within approximately $0.3 R_E$, the source region locations were consistent with generation of AKR at the gyrofrequency, along a single auroral-zone field line.

3. Lunar Occultation Technique

Using the lunar orbiting RAE-2 satellite, Kaiser and Alexander [1976] were able to find two-dimensional source region locations. By analyzing the position of RAE-2, relative to the lunar limb, when AKR

signals disappeared and then reappeared, as RAE-2 orbited behind the moon, a source location could be determined for each individual event. At a frequency of 250 kHz, most source locations were above the polar regions, at a radial distance of 2 to 3 R_E . The source region locations, for frequencies above 300 kHz, were found to be closer to the earth than the source region locations for frequencies below 300 kHz. The probability of occurrence for the source region locations and the observed power of AKR was sharply peaked between 21 and 22 hrs LT, and the source region locations appeared to trace out 70° magnetic latitude (Mlat) field lines. Kaiser and Alexander [1976] reported that approximately 10 percent of the events appeared to originate at radial distances greater than 7 R_E . Alexander et al. [1979] later reported that these anomalous source region locations were probably caused by propagation effects, rather than actual wave generation at a large radial distance. Alexander et al. [1979] speculated that strong scattering of the waves by large-scale density inhomogeneities in the magnetosheath, or scattering of the waves off ion plasma waves in the magnetosheath and/or the solar wind, could explain the apparent source region locations at large radial distances. Kaiser and Alexander [1976] also found considerable evidence for multiple sources and source motion, over the time scale of tens of minutes.

4. Angular Distribution of AKR

From a frequency of occurrence study of AKR, Gurnett [1974] showed that the observed conical radiation pattern could be explained if

the AKR source region was located on auroral field lines in the local nighttime, at radial distances of less than $3 R_E$.

Green et al. [1977] and Green and Gallagher [1985] used observations of AKR by the Hawkeye, IMP-6, and IMP-8 spacecraft to determine the angular distribution of AKR. The frequency of occurrence for AKR above a threshold, as a function of local time and magnetic latitude of the spacecraft, was found for emissions at 56.2 kHz, 100 kHz, 178 kHz, and 500 kHz. The emission cones were found to be centered around 22 hrs LT at auroral latitudes, with the emissions at higher frequencies beamed in to larger solid angles (1.1 sr at 56.2 kHz, 1.8 sr at 100 kHz, 3.5 sr at 178 kHz, and 5.3 sr at 500 kHz). Green et al. [1977] also studied the power flux received by two widely separated satellites (separated by 60° to 70° in magnetic latitude and 3 to 8 hrs in local time), and found that the absolute power fluxes of the signals detected by the different spacecraft were within 2 dB. Green et al. [1977] and Green and Gallagher [1985] conclude from these observations that AKR uniformly illuminates the entire region within the emission cone.

5. AKR Power Dependence on Radial Distance

By studying the average electric-field spectral flux, as a function of spacecraft position, Gallagher and Gurnett [1979] deduced the time averaged AKR source region location. To determine the AKR source region location, the average spectral flux, as a function of spacecraft position, was examined for a R^{-2} radial dependence. Source region locations between 22 and 24 hrs magnetic local time (MLT), and 65°

Mlat, at radial distances of from 2 to 3 R_E , gave the desired R^{-2} radial dependence of the spectral power flux. Gallagher and Gurnett [1979] also measured the angular size of the AKR emission cone at frequencies of 178 kHz, 100 kHz, and 56.2 kHz (4.1 sr at 178 kHz, 2.2 sr at 100 kHz, and 1.5 sr at 56.2 kHz), and estimated the average total power of AKR to be 10^7 watts.

6. Source Region Encounters

From southern hemisphere Hawkeye passes, Gurnett and Green [1978] observed a sharply defined low-altitude frequency cutoff for AKR, at the altitude where the local electron gyrofrequency was equal to the wave frequency. In a few cases the low frequency edge of the AKR emissions merged, essentially continuously, into a band of auroral hiss. Gurnett and Green [1978] concluded that these events were source region encounters and that AKR is generated slightly above the local gyrofrequency.

The signature of AKR, observed with the ISIS-1 spacecraft, has been used to determine the altitude of the AKR source region [Benson and Calvert, 1979; Calvert, 1981a]. With ISIS-1, AKR is observed as an intense noise band above the local cyclotron resonance. Penetration of the source region is indicated by a merging of the AKR noise band with the emissions at the cyclotron resonance [Calvert, 1981a]. From the source region encounters and a ray-tracing analysis, Calvert [1981a] concluded that AKR is extraordinary mode radiation, generated at a frequency slightly above the gyrofrequency, and propagates

preferentially in a direction perpendicular to the magnetic field. AKR was observed most frequently between 68° and 72° Mlat over a wide range of magnetic local times, with the most intense AKR centered about 22 hrs MLT [Benson and Calvert, 1979].

C. Characteristics of the AKR Source Region

1. The Auroral Plasma Cavity

The first evidence that AKR is generated in a region of low plasma density was provided by ISIS-1. A region of depleted electron density, with a minimum density of 25 cm^{-3} , was found to coincide with the AKR source region [Benson and Calvert, 1979]. The plasma depletion region was found to cover a wider extent in longitude than latitude, and could extend downward to $1.3 R_E$. At $1.5 R_E$, the plasma depletion region was found to extend a few degrees in latitude. Benson and Calvert [1979] suggested that the higher plasma density at the lower boundary of the plasma depletion region was responsible for the upper frequency limit of AKR. Since ISIS-1 encounters only the low altitude portion of the AKR source region, Calvert [1981b] used Hawkeye observations to show that the depletion region extends to much greater altitudes and constitutes an enormous plasma cavity, approximately 6° wide centered on 70° Mlat. ISIS-1 source region encounters showed that AKR is generated in regions where the ratio of electron plasma frequency (f_{pe}) to electron gyrofrequency (f_{ge}) is less than 0.2 [Benson and Calvert, 1979].

2. Plasma Cavity Density Enhancements

Within the plasma cavity, ISIS-1 occasionally observed sharp density enhancements of 1000 cm^{-3} above the 25 cm^{-3} plasma cavity density [Benson and Calvert, 1979]. These density enhancements were often found to be less than 100 km thick [Calvert, 1981a]. These density enhancements may be a common source region feature, but due to their small size, may not always be detected by ISIS-1 [Benson and Calvert, 1979].

D. The AKR Generation Mechanism

1. The Doppler-Shifted Cyclotron Resonance

A variety of mechanisms have been proposed for the generation of AKR (see review by Grabbe [1981]). The observed polarization and absence of intense electrostatic waves in the source region greatly restricts the possible generation mechanisms for AKR. The Doppler-shifted cyclotron resonance instability [Melrose, 1976; Wu and Lee, 1979] appears to be the most viable AKR generation mechanism. Melrose [1976] showed that an electron beam, with a large thermal anisotropy, could directly amplify extraordinary mode radiation by the Doppler-shifted cyclotron resonance instability. Since the electrons associated with AKR have not been experimentally observed with a large thermal anisotropy, Wu and Lee [1979] showed that, by including relativistic effects (even though the electrons associated with AKR are not relativistic), magnetically mirrored electrons with a loss-cone distribution could also directly amplify extraordinary mode radiation. A low background plasma density, which reduces the frequency difference between

the cyclotron frequency and the extraordinary mode cutoff frequency, is necessary for resonance with the electrons associated with AKR. Spacecraft observations within the AKR source region have shown that the f_{pe}/f_{ge} ratio must typically be less than 0.1 to 0.3 for the generation of AKR [Calvert, 1981b].

Several authors have calculated growth rates using the relativistic cyclotron resonance condition, and experimentally measured pitch angle distributions. Omidi et al. [1984] and Omidi and Gurnett [1984] calculated AKR growth rates, using electron pitch angles measured by the S3-3 satellite. Path integrated growth rates, computed with steepened electron distributions, indicate that the amplification lengths must be on the order of a 70 km or longer to account for the observed intensities of AKR [Omidi and Gurnett, 1984].

2. The Laser Feedback Model

Calvert [1982] proposed that the generation mechanism for AKR involves positive wave feedback, rather than open loop amplification. With the feedback model, AKR is presumed to be generated in a thin, local density enhancement. Partial reflection of the amplified waves at the boundary of the density enhancement provides a closed feedback path. For oscillation, the closed feedback path is required to have a length equal to a multiple of the wavelength. The feedback model predicts discrete bursts of nearly monochromatic, spatially coherent radiation. The feedback model proposed by Calvert [1982] visualizes the source of AKR as a natural radio laser.

Statistical studies of the onset of AKR and arrival of solar radio bursts indicate that AKR is sometimes triggered by type II radio bursts [Calvert, 1985a] and type III radio bursts [Calvert, 1981c; Farrell, 1984; Farrell and Gurnett, 1985; Farrell et al., 1986], with the triggered emission lasting long after the solar radio burst had ceased. Calvert [1981c] observed that although AKR onsets appear to be abrupt and spontaneous, sometimes AKR develops from a discrete frequency near the leading edge of a type III radio burst. Sometimes AKR occurs at progressively lower frequencies, following the leading edge of the solar radio bursts [Calvert, 1981c; Calvert, 1985a]. Calvert [1985a] concluded that triggering of AKR by external radiation is evidence that AKR must originate from a natural radio laser.

Since the waves are amplified on multiple passes through the source region, the amplification required to explain the observed AKR intensity is lower with the laser feedback model than with only simple wave amplification. Calvert [1982] estimated that 40 dB of wave growth is required with the laser feedback model, instead of 70 to 120 dB without feedback.

E. Characteristics of AKR

1. Temporal and Spectral Characteristics

AKR is observed in the frequency range of approximately 30 kHz to 700 kHz, with the frequency of the spectral peak varying inversely with the AE index [Kaiser and Alexander, 1977]. Distinct storms lasting from tens of minutes to several hours are observed. At peak

intensities, Gurnett [1974] estimated the total power to be approximately 10^9 watts, while the average power was estimated to be approximately 10^7 watts [Gallagher and Gurnett, 1979]. The onset and termination of AKR appears to result from a decrease in the bandwidth with the upper and lower cutoffs pinching together [Gurnett and Anderson, 1981].

AKR has clearly defined upper and lower cutoff frequencies, which can fluctuate over a wide range in the time scale of tens of minutes or less [Gurnett and Anderson, 1981]. The upper and lower cutoff frequencies have been explained by the f_{pe}/f_{ge} ratio [Benson and Calvert, 1979; Calvert, 1981b; Gurnett and Anderson, 1981] and additionally, the lower cutoff frequency can be influenced by the location of electron accelerating regions in the magnetosphere [Gurnett and Anderson, 1981]. Calvert [1981b] presented a contour plot of f_{pe}/f_{ge} for the auroral plasma cavity, and noted that the extremes of the 0.1 contour corresponds to gyrofrequencies of 50 kHz and 600 kHz (corresponding to the average frequency range of AKR), and that the minimum f_{pe}/f_{ge} ratio, of less than 0.03, occurs at approximately $1.8 R_E$, corresponding to a gyrofrequency of 250 kHz (the frequency spectrum of AKR usually peaks at about 250 kHz). From these observations Calvert [1981b] concluded that the cavity controls the overall emission spectrum of intense AKR and that the cavity is essential for the generation of AKR.

Many narrow-band discrete bursts fill the entire frequency range between the upper and lower cutoffs. These discrete AKR bursts show a close similarity to whistler-mode emissions, implying that the basic

instability mechanisms are quite similar [Gurnett and Anderson, 1981]. The frequency drifts can be interpreted in terms of the propagation of shock like disturbances, along auroral field lines at velocities near the ion acoustic speed [Gurnett and Anderson, 1981], with the spatial extent of the disturbance determining the bandwidth of the emission.

Calvert [1982] interprets the discrete structure of AKR bursts as different oscillation modes, within a source region that is a natural laser. The laser feedback model predicts nearly monochromatic waves (0.03 to 10 Hz), at discrete frequencies [Calvert, 1982]. The bandwidth of individual AKR bursts can vary from tens of hertz to several kilohertz. A possible explanation for signal bandwidths of several kilohertz is that temporal fluctuations of the gain, the feedback path, or the saturation amplitude, modulate the emitted signal [Calvert, 1982]. Other features of AKR bursts can be explained as properties of amplification with feedback. An abrupt shift in the emission frequency has been explained by Calvert [1982] as the quenching of one oscillation mode by another oscillation mode. The splitting of an emission at one frequency into multiple frequency components can be explained as triggering of one AKR burst by another [Calvert, personal communication, 1985].

2. Polarization of AKR

The polarization of AKR has caused considerable controversy over the last few years. Evidence for both ordinary and extraordinary mode radiation has been presented by a number of authors. It is now

believed that AKR consists of both R-X and L-O mode radiation, with the most intense and dominant component being generated in the R-X mode [Shawhan and Gurnett, 1982; Mellott et al., 1984].

Three methods have been used to determine the polarization of AKR: (1) a comparison of the observed emission cone with the emission cone predicted by ray-tracing calculations, (2) direct polarization measurements of the observed radiation, and (3) the cutoff frequency of the waves observed in the source region. The first technique that was used to determine the polarization of AKR compared the observed emission cone with the emission cone predicted by ray-tracing calculations. Green et al. [1977] compared the results of ray-tracing calculations for both R-X and L-O mode radiation originating at different altitudes in a model magnetosphere, to the observed frequency of occurrence (as a function of local time and magnetic latitude) for AKR. Generation of R-X mode radiation slightly above the R-X mode cutoff was most consistent with the observed emission cone.

Kaiser et al. [1978] have directly measured the polarization of AKR with the Voyager-1 spacecraft and found that intense AKR is predominantly extraordinary mode radiation. Shawhan and Gurnett [1982] and Mellott et al. [1984] have directly measured the polarization of AKR with the DE-1 spacecraft, and reported the observation of both R-X mode and L-O mode radiation. When both modes were observed, Mellott et al. [1984] found that L-O mode radiation was almost always observed at a lower frequency than R-X mode radiation, and that the R-X mode to L-O mode power ratio was approximately 50. R-X mode radiation ray

paths were found to be confined to a cone within 50° of the source region magnetic field, and L-O mode radiation was typically observed outside of this cone [Mellott et al., 1984]. The local electron gyrofrequency seemed to constitute an absolute lower frequency cutoff for both modes, suggesting that both R-X and L-O mode radiation are produced within the same source region but are refracted differently as they propagate away from the source region [Mellott et al., 1984].

Since the low frequency cutoff for R-X mode radiation is different from the low frequency cutoff for L-O mode radiation, the observed cutoff within the source region can be used to determine the polarization of AKR. The low frequency AKR cutoff, observed within the AKR source region, is found to be near or slightly above the local extraordinary mode cutoff [Gurnett and Green, 1978; Benson and Calvert, 1979]. Gurnett and Green [1978] and Benson and Calvert [1979] used these satellite observations to conclude that AKR is generated in the extraordinary mode.

There have also been observations of L-O mode radiation within the AKR source region. Oya and Morioka [1983] have identified L-O mode radiation from the low frequency cutoffs of AKR, observed with the JIKIKEN (EXOS-B) spacecraft. Benson [1982, 1984] has also identified L-O mode radiation AKR on ISIS-1 ionograms during source region encounters.

Hashimoto [1984] used ray-tracing, in an electron plasma cavity density model of the magnetosphere, to show that propagation effects could explain both the R-X mode and the L-O mode observations. L-O

mode radiation can be observed over a much larger latitudinal range than R-X mode radiation because: (1) R-X mode cannot propagate through regions where the wave frequency is below the R-X mode cutoff. (2) R-X mode radiation is strongly refracted away from the R-X mode cutoff surface. Hashimoto [1984] speculated that both R-X mode and L-O mode radiation are present, with the R-X mode radiation at a higher intensity. In regions accessible to both modes, R-X mode will dominate, but in regions not accessible to R-X mode radiation, only L-O mode radiation will be observed. The JIKIKEN spacecraft observations of L-O mode radiation [Oya and Morioka, 1983] are consistent with Hashimoto's [1984] hypothesis because the JIKIKEN spacecraft predominantly covers a low altitude region, that is inaccessible to R-X mode radiation.

Since the interferometry receivers are aboard spacecraft, there are constraints that limit the type of receivers which can be used and that dictate the format of the received data. Chapter II discusses the spacecraft instrumentation and the ground-based correlator that comprise the ISEE interferometer. Chapter III discusses interferometry and the differences between spacecraft interferometry and ground-based astrophysical interferometry.

The differences between ground-based interferometry and spacecraft interferometry required modifications to the astrophysical interferometry data processing techniques. Chapter IV presents the methods that were devised to process the spacecraft interferometry data. Uncertainty in the absolute time alignment of the received sig-

nals required new techniques to be developed for determining the correct signal delays necessary to maximize the correlations.

Chapter V discusses the correlation measurements. The statistical source region diameter and the source region diameters for the individual bursts are presented. From these source region diameters and the received signal strengths, the spectral density and required wave growth are calculated. Chapter VI compares the measured correlations and calculated source region sizes to the measurements predicted by incoherent and coherent radiation models of the source generation region.

II. DESCRIPTION OF INSTRUMENTATION

A. The Spacecraft Instrumentation

Data from two satellites, ISEE-1 and ISEE-2, are used to perform long-baseline interferometry. Both satellites were launched on October 22, 1977 into nearly identical orbits. The orbits are elliptical with initial perigee and apogee altitudes of 280 km and 145,000 km, respectively, an orbit inclination of 28.7° , and an orbital period of 2.4 days. The separation of the two spacecraft is controllable, allowing long-baseline interferometry to be performed with baselines from approximately 10 km to 10,000 km.

Both ISEE-1 and ISEE-2 have wideband receivers capable of detecting AKR. The waveforms detected by the wideband receivers are recorded on analog tapes at the NASA telemetry stations, and are the data used for long-baseline interferometry.

1. ISEE-1

The University of Iowa plasma wave instrument aboard ISEE-1 is designed to measure the electric field over the frequency range of 5.6 Hz to 2 MHz, and the magnetic field over the frequency range of 5.6 Hz to 10 kHz. The plasma wave receiver consists of four main elements: (1) a 34-channel high-time resolution spectrum analyzer, (2) a narrow-band (high-frequency resolution) sweep-frequency

receiver, (3) a wave-normal and Poynting flux analyzer, and (4) a wideband analog receiver. A block diagram of the plasma wave electronics is shown in Figure 1. These four main elements may be connected in certain combinations to the six plasma wave antennas. The six plasma wave antennas consist of three electric dipole antennas with tip-to-tip lengths of 215 m, 73.5 m, and 0.61 m, and a triaxial search coil magnetometer. The physical locations of the six antennas on the spacecraft are shown in Figure 2.

The 34-channel high-time resolution spectrum analyzer consists of a 20-channel analyzer, with four logarithmically spaced channels per decade (in a 1.0, 1.78, 3.11, and 5.62 sequence), covering the frequency range of 5.6 Hz to 311 kHz, and a 14-channel analyzer, also with four logarithmically spaced channels per decade, covering the frequency range of 5.6 Hz to 10 kHz. The 20-channel analyzer is normally used for electric-field measurements, and the 14-channel analyzer is normally used for magnetic-field measurements. For frequencies below 10 kHz the effective noise bandwidth is ± 15 percent, and for frequencies above 10 kHz the effective noise bandwidth is ± 7.5 percent. The output voltage from each spectrum analyzer channel is proportional to the logarithm of the electric- or magnetic-field strength, and has a dynamic range of 110 dB. The sampling rate for each channel is one sample per second in the low data rate, and four samples per second in the high data rate. The spectrum analyzer data are useful in identifying periods of intense AKR.

The narrow-band sweep-frequency receiver consists of 128 logarithmically spaced frequency channels, covering the frequency range of 100 Hz to approximately 400 kHz with a frequency resolution of approximately 6.5 percent. The sweep-frequency receiver has an output voltage proportional to the logarithm of the field strength and has a dynamic range of approximately 90 dB. The sampling rate for each channel is one sample every 32 sec.

The wave-normal analyzer consists of five narrow-band frequency conversion receivers, all tuned to the same frequency. The wave-normal analyzer receivers can be tuned to one of 32 frequency channels, each with a bandwidth of 10 Hz, in the frequency range of 100 Hz to 5 kHz. The wave-normal analyzer provides the detailed phase and amplitude measurements of the signals received by the triaxial search coil magnetometer and the orthogonal electric dipole antennas, which are necessary to compute the wave-normal direction and Poynting flux. Measurements can be obtained from any one of the 32 frequency channels every 32 sec, or the wave-normal analyzer may be commanded to step through all 32 channels at a step rate of one step every 32 sec.

The wideband receiver consists of two frequency channels; the first channel covers the frequency range of 10 Hz to 1 kHz, and the second channel is a tunable single-sideband single-conversion receiver, with a bandwidth switchable by command to either 10 kHz or 40 kHz. The 10 Hz to 1 kHz channel is transmitted as a frequency modulated subcarrier, and the 10 kHz (or 40 kHz) bandwidth channel modulates the special-purpose analog transmitter directly. A block

diagram of the wideband receiver is shown in Figure 3. Frequency pre-selection filters with a bandwidth of 40 kHz limit the incoming signal to one of eight possible frequency ranges. The lower bandedge frequencies for the eight possible frequency ranges are 2.0 MHz, 1.0 MHz, 500 kHz, 250 kHz, 125 kHz, 62.5 kHz, 31.1 kHz, and 0-10 kHz (or 0-40 kHz) baseband (no frequency conversion). The filtered input signal is mixed with quadrature frequency components f and f_{90} . As indicated in Figure 3, the upper and lower sidebands are superimposed, but have different phase relationships in the two legs. An audio-frequency quadrature phase shift network shifts the signal in one leg by an additional 90° , so that when the signals in the two legs are added together in the summing amplifier, the upper sideband components add and the lower sideband components cancel. The sideband rejection is greater than 25 dB. The output of the receiver is further filtered by a 650 Hz to 10 kHz (or 40 kHz) filter, and added together with a reference frequency derived from the receiver's local-oscillator. This combined signal modulates the spacecraft's analog S-band transmitter. At the telemetry station the received signal is demodulated and added to a 50 kHz carrier, which has been modulated by NASA 36-bit time code, and then recorded on an analog tape recorder. To be able to correlate the two received signals, the wideband receiver's local-oscillators must be at very nearly the same frequency and, over the correlation time, the phase between the two frequencies must not change by more than 1 radian. Laboratory calibration of the receivers

indicate that stability is better than $1 \times 10^{-6} \Delta f/f$ over the expected spacecraft temperature range and over the spacecraft buss voltage variations [Shawhan, 1979].

To provide a method to accurately determine the oscillator frequency, a submultiple of the oscillator frequency (62.5 kHz for ISEE-1 and 15.625 kHz for ISEE-2) is added to the output signal of the wideband receiver.

To achieve the highest possible signal-to-noise ratio for the telemetry signal received on the ground, an automatic gain control maintains a nearly constant signal amplitude into the analog transmitter. The automatic gain control signal is digitally sampled once every second and covers 110 dB dynamic range. The higher frequency ranges of the wideband receiver are used primarily for long-baseline interferometry. A more complete description of the ISEE-1 plasma wave instrument can be found in Gurnett et al. [1978].

2. ISEE-2

The University of Iowa plasma wave instrument aboard ISEE-2 is designed to measure electric and magnetic fields over the range of 5.6 Hz to 31.1 kHz. The plasma wave receiver consists of two elements: (1) a 16-channel high time resolution spectrum analyzer, and (2) a wideband analog receiver. A block diagram of the plasma wave electronics is shown in Figure 4. The two elements may be connected to any one of the three plasma wave antennas. The three plasma wave antennas consist of two electric dipole antennas with tip-to-tip

lengths of 30 m and 0.61 m, and a search coil magnetometer. The physical orientations of these antennas on the ISEE-2 spacecraft are shown in Figure 5.

The spectrum analyzer has 16 channels extending from 5.6 Hz to 31.1 kHz. The bandwidths and center frequencies of these channels are identical to the spectrum analyzer on ISEE-1. The spectrum analyzer is sampled at a rate of one sample per second at the low data rate, and at four samples per second at the high data rate.

The wideband receiver aboard ISEE-2 is essentially identical to the ISEE-1 wideband receiver except that the single-sideband single-conversion receiver has no 40 kHz mode. A more complete description of the ISEE-2 plasma wave instrument can be found in Gurnett et al. [1978].

B. Ground-Recording Scheme

At each telemetry station a NASA 36-bit time code is generated from a Cesium frequency standard, and amplitude modulates a 50 kHz carrier. This time code signal is added to the demodulated telemetry signal and recorded on an analog tape recorder. The 50 kHz carrier and the time code signals can be used, if necessary, to remove tape recorder wow and flutter on playback and to time align the recorded data, if the data are recorded on two separate tape recorders at different telemetry stations. This modulation scheme and the composite recorded spectrum for ISEE-1 and -2 are shown in Figure 6. The absolute time accuracy of the Cesium clock is $\pm 25 \mu\text{sec}$. Since the

correlation is reduced when signals are correlated with an incorrect delay, the time must be accurately known. Appendix A derives the correlation, as a function of signal delay and bandwidth, for signals with white-noise and Gaussian spectral characteristics. The required timing accuracy for interferometry is given by

$$\tau = (\pi \Delta f)^{-1} \quad , \quad (1)$$

where Δf is the bandwidth of the received signal [Shawhan, 1979]. For the ISEE interferometer system, with a receiver bandwidth of 10 kHz, the required time accuracy is approximately 32 μ sec. This is comparable to the ± 25 μ sec accuracy provided by the NASA telemetry station. The optimum data processing scheme is for the data to be recorded on adjacent tracks of the same tape. Tape recording on the same tape minimizes timing errors, and the wow and flutter should be nearly the same.

C. Description of Ground-based Instrumentation

The ISEE-1 and -2 analog tapes are processed by three different sets of instrumentation to produce spectrograms and correlograms. Wideband survey plots or correlograms are produced with dual Federal Scientific UA-6 spectrum analyzers and the 70 mm camera system. High-time and frequency resolution spectrograms are produced by processing the signals with a Nicolet Scientific Corporation UA-500A spectrum

analyzer. Strip chart recordings with correlation plotted as a function of time, and delay-time correlograms, with the correlation plotted as a function of both time and delay, are produced by processing the signals with the correlator system. The signal paths and associated instrumentation are shown in Figure 7.

1. Description of Instrumentation for Survey Plots and Correlograms

To produce the 70 mm microfilm plots, the analog signals from the ISEE-1 and -2 tapes are processed by dual Federal Scientific Corporation (now Nicolet Scientific Corporation) UA-6 spectrum analyzers. The outputs of the spectrum analyzers are then processed by a Federal Scientific MCU-2 multifunction computation unit to produce either independent spectrograms (with signal frequency plotted as a function of time), or frequency-time correlograms (with cross-power spectral density of the two input signals plotted as a function of frequency and time). The output of the spectrum analyzers and multifunction computation unit is processed by the 70 mm camera system to record the data on microfilm. For the interferometer studies, the spectrum analyzers are set for a total bandwidth of 0 to 10 kHz. A complete spectrum is produced every 0.025 sec and consists of 250 frequency channels with a bandwidth (resolution) of 40 Hz. The 70 mm camera system is operated at a film speed of 1/8 inch per second. When the multifunction computation unit is operating in the independent spectrum analysis mode, spectrograms for each satellite are produced. An example of the independent spectrograms for both ISEE-1 and

-2 is shown in the top half of Figure 8. When the multifunction computation unit is operated in the cross-power spectral density mode, a correlation of the two input signals is performed over each of the 250 frequency channels. The density of the plot is a combination of the signal intensities and the phase (degree of correlation or anti-correlation) of the two input signals. High intensity signals which are in-phase can be most clearly identified in the frequency-time correlogram shown in the third panel of Figure 8. Only correlated signals whose phase difference is within the range of $\pm 90^\circ$ are displayed in this correlogram. A frequency-time correlogram which displays signals which are anticorrelated (180° out-of-phase) is also produced (shown in the fourth panel of Figure 8); however, for this interferometer study the out-of-phase correlogram gives redundant information and is not used.

2. Description of Instrumentation for Detailed Spectral Plots

The instrumentation used to produce the detailed spectral plots consists of a Nicolet Scientific UA-500A spectrum analyzer with digital outputs, and a microcomputer to record the spectra. The digital outputs provide the amplitude of spectral data with an accuracy of better than 0.1 percent. For this interferometer study the spectrum analyzer was operated in a mode giving a 500 point spectra over a total bandwidth of 10 kHz every 50 msec. The individual frequency channels have a bandwidth of 20 Hz and a filter time constant (time

resolution) of 50 msec. Microcomputer hardware constraints limit the amount of data that can be continuously acquired to approximately 80 complete spectra over a four-second time interval. An example of the spectra produced by the UA-500A spectrum analyzer is shown in Figure 9. The vertical scale is an arbitrary scale proportional to the square root of the power spectral density (volts/ $\sqrt{\text{Hz}}$) of the input signal, and the horizontal scale is the frequency of the input signal. The computer interface synchronizes the data acquisition with the decoded time code recorded on the analog tape. The acquisition of data can be started within 50 msec of the desired time.

3. Description of the Correlator System

The correlator system consists of three elements: a variable signal delay circuit, quadrature phase shifters, and dual one-bit correlators. Two types of signal delay circuits have been developed to delay the signals, one using analog technology and the other using digital technology. The first delay circuit uses a charge-coupled analog delay line which is clocked at different frequencies to provide a signal delay from 0 msec to 10 msec, in increments of 100 μsec . To achieve a higher time resolution, the charge-coupled delay line is connected to an analog delay line which provides delays from 0 to 100 μsec , in increments of 1 μsec . The digital delay line was developed to delay the signals for longer delays than what was possible with the analog delay line. The digital delay line samples the clipped (one-bit digitized) data at a rate of one sample per μsecond , and

stores the sample data in digital memory. The sample is then read from the memory after the desired number of μ seconds has elapsed. Delays up to 65 msec are possible with a sampling rate of 1 MHz. A computer interface is also connected to the digital delay line to allow the one-bit digitized data to be written to a disk. Micro-computer hardware constraints limit the sampling rate of the one-bit data to one sample every 7 μ sec (for each signal), and the total amount of data acquired, to approximately 1.3 sec. Correlations as a function of both delay and time can be generated from these computerized data. The computer-generated delay-time correlograms clearly show the correct delay for maximum correlation, and also show the phase differences between the two input signals. An example of the delay-time correlogram for a test signal with a white-noise power spectral density is shown in Figure 10.

The quadrature phase shifter provides two outputs, with a 90° phase difference, for each analog signal. The two outputs are accurate to within about 5° of the desired 90° phase difference over the 10 kHz bandwidth.

Correlations are performed with two one-bit correlators. For random noise signals, one-bit correlators have the advantage of producing an output which is normalized to between -1 and +1, but with a reduced signal-to-noise ratio [Weinreb, 1963; Dulk, 1970]. Additionally, the output from a one-bit correlator must be corrected by the term

$$\rho_m = \sin\left(\frac{\pi}{2} C_0\right) \quad , \quad (2)$$

where ρ_m is the measured correlation and C_0 is the value of the correlation from the one-bit correlator [Van Vleck, 1943; Weinreb, 1963].

The output of the correlator is filtered by a low-pass filter, to provide time-averaging of the instantaneous correlation and to remove the $2 \times \omega$ frequency terms. The time constant of the low-pass output filter is 10 msec. The time-averaged correlation is recorded on a strip chart recorder. Examples of the correlator output can be found in the bottom two panels of Figure 8.

III. VERY LONG BASELINE INTERFEROMETRY

A. Characteristics of a Cross-Correlation Interferometer

1. Resolving Power of an Interferometer

Interferometers have played an important role in radio astronomy, due to the increased resolving power of an interferometer over that of a single antenna radio telescope. The angular resolving power of a two-element interferometer is normally defined by the minimum lobe spacing of the antenna pattern. A two-element interferometer has a resolution of λ/D , where λ is the wavelength of the radio emission and D is the baseline of the interferometer [Kraus, 1966]. The resolution of a radio telescope with a single circular antenna is $1.22 \lambda/D$, where λ is the wavelength of the radio emission and D is the diameter of the antenna [Born and Wolf, 1965]. Thus, an interferometer has almost the same resolving power as a single antenna whose diameter is equal to the baseline of the interferometer. For a baseline of 5,000 km and a signal frequency of 250 kHz, the ISEE interferometer system has an angular resolution of 2.4×10^{-4} radians. For a typical source-satellite distance of $15 R_E$, an angular resolution of 2.4×10^{-4} radians gives a spatial resolution at the source region of approximately 25 km.

2. Response of an Interferometer

The response of an interferometer to a radio source depends upon the size of the source region, the spectral characteristics of the radio emission, the baseline of the interferometer, and the signal propagation times. The standard procedure with interferometry is to measure the cross-correlation of the received signals at different projected baselines and time delays. The cross-correlation as a function of baseline provides information about the size and structure of the radio source. A two-dimensional brightness distribution of a radio source can be synthesized by taking the two-dimensional Fourier transform of the cross-correlation function, measured at different two-dimensional baselines. The spatial resolution of the synthesized brightness distribution is determined by the maximum projected baselines [Rogers, 1976].

a. Response to a Point Source

For a point radio source, the magnitude of the cross-correlation coefficient is dependent only upon the spectral characteristics of the radio emission and the signal propagation times. The phase of the cross-correlation coefficient is dependent upon the phase and frequency difference between the wideband receiver local-oscillators, the center frequency of the radio emission, and the signal propagation times. Appendix A derives the response of a cross-correlation interferometer to a point radio source with a rectangular-filtered white-noise power spectra, and to a point radio source with a Gaussian-shaped

power spectra. Equation (A-46), the cross-correlation function for signals with a rectangular-filtered white-noise power spectra, and equation (A-51), the cross-correlation function for signals with a Gaussian-shaped power spectra, contain an identical multiplicative cosine term:

$$C_p = \cos[\Delta\omega_0 t + \theta + \omega_0 \tau - \omega_c(\tau - \tau')] \quad , \quad (3)$$

where

$$\theta = \phi_x - \phi_y + \Delta\omega_0(\tau_{s1} + \tau_{s2})/2 - \omega_0(\tau_{g1} - \tau_{g2}) \quad . \quad (4)$$

This cosine term determines the phase of the cross-correlation. In addition to being a function of the source-spacecraft propagation times, equation (3) is also a function of the propagation times and Doppler shifts of the telemetry signal transmitted from the two spacecraft to the ground stations, and the frequency difference between the wideband receiver local-oscillators. The multiplicative $\sin(x)/x$ term in equation (A-46),

$$C_A = \frac{\sin\left[\frac{\Delta\omega}{2}(\tau - \tau')\right]}{\frac{\Delta\omega}{2}(\tau - \tau')} \quad , \quad (5)$$

and the multiplicative Gaussian term in equation (A-51),

$$C_A = \exp[-\Delta\omega^2(\tau - \tau')^2/4\pi] \quad , \quad (6)$$

determine the magnitude of the correlation as a function of delay. Figure 11 is a plot of equation (5), the $\sin(x)/x$ term, as a function of delay, for different signal bandwidths. A negative correlation represents a 180° phase difference between the two signals at the input to the correlator. Figure 12 is a plot of equation (6), the Gaussian term, as a function of delay, for different signal bandwidths. For high correlations, the functions plotted in Figures 11 and 12 are nearly identical. Figure 13 is a plot of the correlation, as a function of delay, for signals with a 6 kHz bandwidth and a rectangular-filtered Gaussian-shaped power spectra. A rectangular-filtered Gaussian-shaped power spectra closely approximates the power spectra of a signal, with a Gaussian-shaped power spectra, that has been received by a receiver with a finite bandwidth or from bandpass filtering of the signal. In Figure 13, the correlation is plotted for different ratios of filter bandwidth (Δf_f) to signal bandwidth (Δf_s). For $\Delta f_f/\Delta f_s = 0$, the power spectral density is nearly identical to a rectangular-filtered white-noise power spectral density, and for $\Delta f_f/\Delta f_s = \infty$ the power spectral density is nearly identical to a Gaussian-shaped power spectral density. For the entire range of $\Delta f_f/\Delta f_s$ ratios, a time delay in the range of 0 to 150 μsec produces a nearly identical (to within 20 percent) reduction in the correlation. From Figures 11, 12, and 13, the absolute time accuracy necessary to maximize the correlation of signals with different bandwidths can be

deduced. A signal with a rectangular-filtered white-noise power spectral density, and a 1 kHz bandwidth, has its correlation reduced by 10 percent for an error of 250 μ sec in time delay. For signals with wider bandwidths, smaller time delays produce a larger reduction in the correlation. Since the typical AKR bursts observed in the frequency range of 125 kHz to 500 kHz are narrower than 2 kHz in bandwidth, it is only necessary to be within $\pm 25 \mu$ sec to have less than a one percent reduction of the correlation.

With the ISEE interferometer system, the largest term in equation (3) which affects the fringe rate (change in phase of the correlation as a function of time) is the wideband receiver local-oscillator frequency difference term ($\Delta\omega_0 t$). The fringe rate is also dependent upon doppler shifts of the signal caused by the motions of the satellites, the earth, and the source region, but these are typically much smaller than the local-oscillator frequency difference term. For the typical satellite baselines used to observe AKR with the ISEE interferometer, the differential Doppler shift caused by spacecraft motion can be as large as 0.25 Hz. This is smaller than the ~ 6 Hz local-oscillator frequency difference at 250 kHz. Rapid motion of the source region, or signal propagation effects, could induce phase changes in the correlation comparable to the wideband receiver local-oscillator frequency difference.

The important conclusions to be drawn from the derivation of an interferometer's response to a point radio source are: (1) the correlation as a function of signal delay is a Fourier transform of

the power spectral density; (2) the correlation, as a function of signal delay, decreases more rapidly for wide bandwidth signals than for narrow bandwidth signals; (3) the correlation, as a function of signal delay, for signals with comparable bandwidths but different shaped power spectral densities, decreases at approximately the same rate (to within 20 percent); (4) any changes in signal characteristics or signal propagation times will affect the phase of the correlation.

b. Response to an Incoherent Source

A two-element interferometer measures one Fourier component of the two-dimensional brightness distribution of the source region for each baseline. Appendix B derives an interferometer's response to an extended incoherent source. The visibility of a source region with a brightness distribution $S(x,y)$ is [equation (B-37)]:

$$v(u,v) = \iint S(x,y) e^{-i2\pi(ux+vy)} dx dy \quad . \quad (7)$$

From equation (7), it can be seen that the complex visibility function v is the normalized Fourier transform of the brightness distribution $S(x,y)$. The complex visibility is a function of the two-dimensional projected baselines u and v (in wavelengths), and the brightness distribution is a function of the angular positions x and y (in radians). If the complex visibility function is measured over the entire uv -plane, it is possible to construct the source's brightness distribution by taking the Fourier transform of the complex visibility

function. In practice, the visibility function is sampled only at discrete points. The maximum baseline in each direction determines the resolution of the synthesized brightness distribution, and the sample spacing determines the angular size of the region mapped. If the phase terms in the sampled complex visibility function are not available, or if the uv-plane is insufficiently sampled, the available data are usually fit to a model brightness distribution. Figure 14 is a plot of the correlation as a function of the projected baseline and angular source size for a Gaussian brightness distribution. The angular size of the source is defined as the angular width between the points where the brightness distribution is reduced by a factor of $1/e$.

c. Response to a Coherent Source

The response of an interferometer to a coherent source is dependent upon the exact details of the interferometer baseline geometry, the brightness distribution of the source, and the spectral characteristics of the radio emission. Some brightness distributions, such as a uniform linear array of in-phase radiating elements, will have a multi-lobed radiation pattern with a 180° phase shift between lobes. The angular size of the lobes is determined by the size of the source region and the frequency of the emission. Thus, for a multi-lobed radiation pattern, abrupt phase changes might be seen in the correlation as lobes sweep past each spacecraft. Since the lobe spacing is also a function of the frequency of emission, wide bandwidth

emissions could be completely de-correlated for certain source-spacecraft geometries [Ratner, 1976].

Other brightness distributions, such as a circular symmetric two-dimensional Gaussian distribution, will have only one lobe with a uniform phase across the entire lobe. For a single lobed radiation pattern, the signals would be only slightly decorrelated for wide bandwidth emissions.

Although interferometry does not directly measure the brightness distribution of a coherent source, it does provide some information about the spatial coherence of the source region.

3. Oscillator Stability

Any phase instability or frequency difference (linear phase drift) between the receiver local-oscillators will decorrelate the received signals. Moran [1976] defines a coherence function

$$A(T) = \left| \left\langle \frac{1}{T} \int_0^T e^{i\phi(t)} dt \right\rangle \right|, \quad (8)$$

where ϕ is the phase difference between the local-oscillators, t the time, and $\langle \rangle$ the expectation value, to measure the phase stability requirement. A coherence value of 1.0 means that phase instability has no effect on the measured correlation, while a coherence value of 0.5 means that the measured correlation will be reduced to 50 percent of the true correlation because of the phase instability. By

neglecting any receiver local-oscillator frequency difference, and assuming that the phase is a Gaussian random variable, the coherence function can be approximated by:

$$A(T) \approx \exp(-\langle \phi^2 \rangle_T / 2) \quad (9)$$

[Moran, 1976]. The stability of frequency standards is usually defined by their fractional stability $(\Delta f/f)T$. The fractional stability is determined by measurements of the phase difference between two oscillators over the time interval T . Since $\phi = 2\pi fT$,

$$\langle \phi^2 \rangle_T = [(\Delta f/f)2\pi fT]^2 \quad (10)$$

Moran [1976] defines the coherence time as the time for which $A(T) = 0.5$ or $\langle \phi^2 \rangle^{1/2} = 68^\circ$. The phase stability of the ISEE crystal-controlled local-oscillators was measured and found to have a short-term phase stability of better than one part in 10^{-6} [Shawhan, 1978]. Thus, the maximum possible coherence time for the ISEE interferometer system is 1.5 sec for a local-oscillator frequency of 125 kHz and 0.75 sec for a local-oscillator frequency of 250 kHz. Because the present analysis technique does not remove the local-oscillator frequency difference prior to performing the correlation, the coherence time is much less than a second. The actual coherence time must include the linear phase drift caused by the receiver local-oscillator

frequency difference. The integrators used in the ISEE interferometer system exponentially weigh the instantaneous correlation in time. Equation (8), when modified to include the frequency difference of the local-oscillators and the exponential weighting of the integrator, becomes:

$$A(T) = \left| \frac{\int_{-\infty}^T e^{t'/T} e^{i2\pi\Delta f_0 t'} dt'}{\int_{-\infty}^T e^{t'/T} dt'} \right|, \quad (11)$$

where T is the time-constant of the integrator and Δf_0 is the local-oscillator frequency difference. Performing the integrals gives the final form for $A(T)$ as:

$$A(T) = (1 + 4\pi^2 \Delta f_0^2 T^2)^{-1/2}. \quad (12)$$

Figure 15 is a plot of the coherence function, for different integration time-constants, and for different local-oscillator frequency distances. A Δf_0 of 3 Hz corresponds to the approximate local-oscillator frequency difference at 125 kHz, and a Δf_0 of 6 Hz corresponds to the approximate local-oscillator frequency difference at 250 kHz. From Figure 15, the coherence time (integrator time constant) for Δf_0 of 3 Hz is 0.092 sec and for Δf_0 of 6 Hz is 0.046 sec. The time constant of the correlator is 0.010 sec; thus, from Figure 15 or equation (12),

the true correlation is approximately 2 to 5 percent higher than the measured correlation. The consequence of using an integration time that is shorter than the coherence time is that the correlation noise is increased.

An analysis of the response of a low-pass filter (integrator) at the local-oscillator frequency differences, as a function of different RC time constants, gives the identical result as equation (12).

Since the stability requirements are independent of the baseline, if the system works at short baselines (i.e., with laboratory test signals), it will work at large baselines (i.e., after the spacecraft have been launched) [Shawhan, personal communication].

4. Tape Recorder Stability

Any fluctuations in the tape recorder speed during the recording or playback process can affect the correlation. Speed fluctuations with a period shorter than the time constant of the correlator will tend to decrease the correlation; while fluctuations with a period longer than the correlator time constant will have the same effect as introducing a variable (time dependent) delay into the correlation, i.e., the magnitude of the correlation will not be decreased, but will be maximized at different delays as a function of time. Laboratory measurements of the tape recorder indicate that low frequency speed fluctuations can shift the delay required for maximum correlation by up to $\pm 15 \mu\text{sec}$. The effect of speed fluctuations are minimized by having the signals from both spacecraft recorded on

adjacent tracks on the same tape. Speed fluctuations affect adjacent tracks almost identically, provided that the signal delay required to maximize the correlation is small compared to the period of the speed fluctuation. The combined effect of all of the tape recorder speed fluctuations is estimated to decrease the correlation by less than 1 percent.

B. Satellite-Satellite Interferometry

Satellite-satellite interferometry uses the same basic techniques as ground-based interferometry, but since the receivers are placed in orbit, there are differences and unique problems associated with data acquisition and data analysis. The limitations imposed by orbiting receivers also places constraints on the types of radio sources which may be observed.

1. Interferometer Baselines

With ground-based VLBI (Very Long Baseline Interferometry), radio telescopes with fixed geographic locations perform interferometry on radio sources. Multiple observatories and/or the rotation of the earth provide different projected baselines. The full range of possible east-west projected baselines occurs within one-fourth rotation of the earth. Multiple baselines in the north-south direction require multiple pairs of observing stations at different latitudes for equatorial radio sources.

The ISEE interferometer system uses a pair of satellites in nearly identical elliptical orbits. The separation of the spacecraft

is controllable, but it requires months to adjust the separation from the minimum to maximum possible projected baselines. Thus, the correlation can be measured only at one baseline for each event. The inclination of the spacecraft orbits limits the reception of events to those which are beamed to latitudes lower than approximately $\pm 40^\circ$ magnetic latitude.

2. Spacecraft Antennas, Receivers, and Transmitters

Since the ISEE interferometer antennas and receivers are mounted aboard spacecraft, there are severe design constraints which must be followed (such as size, weight, and electrical power). These constraints determine the type and sensitivity of the equipment which can be placed in orbit.

a. Receiving Antennas

Weight and size limitations dictated the use of long dipole antennas. Because dipole antennas have a wide beamwidth, it is impossible to direct them away from the source region to measure the background noise levels, and they are not as sensitive as other types of antennas with narrower beamwidths.

b. Wideband Receiver

The ISEE wideband receivers were designed to operate over a large frequency bandwidth and over a large range (~ 100 dB) of signal amplitudes. To cover the necessary 100 dB dynamic range, AGC (Automatic Gain Controlled) receivers were employed. Although the AGC

level is digitally sampled and available with the digital data, the time constant of the AGC is much shorter than the digital sampling rate. Thus, it is impossible to know the gain of the receiver at all times. Since the uncorrelated noise on the analog data tapes consists of noise which is gain dependent (background noise levels, spacecraft interference, and preamplifier noise), and noise which is gain independent (telemetry noise and tape recorder noise), correcting the correlation for the signal-to-noise ratio is difficult. Since individual AKR bursts are narrower in frequency than the bandwidth of the wideband receiver, the system noise level can be estimated by examining the signal levels at frequencies which do not contain the AKR burst.

The local-oscillators used in the ISEE wideband receivers are crystal controlled. Crystal oscillators have good short-term phase stability but drift in frequency with age and temperature, making it impossible for both receivers to have exactly the same local-oscillator frequency. The local-oscillator frequency difference puts an upper limit on the correlator integration time constant. This integration time constraint is not a severe problem since typical AKR bursts last for several seconds or less and can change in frequency or bandwidth on even shorter time scales. Short integration times do, however, increase the noise in the correlation. The difference in local-oscillator frequencies produces a very noticeable fringe in the correlation at the difference frequency, making it much easier to

detect the fringe [Hanbury Brown et al., 1955] and determine the correct delay to maximize the correlation.

c. S-band Analog Transmitter

Electrical power available to the S-band telemetry transmitters aboard each spacecraft limits the transmitter bandwidth to 10 kHz for the typical interferometer baselines used.

3. Telemetry Station Recording Equipment

Data acquisition at each of the many NASA telemetry stations required the use of existing equipment. The use of specialized equipment, such as analog or digital tape recorders with video frequency bandwidths and precisely aligned rubidium-controlled clocks (with time synchronization on the order of 1 μ sec), could not be used.

The bandwidth of the analog tape recorders used in the ISEE interferometer system is 100 kHz at a tape speed of 15 ips. At each telemetry station, the time code is generated by a Cesium frequency standard and is recorded on the data tape with an absolute time accuracy of better than $\pm 25 \mu$ sec.

4. Operational Constraints

To detect AKR, both spacecraft must be within the AKR emission cone when AKR is being generated. To perform interferometry, both spacecraft must be commanded to the same wideband receiver mode and the telemetry stations must be scheduled to record the analog data. For the data from both spacecraft to be recorded on the same analog

tape (which provides the best possible time alignment of the data and currently are the only data that can be analyzed), the same telemetry station must be capable of receiving data from both satellites simultaneously. At some of the longer baselines, data from both spacecraft could not be recorded on the same tape.

5. Types of Observable Sources

The characteristics of the ISEE interferometer system limits the types of observable sources to bursts which have a high intensity relative to the background noise, are narrow in frequency compared to the bandwidth of the system, and have a duration of approximately one second. These burst characteristics give the data a good signal-to-noise ratio (which allows short integration times), allows the correlation to be corrected by the signal-to-noise ratio, and gives multiple fringes over the duration of the burst (which makes the correlation highly visible). Individual AKR bursts have the signal characteristics which are necessary to accurately measure the correlation.

IV. METHOD OF ANALYSIS

A. Introduction

The structure of AKR bursts is extremely complex and diverse [Gurnett et al., 1979; Gurnett and Anderson, 1981; Calvert, 1982]. To simplify the analysis and interpretation of the data, bursts were chosen which meet the following criteria: (1) a burst duration of several seconds, (2) relatively constant burst frequency, (3) high burst intensity, and (4) isolation from other AKR bursts or spacecraft interference.

1. Burst Duration

For a wideband receiver frequency of 125 kHz, the difference in the local-oscillator frequencies is approximately 3 Hz. Thus, a burst lasting several seconds will have at least four or five complete fringes in the correlogram. Having a large number of fringes makes it easier to determine the maximum correlation and gives a more accurate statistical result.

2. Constant Burst Frequency

With bursts nearly constant in frequency, it is possible to increase the signal-to-noise ratio by filtering out the background noise. Because of the limited number of events available at long baselines, some events analyzed were not constant in frequency.

3. High-Intensity Bursts

High-intensity bursts have a much higher signal-to-noise ratio than lower intensity bursts. The error in determining the signal-to-noise ratio is greater for low signal-to-noise ratios; thus the correlation for bursts with high signal-to-noise ratios will have a smaller error.

4. Isolation From Other Bursts and Interference

Any uncorrelated signal, such as spacecraft interference, will reduce the correlation. Since AKR bursts generated at different source region locations would require a different amount of delay to maximize the correlation, multiple bursts would decorrelate each other.

B. Determination of the Correct Delay

Two methods to determine the signal delay necessary to maximize the correlation have been developed. The first method determines the correct delay by measuring the slope of the striations in the frequency-time correlograms, and the second method uses the delay-time correlogram to determine the correct delay.

1. The Frequency-Time Correlogram Method

A two-step process is used to determine the signal delay which maximizes the correlation. First, the slope of the striations on the frequency-time correlogram is measured to determine the approximate delay required to maximize the correlation. Second, the correlation is measured with different delays near the value determined by measuring

the slope of the striations (typically within ± 200 μsec of estimated delay) until the correlation is maximized. For a delay increment of 25 μsec , the correct delay can be determined to within ± 12.5 μsec .

Figure 16 shows a series of frequency-time correlograms produced by delaying a signal that has a white-noise power spectral density, by different amounts, prior to correlating. Under each frequency-time correlogram in Figure 16 is the value that the ISEE-1 signal was delayed to produce that correlogram, and the slope of the striations that were produced. The data for these correlograms were obtained during spacecraft integration by applying identical white-noise signals to the antenna inputs on both spacecraft. Table 1 shows the slope of the striations in correlograms for signal delays in the range of ± 6.0 msec. These results can be explained by examining equation (3). Since the striations in Figure 16 represent lines of constant phase as a function of time and frequency, it is possible to use the slope of the striations to determine the desired delay. For these lines of constant phase:

$$\phi_c = \text{const} = \Delta\omega_0 t + \theta + \omega_0 \tau - \omega(\tau - \tau') \quad . \quad (13)$$

Solving equation (13) for ω gives the equation of the lines of constant phase:

$$\omega = \frac{\Delta\omega_0}{(\tau - \tau')} t + \frac{(\theta + \omega_0 \tau - \phi_c)}{(\tau - \tau')} \quad . \quad (14)$$

Thus, the slope $\Delta\omega/\Delta t$ of the lines of constant phase in the frequency-time correlogram is:

$$\frac{\Delta\omega}{\Delta t} = \frac{\Delta\omega_0}{(\tau - \tau')} \quad . \quad (15)$$

By measuring the slope of the lines of constant phase it is possible to determine $(\tau - \tau')$. From equations (5) and (6), the magnitude of the correlation is maximized when $(\tau - \tau') = 0$, and from equation (15), the slope of the striations is infinite when $(\tau - \tau') = 0$. Figure 17 is a plot of the reciprocal of the striation slope for different amounts of signal delay. A least squares fit to the data in Table 1 and Figure 17 gives:

$$\left(\frac{\Delta\omega}{\Delta t}\right)^{-1} = -0.536(\tau + 0.087) \quad (16)$$

as the equation for $(\Delta\omega/\Delta t)^{-1}$ as a function of delay. It can be shown that correct scaling for the slope of the striations in the correlogram can be accomplished by measuring $\Delta\omega_0$ in units of fringes per unit length along the time axis divided by frequency in kHz per unit length along the frequency axis, and τ in units of msec. After compensating for the error in the delay line (1.000 msec on the dial of the delay line is actually 1.086 msec), there is a 0.5 percent difference between the experimental and theoretical values of $(\Delta\omega/\Delta t)$. The

frequency-time correlogram predicts the highest correlation with a delay of $-87 \mu\text{sec}$ for this white-noise test signal. This $87 \mu\text{sec}$ offset is probably caused by misalignment of the tape recorder heads used to record and play back the data.

The frequency-time correlogram can be used to calculate the correct delay for delays up to approximately $\pm 10 \text{ msec}$. For larger delays, the striations become almost horizontal and merge together.

2. Delay-Time Correlogram Method

The delay-time correlogram was developed to determine the correct delay for delays greater than $\pm 10 \text{ msec}$. The delay-time correlogram is a correlogram consisting of a large number of correlations, each at a different delay, plotted together as a function of delay and time. The magnitude of the correlation is plotted as intensity, with black representing a large positive correlation and white representing a large negative correlation. Figure 10 is a delay-time correlogram for the same white-noise test signal that was used to produce the correlograms in Figure 16. In Figure 10, high correlations are found between delays of $-175 \mu\text{sec}$ and $60 \mu\text{sec}$, with the highest correlation at a delay of $-60 \mu\text{sec}$. Individual correlations near the correct delay can be examined to determine the delay which maximizes the correlation. With a signal sampling rate of one sample every $7 \mu\text{sec}$, the correct delay can be determined to within $\pm 3.5 \mu\text{sec}$.

The slope of the striations, and the change in correlation as a function of delay observed in delay-time correlograms, can be explained by examining equations (3), (4), (A-46), and (A-51).

a. Slope of the Striations

If the signal propagation times remain constant, θ in equations (3) and (4) and τ' in equation (3) are constants. For constant θ and τ' , equation (3) becomes:

$$C_p' = \cos(\Delta\omega_0 t - \omega_c' \tau + \theta') \quad , \quad (17)$$

where θ' is a constant, and $\omega_c' = (\omega_c - \omega_0)$. ω_c' is the down-converted center frequency of the burst, and is in the frequency range of 0 to 10 kHz. Solving equation (17) for the lines of constant phase gives:

$$\tau = \frac{\phi_c - \Delta\omega_0 t}{\omega_c'} \quad . \quad (18)$$

Thus, the slope $\Delta\tau/\Delta t$ of the lines of constant phase is:

$$\frac{\Delta\tau}{\Delta t} = - \frac{\Delta\omega_0}{\omega_c'} \quad , \quad (19)$$

the period T_t of the fringes along the time axis is:

$$T_t = 2\pi/\Delta\omega_0 \quad , \quad (20)$$

and the period T_τ of the fringes along the delay axis is:

$$T_{\tau} = 2\pi/\omega'_c \quad . \quad (21)$$

b. Decrease in Correlation as a Function of Delay

From equations (A-46) and (A-51), it can be seen that the correlation as a function of delay is the Fourier transform of the power spectral density. In general the correlation will be a maximum when $(\tau - \tau') = 0$, and will decrease from the maximum value at a rate that is dependent upon the bandwidth of the signals. The correlation will decrease more rapidly for wide bandwidth signals than for narrow bandwidth signals.

The delay-time correlogram provides, as a function of time, information about (1) the value of the maximum correlation, (2) the delay required to maximize the correlation, (3) the phase of the correlation, (4) the center frequency of the burst, and (5) the bandwidth of the burst.

C. Correction for One-bit Digitization

The correlation measured with a one-bit correlator differs from the measured correlation ρ_m by the relation:

$$\rho_m = \left[\sin^2\left(\frac{\pi}{2} C_0\right) + \sin^2\left(\frac{\pi}{2} C_{90}\right) \right]^{1/2} , \quad (22)$$

where C_0 and C_{90} are the quadrature outputs of the correlator [Weinreb, 1963]. In theory, equation (22) is valid only for signals

with Gaussian amplitude distributions. The response of a one-bit correlator to noise with non-Gaussian amplitude distributions has been investigated by Ochs [Dulk, 1970] and was found to have an error of several percent, except that in the case of repetitive waveforms with spiked distribution functions the error was much larger than a few percent.

D. Determination of Signal-to-Noise Ratio

To obtain the true correlation ρ of the burst, the measured correlation ρ_m must be multiplied by a factor to correct for the signal-to-noise ratio, i.e.,

$$\begin{aligned}\rho &= \left[\left\langle \frac{S_1^2}{S_1^2 + N_1^2} \right\rangle \cdot \left\langle \frac{S_2^2}{S_2^2 + N_2^2} \right\rangle \right]^{-1/2} \rho_m \\ &= \left[\left\langle \frac{S_1^2}{V_1^2} \right\rangle \cdot \left\langle \frac{S_2^2}{V_2^2} \right\rangle \right]^{-1/2} \rho_m \quad .\end{aligned}\tag{23}$$

S_1 and S_2 are the signal voltages of the correlated burst, N_1 and N_2 are the voltages of the uncorrelated background noise, and V_1 and V_2 are the total voltages contained in the signals from ISEE-1 and ISEE-2 [Rönnäng, 1971].

To measure the signal-to-noise ratio of the bandpass filtered signals, detailed spectral plots are produced for both the unfiltered signals and the bandpass filtered signals from both satellites. The

spectra of the unfiltered signals is used to estimate the noise power contained within the frequency range of the burst and the signal voltage contained in the burst. The noise power within the bandwidth of the burst is estimated by computing the power spectral density of the background noise at frequencies above and below the frequency of the burst, interpolating these values to the center frequency of the burst (assuming the power spectral density is a linear function of frequency), and then multiplying by the bandwidth of the burst. The signal voltage of the burst is computed by taking the square root of the difference between the power contained within the bandwidth of the burst and the noise power contained within the bandwidth of the burst. The total power of the filtered signals is computed by integrating the power spectral density over the full 10 kHz receiver bandwidth. V_1 and V_2 are the square roots of the total power contained in the bandpass filtered signals. To estimate the error in the signal-to-noise correction factor, the correction factor was computed several times for five of the events and was found to be consistent within 5-10 percent. The error in the correction factor was largest for the events with low signal-to-noise ratios.

Figure 9 shows the spectrum of the unfiltered signal and the bandpass filtered signal from a narrow bandwidth AKR burst observed on February 27, 1978 at 1241 UT. For this burst the uncorrelated background noise is assumed to be in the frequency ranges of 125.0 kHz to 131.0 kHz and 131.15 kHz to 135.0 kHz; the frequency range of the burst is assumed to be from 131.00 kHz to 131.15 kHz. Comparison of

the correlograms for the filtered and unfiltered signals in Figure 8 shows that the signal-to-noise ratio can be greatly improved by band-pass filtering.

E. Field-Aligned Coordinate System

To measure the baseline dimensions, the origin and orientation of the source centered coordinate system must be determined. Since AKR bursts may originate anywhere along the auroral oval, and the actual position of individual bursts could not be determined, the origin of the source centered coordinate system was chosen to be along a 70° magnetic latitude field line at 21.0 MLT. Since the viable theories for the generation of AKR predict the radiation to be generated at slightly above the local gyrofrequency, the altitude of the coordinate system was chosen to be at the altitude where the local gyrofrequency equaled the observing frequency. Thus, the origin of the source-centered coordinate system was chosen to be the location where the probability of occurrence for AKR is peaked [Kurth et al., 1975; Kaiser and Alexander, 1976; Gallagher and Gurnett, 1979; Green and Gallagher, 1985]. As shown in Figure 18, the z axis of the source centered coordinate system is aligned along the source-satellite line, and the y axis is aligned so that the magnetic field (or gradient of the magnetic field, if desired) is in the y-z plane. The error in the projected baseline caused by uncertainty in the source location is estimated to be less than 10 percent.

F. Normalization of Source-Satellite Distance

Unlike ground-based astrophysical interferometry where the source region is effectively at infinity, the correlations of terrestrial signals measured with satellite-satellite interferometry must be corrected for the differing source-satellite distances. Typical source-satellite distances range from approximately $6 R_E$ to more than $20 R_E$. For the calculation of the statistical source size, the correlation coefficients were normalized to $20 R_E$.

If the source region is assumed to have a two-dimensional Gaussian brightness distribution, the angular source size can be computed for an individual burst. Since the visibility is the Fourier transform of the brightness distribution [Rogers, 1976], the equation for the correlation as a function of angular source size for a Gaussian brightness distribution, is:

$$\rho = e^{-(\pi b \alpha / 2)^2} \quad , \quad (24)$$

where b is the projected baseline in wavelengths and α the angular width between the points where the brightness distribution is down by a factor of $1/e$. Solving equation (24) for the angular source size at the source-satellite distance r_0 , and using the relation:

$$r_0 \alpha_0 = r_n \alpha_n \quad , \quad (25)$$

the angular source size α_n , at the normalized distance r_n , can be shown to be:

$$\alpha_n = \frac{2\sqrt{-\ln \rho_0}}{\pi b} \frac{r_0}{r_n}, \quad (26)$$

where ρ_0 is the correlation measured at the source-satellite distance r_0 . Substituting equation (26) into equation (24) gives the equation for the normalized correlation:

$$\rho_n = \exp \left\{ - \left[\pi b \left(\frac{2\sqrt{-\ln \rho_0}}{\pi b} \frac{r_0}{r_n} \right) / 2 \right]^2 \right\} = \rho_0^{(r_0/r_n)^2}, \quad (27)$$

where ρ_n is the correlation normalized to the source-satellite distance r_n . The normalized correlation represents the correlation that would have been measured if the source-satellite distance was $20 R_E$ instead of the actual source-satellite distance, with the same baseline.

G. Calculation of Statistical Source Size

With the normalized correlation from many different AKR events plotted as a function of baseline, a statistical source size may be calculated by fitting the data to a model brightness distribution. Gaussian-shaped components are commonly used for model fitting because the brightness distributions of a number of astrophysical radio sources

approximate a Gaussian and Gaussians have convenient Fourier transforms [Fomalont and Wright, 1974]. A Gaussian-shaped brightness distribution [equation (24)] was chosen for the AKR source region model.

H. Calculation of Spectral Density and Brightness Temperature

The AGC levels of the wideband receiver can be used to determine the electric-field strength at each satellite, over the full 10 kHz signal bandwidth, and to calibrate the scale on the detailed spectral plots. The peak spectral density, used in the calculations of source region spectral density and brightness temperature, is the average of the maximum spectral densities found on each spectrogram, during periods of high signal correlation. The primary cause of error in determining the spectral densities is the slow digital sampling rate of the AGC levels. Over a several second interval, the AGC levels indicate that the electric-field strength can change by a factor of 2.5.

If the AKR burst has a signal bandwidth that is large, compared to the 20 Hz spectrum analyzer resolution, the calculated spectral densities are accurate to several percent. If the bandwidth of the AKR burst is less than 20 Hz, the calculated values represent a lower limit to the actual spectral density.

The source region spectral densities are computed by extrapolating the spectral density detected by the spacecraft to the radius of the source region, determined from the correlation measurements (assuming an incoherent source with a Gaussian brightness distribution).

The Rayleigh-Jeans law gives the flux density s as

$$s = \iint \frac{2kT(\theta, \phi)}{\lambda^2} d\Omega \quad , \quad (28)$$

where k is Boltzmann's constant, $T(\theta, \phi)$ is the brightness temperature as a function of angular position, $d\Omega$ is an infinitesimal element of solid angle, and λ is the wavelength [Kraus, 1966]. Assuming the Gaussian brightness distribution:

$$T(\theta, \phi) = T_b e^{-4r^2/\alpha^2} \quad , \quad (29)$$

where T_b is the central brightness temperature and α is the angular width (between the points where the brightness is reduced by a factor of $1/e$) of the brightness distribution, the flux density can be integrated to get the brightness temperature as a function of measured spectral density:

$$T_b = \frac{2s\lambda^2}{\pi k \alpha^2} \quad . \quad (30)$$

For wide bandwidth signals, the computed brightness temperature is within a factor of 6 of the actual brightness temperature, and for very narrow bandwidth signals the actual brightness temperature could be orders of magnitude higher.

V. DISCUSSION OF THE EVENTS

A. Characteristics of the Bursts

The structure of AKR bursts is complex and diverse [Gurnett et al., 1979; Gurnett and Anderson, 1981; Calvert, 1982]. AKR bursts often consist of discrete narrowband emissions that increase or decrease in frequency, as a function of time. Gurnett and Anderson [1981] attribute the drifting tones to disturbances propagating along auroral field lines at the ion-acoustic speed. Calvert [1982] explains the discrete structure of AKR bursts as properties of amplification with feedback, i.e., a natural radio laser. The bandwidth of the bursts can vary from less than 20 Hz to over several kHz. Figure 9 shows the spectrum of a very narrow bandwidth AKR event, with a center frequency of 131.1 kHz, detected by ISEE-1 and -2 on February 27, 1978 at 1322:13.9 UT.

The analyzed events are broken into two classes: (1) events with projected baselines less than 1000 km, and (2) events with projected baselines greater than 1000 km. The short baseline events were detected at a wideband receiver frequency of 125 kHz, and the long baseline events were detected at a wideband receiver frequency of 250 kHz. Since the angular resolution of an interferometer is inversely proportional to the projected baseline, the long baseline events determine the resolution of the interferometer.

1. Short Baseline Events

Figures 8, 19, and 20 are spectrograms and correlograms for a series of AKR events detected on June 12, 1978 by ISEE-1 and -2. The projected baseline for these events is 496 km. The top two panels in Figure 8 show the spectra of the signals received by ISEE-2 and -1. From 1725:05 to 1725:15 UT, the AKR burst is nearly constant in frequency and has a very narrow bandwidth. At 1725:15 UT, the emission at 130 kHz abruptly stops, and simultaneously an emission begins at a frequency of approximately 132.5 kHz.

Figures 19 and 20 show other segments of the AKR bursts detected by ISEE-1 and -2 on June 12, 1978. In Figure 19, at 1724:05, 1724:41, and 1724:45 UT, the AKR emission splits into two components. The bottom two panels in Figure 19 show the uncorrected correlation of the signals in the full 10 kHz receiver bandwidth, and the uncorrected correlation for the signals between 130.5 kHz and 132.5 kHz. The uncorrected correlation goes from 50 percent, for all signals and noise within the 10 kHz receiver bandwidth, to 70 percent, when the background noise is filtered from the signals.

The third and fourth panels in Figure 20 show frequency-time correlograms for the June 12, 1978 events. Between 1724:00 and 1724:05 UT, and between 1724:40 and 1724:45 UT, nearly vertical striations are found in the frequency-time correlograms. The nearly vertical striations indicate that the signals are close to being correctly time aligned. The bottom two panels of Figure 20 show the uncorrected correlation for the burst. The correlation decreases between 1724:46 and 1724:48 UT. This interval corresponds to the time when there are

two frequency components present. If these two frequency components originate at different source locations, the correlation would be expected to be lower. The true correlation, after filtering the background noise from the bursts, correcting for the signal-to-noise ratio (equation 23), and correcting for the one-bit correlator response (equation 2), is 89 ± 4 percent.

2. Long Baseline Events

Figures 21 and 22 are spectrograms of AKR bursts detected by ISEE-1 and -2, in the 250 kHz wideband channel, on February 20, 1979. Seven of these bursts were chosen to be analyzed. The bursts that were chosen are representative of the different characteristics seen in the AKR spectra. Bursts with rapid changes in frequency, as a function of time, were not analyzed because of the difficulty in measuring the correlation over a fraction of a fringe period and correcting for the signal-to-noise ratio. The projected baselines for the events detected between 0035 and 0055 UT are between 3801 and 3868 km, and the projected baselines for the events detected between 0305 and 0315 UT are between 3251 and 3260 km.

a. Day 51, 1979, 0038:15 to 0038:19 UT

The top two panels of Figure 21 show an AKR burst, detected from 0038:09 to 0038:21 UT, that is slowly increasing in frequency and has a bandwidth of approximately 1 kHz. The horizontal line at 252.5 kHz on the ISEE-2 spectrogram is caused by spacecraft interference. The true (corrected) correlation for this burst is 45 percent.

b. Day 51, 1979, 0041:21.5 to 0041:25.5 UT

The middle two panels of Figure 21 show the second burst analyzed. This burst, detected from 0041:16 to 0041:26 UT, has an average bandwidth of less than several hundred hertz, and remains relatively constant in frequency. Figures 23 and 24 show delay-time correlograms for this event. The correlograms show the correlation for all signals within the 10 kHz bandwidth of the receiver. The value of the correlations, shown in Figures 23 and 24, is the output of the one-bit correlator and has not been corrected for the signal-to-noise ratio (equation 23) or for the one-bit correlator response (equation 2). The true correlation, after bandpass filtering of the signal, correcting for the signal-to-noise ratio, and correcting for the one-bit correlator response, is 99 percent. Over certain time intervals, the slope of the striations is uniform, but there are also some very abrupt phase changes in the correlation. These abrupt phase changes are indicative of rapid changes in one or more of the signal propagation times. Changes in the phase of the correlation could be caused by either signal propagation effects or some real change in the source region. Since this AKR burst has a narrow bandwidth, the correlation decreases very slowly as a function of delay. The bandwidth of the burst can be estimated by measuring the rate the correlation decreases, as a function of delay. The decrease in the correlation, as a function of delay, was measured at the times when the correlation was the highest (0041:21.9, 0041:22.8, and 0041:23.5 UT) and was found to decrease by an average of 5 percent, over a 7 msec change

in delay. From equation (6), the bandwidth of this event is less than 20 Hz at these times. Another feature shown in Figure 23, at 0041:21.5 and 0041:21.7 UT, is a beating of two correlation fringes, which have different frequencies, as a function of delay. From equation (21), the down-converted center frequency of the signals can be determined by the fringe period, along the delay axis. The periods of the two fringes, measured on Figure 23, are 0.289 msec and 0.103 msec, corresponding to down-converted center frequencies of 3.47 kHz and 0.974 kHz. Examination of the spectrograms for this event, shown in Figure 21, shows signals at approximately 253.4 kHz and 251.2 kHz (with down-converted center frequencies of 3.4 kHz and 1.2 kHz) for these times. When correlograms were produced, for the frequency interval of 250 to 252 kHz, this beating disappeared.

c. Day 51, 1979, 0051:30 to 0051:34 UT

The bottom two panels of Figure 21 show the third burst analyzed. This burst, detected from 0051:30 to 0051:34 UT, has an average bandwidth of approximately 250 Hz. There is a portion of the burst, at 0051:32 UT, where the bandwidth becomes very narrow. The delay required for maximizing the correlation of this event is 68.40 msec, and the delay predicted, from the assumed source region location (along a 70° Mlat field line located at 21.0 hrs MLT) and the known spacecraft and NASA telemetry station locations, is 68.92 msec. A 520 μ sec difference between the measured and predicted delays is consistent with a source region located in the auroral region. The true (corrected) correlation for this burst is 93 percent.

d. Day 51, 1979, 0307:42 to 0307:46 UT

The top two panels of Figure 22 show the fourth burst analyzed. This burst was detected by ISEE-1 and -2 from 0307:39 to 0307:56 UT. The center frequency of the burst is rising at a rate of 300 Hz sec^{-1} . Assuming emission at the electron gyrofrequency and a dipole magnetic field, the radial component of the source velocity along a magnetic-field line can be determined from the rate of frequency drift. Gurnett and Anderson [1981] approximate the source region velocity, as a function of frequency drift with the equation:

$$\frac{dR}{dt} = -\frac{R_E}{3} \left(\frac{f_{go}^{1/3}}{f^{4/3}} \right) \left(\frac{df}{dt} \right), \quad (31)$$

where $f_{go} \approx 1.7 \text{ Mhz}$ is the electron gyrofrequency at the surface of the earth in the auroral region. From equation (31) this rate of frequency change corresponds to a radial source region velocity of 4.8 km sec^{-1} . The true (corrected) correlation for this burst is 59 percent.

e. Day 51, 1979, 0308:10 to 0308:14 UT

The two middle panels in Figure 22, show the spectrograms for the fifth analyzed burst. This event is first detected by ISEE-1 and -2 at approximately 0307:57 UT, and extends to approximately 0308:27 UT. This event starts as a series of very short vertical pulses, with approximately a 1 kHz bandwidth, at nearly the same frequency. At approximately 0308:10 UT the vertical pulses form a continuous

emission for several seconds. The center frequency of the continuous emission appears to fluctuate in a cyclic fashion, with a period of about 0.3 sec. Figure 25 is a delay-time correlogram for this event. This correlogram shows two important features. The decrease in the correlation as a function of delay is clearly evident. The delay for maximizing the correlation of this event is 55.45 msec, and the delay predicted, from the assumed source region location (along a 70° Mlat field line located at 21.0 hrs MLT) and the known spacecraft and NASA telemetry station locations, is 55.70 msec. A 250 μ sec difference between the measured and predicted delays is consistent with a source region located in the auroral region. The bandwidth of the event appears to change rapidly. From equation (6), and the measured change in correlation as a function of delay, the bandwidth of this event can change from 30 Hz to over 500 Hz in a fraction of a second. The spectrogram for this event, shown in the middle panel in Figure 24, also indicates that the bandwidth of the signal is fluctuating. The uniform striations that are expected to be observed when the correlation is maximized are observed in the correlogram for this event (Figure 25). The true (corrected) correlation for this burst is 81 percent.

f. Day 51, 1979, 0308:32 to 0308:36 UT

The middle two panels of Figure 22 show spectrograms for this event. The characteristics of this burst are similar to the burst analyzed from 0308:10 to 0308:14 UT. The same bursty nature is

observed and the center frequency of the burst also appears to fluctuate cyclically. The true (corrected) correlation for this event is 84 percent.

g. Day 51, 1979, 0311:20 to 0311:24 UT

The bottom two panels of Figure 22 show spectrograms for the seventh analyzed burst. This event is relatively intense (the background noise and spacecraft interference, in the ISEE-2 spectrogram, disappears when the gain of the wideband receiver decreases for large signal amplitudes), and increases in frequency uniformly, at a rate of 2.5 kHz per second. The bandwidth of this event is approximately 2 kHz. The bursty characteristics found in the two events between 0308:00 and 0309:00 UT, is absent in this event.

Figure 26, a delay-time correlogram for this event, shows another important feature found in the delay-time correlograms. The vertical spacing of the fringes is dependent upon the center frequency of the burst. The frequency of this burst increases uniformly with time, and thus the vertical spacing of the fringes decreases in time. Near 0311:20 UT the fringe period, along the delay axis, is 1.07 msec, and near 0311:21.3 UT the fringe period, along the delay axis, is 0.3 msec. From equation (21), a period of 1.07 msec corresponds to a down-converted center frequency of 935 Hz, and a period of 0.3 msec corresponds to a down-converted center frequency of 3.3 kHz. Near 0311:21.2 UT, this correlogram shows a region of uniform striations and a higher correlation, indicating the correct signal delay for

maximizing the correlation. The spectrogram for this event, shown in the bottom panels of Figure 24, shows that the signal bandwidth is approximately 2 kHz. The true (corrected) correlation of this event is 56 percent.

B. The Size of the AKR Source Region

Correlations of AKR bursts, at 125 kHz and 250 kHz, were measured for baselines up to 3868 km. High correlations were measured at all baselines, with narrow bandwidth bursts having the highest correlation and wider bandwidth bursts having a lower correlation.

1. The Statistical Source Size of the AKR Source Region

If the source region of AKR is assumed to have a specific brightness distribution, the statistical size of the source region may be computed. For the analysis of the AKR source region size, the brightness distribution is assumed to be a circularly symmetric Gaussian [equation (29)]. Figure 27 is a plot of the correlation, as a function of baseline, for all of the events analyzed. Each point represents the average correlation of the bursts analyzed at each baseline. To correct for the different source-satellite distances at each baseline, the correlations were normalized to a $20 R_E$ source-satellite distance with equation (27). To normalize the correlations to the same source-satellite distance, the radiation is assumed to be incoherent and the source region is assumed to have a Gaussian brightness distribution. The normalized data were least-squares fit to

equation (24), the correlation as a function of angular source size and baseline for a Gaussian brightness distribution. The result of the least-squares fit gives a statistical source diameter of 9.27 km. A least-squares fit to a straight line was also performed, and gave the result:

$$\rho = -3.22 \times 10^{-6}b + 0.895 \pm 0.07, \quad (32)$$

where ρ is the correlation and b is the baseline. Equation (32) shows that there is only a very small decrease in the correlation as a function of baseline.

The results of the calculations for the statistical source size are based upon the following assumptions: (1) The radiation is incoherent; and (2) The AKR source region is circularly symmetric with a Gaussian brightness distribution. Although a Gaussian brightness distribution was used to fit the data, the results would not differ significantly for other brightness distributions with one central maximum.

The results of the calculations indicate that: (1) The statistical source diameter of AKR bursts is less than 10 km; and (2) The correlation does not decrease significantly as a function of baseline.

C. The Source Size of the Individual Bursts

If the radiation is assumed to be incoherent and to have a Gaussian brightness distribution, the source size of individual bursts can be computed by solving equation (24) for the angular source size α as a function of correlation ρ and baseline b . The source size was computed for all seven of the long baseline events analyzed.

Table 2 lists the time of the event, the baseline parameters, the correlation of the event, and the calculated source diameter for each of the seven events. The calculated source diameters were in the range of from 1 to 16 km. The small source diameters were for the bursts with signal bandwidths of less than several hundred hertz, and the large source diameters were for the bursts with signal bandwidths of several kilohertz. If the radiation is coherent, the correlation is not directly related to the source region size.

The results of the calculations for the source size of the individual bursts are based upon the following assumptions: (1) The radiation is incoherent. (2) The AKR source region is circularly symmetric with a Gaussian brightness distribution.

The results of the calculations for the source size of individual AKR bursts are: (1) The apparent source diameter of individual AKR bursts ranges from 1.4 to 15.4 km. (2) The average source diameter of the individual bursts is 9.3 km. (3) AKR bursts that have bandwidths of less than several hundred Hz have source diameters of less than 5.0 km; AKR bursts with bandwidths near 1 kHz

have source diameters of approximately 10.0 km; and AKR bursts with bandwidths near 2 kHz have source diameters of approximately 15 km.

D. The Brightness Temperature

The brightness temperature was calculated for the long baseline events detected on February 20, 1979. From equation (30), the brightness temperature is proportional to the flux density measured at the spacecraft, divided by the square of the source region's angular size. Thus, the brightness temperature is proportional to the flux density at the radius of the source region. The spectral density of the AKR bursts, received by the spacecraft, was measured from the wideband receiver AGC levels and the signal amplitudes in the high resolution spectrograms. The actual spectral densities can be higher than the measured spectral densities, for bursts with bandwidths narrower than the 20 Hz spectrum analyzer resolution.

Brightness temperatures of the bursts were in the range of 5.95×10^{19} to 5.52×10^{23} °K. The brightness temperature was largest for the events with a high correlation and smallest for the events with a low correlation, except for the event at 0311:20 UT. This burst was the most intense of the long baseline events analyzed. The spectrogram for this event, shown in the bottom two panels of Figure 22, shows a large decrease in the background noise level during the burst. This decrease in the noise level on the spectrogram is a result of the wideband receiver gain decreasing, because the intensity of the burst is much larger than the background noise. For comparison, the

lower limits of the brightness temperature for Jovian decametric radiation are from 10^{16} to 10^{17} °K [Ratner, 1976]. Table 2 lists the brightness temperatures for each of the seven events analyzed.

E. Source Region Spectral Density

If the source region diameter is known, equation (C-18) can be used to compute the electric-field spectral density at the edge of the source region. The spectral density at the source is proportional to the square of the source-spacecraft distance divided by the square of the source region diameter. Table 2 lists the electric-field spectral density for the seven long baseline events analyzed. These results assume that the radiation is incoherent and that the source region is circularly symmetric. For source region diameters less than 5 km, the source region spectral density ranged from 9.07×10^{-4} to 1.25×10^{-2} $\text{V}^2 \text{m}^{-2} \text{Hz}^{-1}$. Since the bursts with source region diameters less than 5 km all had very narrow signal bandwidths, these values represent lower limits to the source region spectral density. For source region diameters between 5 and 10 km, the source region spectral density ranged between 3.00×10^{-5} to 1.06×10^{-4} $\text{V}^2 \text{m}^{-2} \text{Hz}^{-1}$. For source region diameters between 10 and 16 km, the source region spectral density ranged between 1.35×10^{-6} and 5.61×10^{-4} $\text{V}^2 \text{m}^{-2} \text{Hz}^{-1}$.

F. Source Region Amplification

If the spectral density of an AKR burst, measured at the spacecraft, is extrapolated back to the radius of the source region, the amplification within the source region can be computed. From

equation (C-20) the spectral density of the waves detected by the spacecraft is proportional to the square of the source region's angular size multiplied by the total growth, within the source region. For a constant spectral density at the spacecraft, the required amplification within the source region is larger for small angular source region sizes than for large angular source region sizes. Table 2 lists the source region amplification for each of the long baseline events. For source region diameters less than 5 km, the required source region amplification ranged from 124 dB to 155 dB (assuming that the ambient galactic background noise is 10^{-20} to 10^{-18} W m⁻² Hz⁻¹ [Alexander et al., 1970; Brown, 1973]); for source region diameters between 5 and 10 km, the required source region amplification ranged from 109 dB to 135 dB; and for source region diameters between 10 and 15 km, the required source region amplification ranged from 96 dB to 142 dB. The values for the source region amplification assume that the received signals are incoherent radiation from a spherically symmetric source region with a Gaussian brightness distribution.

G. Summary

The high correlations, measured for all of the events analyzed, indicate that the signals received by both spacecraft are nearly identical. The correlations were also found to be higher for the bursts with narrow bandwidths than for bursts with wider bandwidths. The correlation results are interpreted differently for coherent radiation than for incoherent radiation. If the radiation is assumed

to be incoherent, interferometry will measure the angular size of the source region. If the radiation is coherent, high correlations would be expected at all baselines, provided that both spacecraft are within the beamwidth of the coherent source.

If the radiation generated in the AKR source region is incoherent, the AKR source region diameter is in the range of 1 to 16 km, with a statistical source diameter of 9.27 km. The central brightness temperature is between 5.95×10^{19} and 5.52×10^{23} °K. The electric-field spectral density at the edge of the source region is between 1.35×10^{-6} and 1.25×10^{-2} V² m⁻² Hz⁻¹. The amplification within the source region is between 96 and 155 dB.

To determine if the radiation is coherent or incoherent, the results of the interferometry measurements must be compared with the properties of the AKR amplification region. Amplified waves, propagating in different directions, must have nearly identical spectral and phase characteristics. With source region diameters in the 1 to 16 km range, the wave growth per unit length, within the source region, will be high. To conclude that the radiation is incoherent, the wave growth within the source region must be consistent with the growth rates predicted by the theories, with the observed electron velocity distributions. Additionally, mechanisms, such as coherent scattering and wave reflection, must be investigated to determine if these mechanisms will produce high correlations for long baselines, with a large incoherent source region.

VI. INTERPRETATION OF THE RESULTS

A. Properties of Incoherent and Coherent Radiation

High correlations have been measured at projected baselines of up to 3868 km. To observe high correlations, the radiation detected by each spacecraft must have nearly identical spectral and phase characteristics. The correlation results are interpreted differently for coherent radiation than for incoherent radiation. If the radiation emitted from the source region is incoherent, the visibility of the source region is the Fourier transform of the brightness distribution. If the radiation emitted from the source region is coherent, an upper limit to the source region diameter can be inferred from the angular width of the radiation pattern. The correlation results and the spectral characteristics of AKR bursts can be used to help determine if the radiation is coherent or incoherent.

1. Incoherent Radiation

For incoherent radiation, the phase difference between the radiation emitted from different elements within the source region is random, as a function of time. If the radiation emitted from one element within the source region is cross-correlated with the radiation emitted from another element within the source region, the magnitude of the correlation will be zero. When the radiation emitted from

the entire source region is detected by different spacecraft, the phase differences between the signals received by each spacecraft will be a function of both time and frequency. With large source regions and long projected baselines, the phase differences between the signals received by each spacecraft will be large, and the correlation will be low. This definition of incoherent radiation is based upon the conditions necessary for interferometry to correctly measure the angular size of the source region.

2. Coherent Radiation

For coherent radiation, the phase difference between the radiation emitted from different elements within the source region is constant, as a function of time. If the radiation emitted from one element within the source region is cross-correlated with the radiation emitted from another element within the source region, the magnitude of the correlation can be any value between zero and one. With coherent radiation, the signals emitted from different elements within the source region will interfere, producing a complex radiation pattern. The radiation pattern from a coherent source region is dependent upon the exact phase differences between the radiation emitted from each element within the source region. Multi-lobed radiation patterns will have a 180° phase shift between lobes. Since the radiation pattern is a function of the wavelength, the correlation can be less than one, for coherent radiation with a non-zero bandwidth.

B. AKR Source Region Models

The theories, which explain the generation of AKR, must be consistent with the high correlations measured with interferometry. The properties of the AKR amplification region will be examined to determine if the conditions necessary to produce high correlations exist.

Two models of the source region have been proposed to explain the generation of AKR. A number of theories assume that the galactic background radiation is amplified by the Doppler-shifted cyclotron resonance mechanism, as the radiation propagates through the AKR source region [Melrose, 1976; Wu and Lee, 1979; Omid and Gurnett, 1982]. The details of the amplification process vary in each theory, but are consistent with amplification of frequencies slightly above the gyrofrequency in the source region. The second model assumes that the AKR source region is a natural radio laser [Calvert, 1982]. With the laser model, radiation is amplified on multiple passes through the source region and is emitted as a coherent beam.

1. The Amplifying Region

a. Assumptions

Each individual amplifying region is assumed to have the following characteristics: (1) For amplifying region sizes much greater than the wavelength of the radiation, all waves arriving at the angle Φ are amplified simultaneously and emitted at the same angle Φ . (2) For amplifying region sizes near the wavelength of the radiation,

diffraction effects determine the emission angle. (3) All waves emitted at the same angle are identical. (4) For amplifying region sizes much greater than the wavelength of the radiation, the angular size of the solid angle of amplified galactic background noise illuminating the spacecraft is equal to the angular size of the source region, as viewed from the spacecraft. (5) For amplifying region sizes near the wavelength of the radiation, the solid angle of amplified galactic background radiation illuminating the spacecraft is greater than the angular size of the source region, as viewed from the spacecraft. (6) The brightness distribution of the radiation emitted from the source region is uniform and has a diameter equal to the diameter of the amplifying region. (7) The amplification length in the amplifying region is comparable to the diameter of the amplifying region. Thus, the amplifying region can be treated as a spherical region with properties like a circular aperture.

The source region is assumed to (1) consist of one or more individual amplifying regions (with each individual amplifying region acting independently), (2) have a Gaussian brightness distribution for an array of individual amplifying regions, and (3) have an amplification length comparable to the diameter of the source region.

The galactic background noise from each element of solid angle is assumed to be incoherent and have a uniform brightness distribution. The correlation will be assumed to be proportional to the overlap of the solid angles of amplified background radiation illuminating each spacecraft. Figure 28 shows the geometry of the amplifier model

and defines the angular size of the satellite baseline, the amplifying region, and the galactic background radiation illumination cone.

b. Calculation of the Correlation

The correlation of the signals received by two spacecraft can be estimated by determining the amount the solid angles of amplified galactic background radiation illuminating each spacecraft overlap. The galactic background noise, originating in the overlapping solid angles, will be detected by both spacecraft identically and will have a 100 percent correlation. The galactic background noise, originating in the areas that do not overlap, will be detected by only one spacecraft and will not be correlated. The correlation of the total signal detected by one spacecraft with the total signal detected by the other spacecraft can be estimated by examining the signal-to-noise correction term in equation (23), with the assumption that

$$S_1^2 = S_2^2 = dA \quad (32)$$

and

$$V_1^2 = V_2^2 = A \quad , \quad (33)$$

where A is the solid angle of amplified galactic background radiation illuminating each spacecraft, and dA is the solid angle of overlap.

Substituting equations (32) and (33) into the signal-to-noise term in equation (23) gives the estimated correlation as:

$$\rho = \left[\left\langle \frac{dA}{A} \right\rangle \cdot \left\langle \frac{dA}{A} \right\rangle \right]^{1/2} = \frac{dA}{A} \quad . \quad (34)$$

The ratio of the overlap dA of two circular disks of the same radius to the area A of one disk (the model correlation ρ) can be shown to be:

$$\frac{dA}{A} = \rho = \frac{2}{\pi} \{ \sin^{-1}[\sqrt{1 - (\beta/\Omega)^2}] - \beta/\Omega[\sqrt{1 - (\beta/\Omega)^2}] \} \quad , \quad (35)$$

where β is the separation of the disks (the angular separation of the spacecraft), and Ω is the diameter of the disks (angular size of the solid angle of amplified galactic background radiation illuminating the spacecraft). Figure 29 is a plot of the correlation, as a function of the ratio of the angular spacecraft separation to the angular size of the illumination cone, for the amplifying region model [equation (35)].

c. Calculation of Diffraction Effects

If the size of the amplifying region becomes comparable to the wavelength of the radiation, diffraction effects can become important. Diffraction effects can increase the size of the solid angle of amplified galactic background radiation illuminating each spacecraft. To

estimate the diffraction effects, the amplifying region is modeled as a circular aperture.

The normalized intensity $I(\Phi)$ of the diffraction pattern for a circular aperture is [Hecht and Zajac, 1974]:

$$I(\Phi) = \left[\frac{2J_1(\pi d \sin \Phi)}{\pi d \sin \Phi} \right]^2, \quad (36)$$

where d is the diameter of the aperture (diameter of amplifying region) in wavelengths, Φ is the angular position from the axis of the aperture, and J_1 is the Bessel function (of the first kind) of order one. By setting $I(\Phi)$ in equation (36) equal to $1/e$, the angular width Ω of the diffraction pattern, as a function of aperture diameter d (in wavelengths), can be shown to be:

$$\Omega = 2 \sin^{-1} \left(\frac{1.915}{\pi d} \right). \quad (37)$$

Table 3 gives the amplifying region diameters (aperture diameter) for different illumination cone sizes (angular diffraction pattern width). For diffraction effects to be important, the diameter of the amplifying region must be less than about 25 km.

d. Predicted Correlation for a Single Amplifying Region Source

For a fixed angular spacecraft separation β , there are two ways to have a large correlation predicted with a single amplifying region.

The amplifying region must either be extremely large or extremely small.

For large amplifying regions the illumination cone angular size Ω is equal to the angular size of the amplifying region α , as viewed from the spacecraft; thus the ratio β/Ω can be made as small as desired by making the angular size of the amplifying region large. Equation (35) gives the correlation, as a function of (β/Ω) , for the single amplifying region model. Table 4 lists the source size (d_1) predicted with a large amplifying region (at the approximate baselines and frequency for the events analyzed), for correlations between 50 and 95 percent. All of the source sizes predicted are greater than 1 R_E and cannot be physically justified, since they are substantially larger than the whole auroral region, and physically the single amplifying region model breaks down for sizes that are much larger than the wavelength of the emission.

For a small amplification region size, the illumination cone angular size Ω is equal to the angular size of the diffraction pattern. By making the amplifier diameter very small, Ω can be made as large as necessary to get the desired correlation. The correlation ρ , as a function of amplifying region diameter d (in wavelengths) and spacecraft separation angle β , can be determined for a very small amplifying region by substituting equation (37) into equation (35). Table 4 lists the source sizes (d_2) predicted with a very small amplifying region, for correlations between 50 and 95 percent. For both

baselines, the predicted source sizes are less than 16 km for all correlations above 60 percent.

e. Predicted Correlation for a Source Consisting of Multiple Amplifying Regions

For multiple independent amplifying regions, the correlation is dependent upon both the source region brightness distribution and the individual amplifying region size. To estimate the correlation of an array of independent individual amplifying regions, with a brightness distribution $S(x,y)$, the response of the interferometer to one small amplifying region is integrated over the brightness distribution. From equation (35), the response of the interferometer to one small independent amplifying region at angular position (x,y) , with brightness $S(x,y)$ is:

$$d^2\rho = S(x,y) \frac{2}{\pi} \{ \sin^{-1}[\sqrt{1 - (\beta/\Omega)^2}] - \beta/\Omega[\sqrt{1 - (\beta/\Omega)^2}] \} dx dy \quad . \quad (38)$$

Integrating equation (38) over the entire source region gives the correlation ρ for a source consisting of multiple amplifying regions. For a source region with a Gaussian brightness distribution, the correlation for multiple amplifying regions is:

$$\rho = \frac{2}{\pi} \{ \sin^{-1}[\sqrt{1 - (\beta/\Omega)^2}] - \beta/\Omega[\sqrt{1 - (\beta/\Omega)^2}] \} e^{-(\pi ab/2)^2} \quad , \quad (39)$$

where b is the baseline in wavelengths and α is the angular width (between $1/e$ points of the brightness distribution) of the source region.

For multiple amplifying regions, both the amplifying region size and the source region size can be adjusted to change the correlation. From equation (39), the size of the individual amplifying regions and the source region must be small for high correlations. For extremely small amplifying regions, a source consisting of multiple independent amplifying regions is an incoherent source (interferometry will measure the true source size). Table 5 lists the source sizes predicted by the multiple amplifying region model (at the approximate baselines and frequency for the events analyzed), for correlations between 50 and 95 percent. For all correlations above 70 percent, the predicted source sizes are less than 26 km.

f. Summary

To be consistent with the measured correlations, both amplifying region models require source sizes and amplification lengths of 2 to 25 km.

2. AKR Laser Feedback Model

Calvert [1982] proposed a model of the AKR source region in which part of the amplified wave is reflected back to its origin with the appropriate amplitude, phase, and direction to replenish itself. The ARK feedback model [Calvert 1982] visualizes the AKR source as a natural radio laser. The boundary of density enhancements,

approximately 100 km across, with an order of magnitude increase in density [Benson and Calvert, 1979], within the auroral plasma cavity, are presumed to partially reflect the waves, producing a closed feedback path within the source region. The laser feedback model of the AKR source region predicts: (1) the emission of very narrow band spatially coherent radiation, (2) no phase shift in the electric field across the beam, and (3) a Gaussian brightness distribution (with the brightness distribution diameter dependent upon the length of the laser) [Calvert, personal communication, 1985].

a. Brightness Distribution Diameter

An interferometer will measure a perfect correlation ($\rho = 1$) with spatially coherent radiation from a laser, independent of the size of the brightness distribution (provided that both spacecraft are within the beam). The intensity of a coherent beam of radiation, as a function of angular position, can be computed by taking the Fourier transform of the brightness distribution [Hecht and Zajac, 1974]. For a Gaussian brightness distribution, the normalized intensity $I(\Phi)$, and brightness distribution diameter d (in wavelengths), is:

$$I(\Phi) = e^{-(\pi d \sin \Phi)^2}, \quad (40)$$

where Φ is the angular position from the axis of the laser. By setting $I(\Phi)$ in equation (40) equal to $1/e$, the angular width θ of the

coherent beam, as a function of the brightness distribution diameter d (in wavelengths), is:

$$\theta = 2 \sin^{-1} \left(\frac{1}{\pi d} \right) \quad . \quad (41)$$

Figure 30 is a plot of the angular diameter θ of a coherent beam, as a function of source region diameter, for a Gaussian brightness distribution [equation (41)]. For diameters much larger than 15 or 20 km (at a frequency of 250 kHz), the beam diameter is small enough (less than 2°) that the probability that only one spacecraft will be in the beam will begin to become large. The spectra of the AKR events observed at the long baselines are almost identical for both spacecraft. A close comparison of the spectra from each spacecraft, shown in Figures 21 and 22, reveals some small differences. The similarity of the spectra indicates that the angular width of the beam, for the laser feedback model, is at least 2.5° .

b. Summary

The AKR laser feedback model will give high correlations at all baselines, when both spacecraft are within the beam. For an angular beam width of 2.5° , the diameter of the brightness distribution must be smaller than 20 km.

C. Source Region Amplification

The flux density of the signals detected by the spacecraft is [equation (C-20)]:

$$s = \frac{1}{4} \alpha^2 s_g \times e^{d\gamma} \quad , \quad (42)$$

where α is the angular width of the source region, s_g is the flux density of the galactic background noise, d is the amplification length within the source region, and γ is the growth rate. Substituting equation (C-7) into equation (42) and solving for the total growth, $d\gamma$, gives:

$$d\gamma = \ln \left(4 \frac{R^2}{d^2} \frac{s}{s_g} \right) \quad , \quad (43)$$

and solving for the growth rate, γ , gives:

$$\gamma = \frac{1}{d} \ln \left(4 \frac{R^2}{d^2} \frac{s}{s_g} \right) \quad . \quad (44)$$

Figure 31 is a plot of the total wave growth, as a function of source region diameter. For a constant flux density received at the spacecraft, an order of magnitude decrease in the source region diameter requires an increase in the total wave growth by 20 dB. From equation

(C-18), the received flux density is proportional to the square of the source region diameter. Thus, smaller source region diameters will require a larger total wave growth. Figure 31 assumes that the flux density of the galactic background noise is $10^{-19} \text{ W m}^{-2} \text{ Hz}^{-1}$ and the flux density of the signals received by the spacecraft, located at a radial distance of $12 R_E$, is $10^{-15} \text{ W m}^{-2} \text{ Hz}^{-2}$.

Figure 32 is a plot of the average growth rate, as a function of source region diameter. The required growth rate rises very quickly for source region diameters smaller than 10 km. This rapid increase in the growth rate is caused by two factors: (1) The required total wave growth is larger for small source region diameters. (2) The total wave growth must be accomplished over a smaller length. Equation (44) and Figure 31 assume that the growth rate is constant within the source region and zero outside.

Omidi and Gurnett [1984] used typical electron distribution functions, measured by the S3-3 spacecraft, to calculate the path-integrated growth of AKR. Substantial wave growth was found only for ray paths with wave-normal angles which remained close to 80° for a considerable length of time. The wave growth, computed with the electron distribution functions measured by S3-3, was substantially less than what is required to explain the observed intensity of AKR. Omidi and Gurnett [1984] also calculated the path-integrated growth of AKR for electron distribution functions having much steeper velocity space gradients. With reasonable velocity space gradients, Omidi and

Gurnett [1984] found that the galactic background noise could be sufficiently amplified with an amplification length of 70 km.

Calvert [1982] has proposed wave amplification, with feedback, to explain the observed intensity and discrete structure of AKR bursts. Since a portion of the wave is reflected, and propagates through the amplification region more than once, the laser feedback model requires less gain to explain the observed AKR intensity. Calvert [1982] estimates that approximately 40 dB of gain per loop is required with the laser feedback model. Omid and Gurnett [1984] point out that during some portions of the feedback loop, the waves will resonate with the downgoing electrons and will most probably be damped. The amplification along the upgoing portion of the loop will have to compensate for this damping. Although the gain required for the laser feedback model is less, Omid and Gurnett [1984] show that gradients in the electron distribution function, steeper than what are observed, are also necessary with the laser feedback model.

D. Ray-Tracing Results

A ray-tracing analysis was performed to determine if wave reflection from a convex surface, such as the plasmopause, could produce a small source region image and high correlations. A complete description of the ray-tracing analysis can be found in Appendix C.

From an analysis of the propagation time difference, for waves propagating directly to both spacecraft, the source region diameters are from 2 percent to 24 percent smaller than the source diameters

computed with an assumed source region location along a 70° Mlat field line located at 21.0 hrs MLT. The source region diameters, with the waves reflecting from the plasmopause, are from 5 percent to 34 percent larger than the source diameters computed with an assumed source region location along a 70° Mlat field line located at 21.0 hrs MLT with the waves propagating directly to the spacecraft. These adjustments to the source region diameter do not affect the results significantly.

The most significant result of the ray-tracing analysis is that the flux density of waves reflecting from the plasmopause can be 18 to 121 times greater than the flux density of waves propagating directly to the spacecraft. From equation (C-21), the flux density of the radiation, detected by the spacecraft, is proportional to the solid angle of amplified galactic background noise illuminating the spacecraft. When the waves reflect from a convex surface, such as the plasmopause, a much larger solid angle of amplified galactic background noise will illuminate the spacecraft. Since the flux density of the waves reflecting from the plasmopause is much greater than the flux density of the waves propagating directly to the spacecraft, the waves propagating directly to the spacecraft will have only a small effect on the measured correlation.

E. Point Scattering of the Waves

When plane waves scatter from a spherical scattering center, the total electric and magnetic fields, outside of the scattering

center, are composed of two components: (1) the fields from the incident wave, and (2) the fields from the scattered wave. Scattering of incoherent radiation from a single scattering center can produce high correlations only if the ratio of scattered radiation to incident radiation, detected by each spacecraft, is high.

For a scattering center that is larger than the wavelength of the radiation, the cross section of the scattering center is twice its geometric area [Born and Wolf, 1965]. For scattering centers smaller than the wavelength of the radiation, the total scattering cross section is [Jackson, 1962]:

$$\sigma = \frac{10\pi}{3} a^2 (ka)^4, \quad (45)$$

where a is the radius of the spherical scattering center and k is the wave number. Since the intensity of radiation scattered from a single scattering center is much less than the intensity of the radiation propagating directly from the source region, the scattered radiation would have only a very small effect on the measured correlation.

Under certain circumstances, incoherent radiation scattered from multiple point scattering centers could produce a high correlation. If the scattering region consists of uniformly spaced point scattering centers of an identical size, a diffraction pattern can be produced. With randomly distributed scattering centers, no coherent phase relationship between the waves scattered by the individual

scattering centers will exist, and correlation will be low. It seems very unlikely that a scattering region in the magnetosphere would consist of uniformly spaced scattering centers of an identical size.

F. Properties of the Correlation

1. Correlation Dependence on Signal Bandwidth

The correlation of AKR bursts with a narrow signal bandwidth was found to be larger than the correlation of AKR bursts with a wide signal bandwidth. There can be several causes for this effect: (1) AKR bursts with a wider signal bandwidth are generated in a larger source region. (2) Propagation effects could alter the phase, as a function of frequency, of the signals detected by each spacecraft. (3) If the radiation is coherent, the amplitude and phase differences, between the signals received by each spacecraft, are a function of the radiation pattern. Since the radiation pattern is a function of frequency, the amplitude and phase differences between the received signals would be larger for wide bandwidth signals than for narrow bandwidth signals.

Although the correlation decreases more rapidly, as a function of delay, for wide bandwidth signals, an incorrect signal delay cannot explain the observations. From equation (6), the maximum error in the signal delay ($\pm 3.5 \mu\text{sec}$) will reduce the correlation by less than 0.1 percent for a 2 kHz signal bandwidth. The observed decrease in the correlation is approximately 50 percent for a 2 kHz signal bandwidth.

a. Source Region Size is a Function of Signal Bandwidth

Since AKR bursts are generated slightly above the gyrofrequency, different frequencies are generated at slightly different radial distances. For the earth's magnetic field, the gyrofrequency, in kilohertz, along a magnetic-field line is:

$$f_g = 8.1031 \times 10^2 [4 - 3r \cos^2 \lambda_m]^{1/2} r^{-3}, \quad (46)$$

where λ_m is the magnetic latitude of the field line, and r is the radial distance in R_E . From equation (46), at an emission frequency of 250 kHz and a source region located along a 70° Mlat field line, a 2 kHz bandwidth corresponds to a source region extending 29.87 km in radial distance. A 100 Hz signal bandwidth corresponds to a source region extending 1.49 km in radial distance. These source region thicknesses, as a function of signal bandwidth, are comparable to the source region diameters computed from the measured correlations.

b. Propagation Effects

To measure a high correlation, the phase difference between the signals received by each spacecraft must be constant, as a function of both frequency and time. If the waves are refracted or reflected between the source region and the spacecraft, the phase differences between the received signals will not be constant, and the correlation will be reduced. From equations (C-3) and (C-4), the index of refraction is a function of frequency, and from equation (C-1) the R-X mode

cutoff is also a function of frequency. Since the waves must propagate along slightly different paths to reach the different spacecraft, differences in the index of refraction along the different paths can cause phase differences between the received signals, as a function of frequency. Ray-tracing results [Omidi and Gurnett, 1984] have shown that there can be significant refraction within the source region. Density enhancements between the source region and the spacecraft can also cause phase differences between the received signals. If the waves reflect from the plasmopause, the different frequencies contained within the burst will reflect from slightly different locations on the plasmopause. Since the waves must propagate along different paths to reach the different spacecraft, the phase difference, as a function of frequency, between the signals received by each spacecraft will not be constant, and the correlation will be reduced.

c. Radiation Pattern Effects for Coherent Radiation

The radiation pattern, for a source region emitting coherent radiation, is a function of the emission frequency. Equations (36) and (40) are the radiation patterns for source regions with a uniform brightness distribution (a circular disk), and with a Gaussian brightness distribution. Both equations contain a term equal to $\pi d \sin \Phi$, where d is the diameter of the brightness distribution and Φ is the angular position from the axis of the brightness distribution. Unless both spacecraft were located symmetrically about the axis of the brightness distribution, the amplitude and phase of the received

signals, as a function of frequency, would be slightly different for each spacecraft. These amplitude and phase differences would be larger and the correlation lower for wide bandwidth signals.

2. Abrupt Correlation Phase Changes

Abrupt phase changes in the correlation can be produced by several effects: (1) If the radiation is coherent, radiation patterns with multiple lobes are possible. Since there is a 180° phase difference between lobes, spacecraft motion, an abrupt change in the frequency of the burst, or changes in the source region's brightness distribution could cause the radiation pattern to sweep past the spacecraft causing an abrupt phase shift in the correlation. (2) If the position of the source region changes, there will be an abrupt phase shift in the correlation. (3) Abrupt changes in emission frequency will introduce a phase shift in the correlation if the delay is incorrect. (4) Since the spacecraft are moving, the propagation path for the radiation detected by each spacecraft is continually changing. Since the phase of the signal received at each spacecraft is dependent upon the plasma parameters along the entire propagation path, spatial or temporal changes in density, along the propagation path, will cause a phase shift in the correlation.

G. Summary

1. Incoherent Radiation

If the radiation emitted from the source region is incoherent, the AKR source region diameter, calculated from the correlation

measurements, is from 1 to 16 km. For source region diameters in this range, diffraction effects produce partially coherent radiation, with nearly identical signals detected at each spacecraft. Amplification lengths, between 1 and 16 km, are much too short to explain the observed AKR intensity with the Doppler-shifted cyclotron resonance instability and simple wave amplification.

2. Coherent Radiation

a. Coherent Generation Mechanism

Any generation mechanism that produces coherent radiation will be able to explain the high correlations. The radiation pattern produced by coherent radiation is dependent upon the phase, amplitude, and the brightness distribution of the emitted signals. A spatially coherent source is analogous to an antenna array transmitting broadband noise [Dulk, 1970]. If the angular width of the radiation pattern lobes is assumed to be equal to the angular separation of the spacecraft, the source region diameter is less than 20 km. An amplification length of 20 km is too short to explain the observed AKR intensity with the Doppler-shifted cyclotron resonance instability and simple wave amplification.

If the angular width of the radiation pattern lobes is assumed to be narrower than the angular spacecraft separation, the source region diameter could be much larger than 20 km. With a large source region, the amplitude of the detected signals would vary over a large range of values. The amplitude of the detected signal is dependent

upon the spacecraft position within the radiation pattern. The ratio of the signal strength received by ISEE-1 to the signal strength received by ISEE-2 would vary widely, for individual bursts. Qualitatively, this variation in burst intensity ratios is not observed in the data. Inspection of the spectrograms shows that intense AKR bursts observed by ISEE-1 are also intense, when observed by ISEE-2. Weak AKR bursts observed by ISEE-1 are also weak, when observed by ISEE-2. No case has been identified that shows an intense AKR burst observed by one spacecraft, that is not observed by the other spacecraft. If the angular width of the radiation pattern was much smaller than the angular spacecraft separation, there would be more differences observed between the ISEE-1 and -2 spectrograms.

Refraction near the source region, or reflection from the plasmopause, of coherent radiation could spread the radiation over a wider solid angle. From equation (41), the angular width of the radiation pattern, for a Gaussian brightness distribution 83 wavelengths in diameter (100 km at an emission frequency of 250 kHz), is 0.44° . The maximum angular spacecraft separation, for the events analyzed, is 2.4° . Spreading the angular width of the radiation by a factor of 5.46 is consistent with the ray-tracing results, for waves reflecting from the plasmopause.

b. Laser Feedback Model

With the laser feedback model, the source region diameter, inferred from the measured correlations, is less than 20 km. From an

analysis of the spacing of multiple discrete frequency components, sometimes observed in AKR spectra, Calvert [1982] calculated the source region thickness to be approximately 25 wavelengths. The wave growth required for the laser feedback model is consistent with the growth rates predicted by Omid and Gurnett [1984], with the steepened electron distribution functions.

CONCLUSIONS

A. Results

With a source region emitting incoherent radiation, the correlation measurements give source region diameters from 1 to 16 km. A simple amplifying region model, which only amplifies the incoming radiation, can produce high correlations only if the source region diameter is smaller than 20 km. Small source region diameters are required for diffraction effects to produce partially coherent radiation. The wave growth, computed with steepened electron distribution functions and the Doppler-shifted cyclotron resonance instability, is not large enough to explain the observed AKR intensity, with source region diameters less than 20 km. This result strongly indicates that the radiation is coherent.

The correlation measurements are consistent with generation mechanisms that produce coherent radiation. The similarity of the ISEE-1 and -2 spectrograms indicates that the angular width of the radiation pattern is larger than 2.5° . Source region diameters of less than 20 km or refraction (reflection) of waves emitted from a larger coherent source region (~ 100 km) will produce a radiation pattern with an angular width of 2.5° . The wave growth, computed with steepened electron distribution functions and the Doppler-shifted cyclotron resonance instability, is large enough to explain the

observed AKR intensity, if amplification length is greater than 70 km or if the radiation is generated with the laser feedback model.

The radiation emitted from the AKR source region must be coherent over an angular width of at least 2.5° to explain the observed correlations. The generation mechanism for AKR must be able to produce coherent radiation, and have sufficient growth to explain the observed AKR intensity.

B. Areas for Further Investigation

Several aspects of this research deserve further study. First, much longer baselines could be achieved by simultaneous interferometry with three satellites, ISEE-1, ISEE-2, and Dynamics Explorer 1 (DE-1). Since DE-1 is in a polar orbit and the ISEE spacecraft are in equatorial orbits, very large spacecraft separations are possible. With three spacecraft, the exact source region location can be determined for individual bursts and data would be provided simultaneously at three projected baselines. With the the proper spacecraft locations, orthogonal components of the source diameter could be measured.

Second, the abrupt changes in the correlation phase can be produced by changes in the characteristics of the burst (such as a change in the emission frequency), source region motion, or by propagation effects. Explanation of these correlation phase shifts could provide information about the generation mechanism of AKR.

Third, measurement of the instantaneous radiation pattern for individual bursts would provide direct evidence of the source region

diameter, if the radiation is coherent. Comparison of the signal strengths, of the individual AKR bursts detected by two or more widely separated spacecraft, would provide a map of the radiation pattern.

Fourth, in addition to providing information about the spectral characteristics of an AKR burst, the correlation, as a function of signal delay can be used to identify reflected waves and waves propagating directly to the spacecraft. There should be two peaks in the correlation, as a function of delay, one for the waves propagating directly to the spacecraft, and one for the reflected waves.

Table 1
Slope of the Striations in Frequency-Time Correlograms,
for Different ISEE-1 Signal Delays

ISEE-1 Signal Delay (msec)	Slope (°)	Cotangent of Slope
6.0	163.00	-3.2709
5.5	161.50	-2.9887
5.0	160.00	-2.7475
4.5	158.00	-2.4751
4.0	155.50	-2.1943
3.5	152.50	-1.9210
3.0	148.50	-1.6319
2.5	144.00	-1.3764
2.0	138.00	-1.1106
1.5	130.00	-0.8391
1.0	120.00	-0.5774
0.5	107.00	-0.3057
0.0	92.50	-0.0437
-0.5	77.50	0.2217
-1.0	63.50	0.4986
-1.5	53.00	0.7536
-2.0	44.50	1.0176
-2.5	37.50	1.3032
-3.0	33.00	1.5399
-3.5	29.00	1.8040
-4.0	25.75	2.0732
-4.5	22.75	2.3847
-5.0	20.75	2.6395
-5.5	19.00	2.9042
-6.0	17.50	3.1716

Table 2
Correlation Results for Events at Long Baselines

Day	Time	Source- Baseline (Re)	Projected Baseline (km)	Correlation (%)	Source* Size (km)	E^2/Hz^\dagger	$T_b^\#$ (°K)	E^2/Hz°	Gain [•] (dB)
051	0038:15.0	10.738	3868.4	45	12.09	1.04×10^{-14}	5.95×10^{19}	1.35×10^{-6}	96-116
051	0041:21.5	10.798	3852.8	99	1.37	8.97×10^{-14}	4.00×10^{22}	9.07×10^{-4}	124-144
051	0051:30.0	10.994	3801.9	93	3.80	9.53×10^{-12}	5.52×10^{23}	1.25×10^{-2}	135-155
051	0307:42.0	13.438	3260.4	59	14.59	4.39×10^{-14}	2.67×10^{20}	6.06×10^{-6}	102-122
051	0308:10.0	13.438	3260.4	81	9.22	3.07×10^{-13}	4.68×10^{21}	1.06×10^{-4}	115-135
051	0308:32.0	13.454	3257.4	84	8.40	7.20×10^{-14}	1.32×10^{21}	3.00×10^{-5}	109-129
051	0311:20.0	13.487	3251.4	56	15.39	4.52×10^{-12}	2.47×10^{22}	5.61×10^{-4}	122-142

*Assumes an incoherent source with Gaussian brightness distribution.

[†]Peak spectral density measured at spacecraft ($\text{Volts}^2/\text{m}^2 \text{ Hz}$).

[#]Central brightness temperature.

[°]Peak spectral density extrapolated to radius of source region ($\text{Volts}^2/\text{m}^2 \text{ Hz}$).

[•]Assumes the ambient noise is 10^{-20} to $10^{-18} \text{ W/m}^2 \text{ Hz}$ [Brown, 1973].

Table 3

Amplifying Region Diameters for Different Illumination
Cone Sizes, Assuming Diffraction Effects

Ω (°)	d (wavelengths)	d (km)	α (deg $\times 10^{-3}$)
70.0	1.06	1.28	0.96
60.0	1.22	1.46	1.10
50.0	1.44	1.73	1.30
40.0	1.78	2.14	1.60
30.0	2.36	2.83	2.16
20.0	3.51	4.21	3.15
10.0	6.99	8.39	6.28
5.0	13.97	16.77	12.60
2.5	27.94	33.53	25.10

$R = 12.0 R_E$, $f = 250$ kHz.

Table 4
AKR Source Size Predicted by Single
Amplifying Region Model

B*	Correlation (%)	β/Ω	Ω (°)	d_1 (km) [†]	d_2 (km) [‡]
1	95	0.040	62.5	83488	1.47
1	90	0.080	31.3	41811	2.83
1	85	0.117	21.4	28586	4.11
1	80	0.157	16.0	21373	5.49
1	75	0.200	12.5	16698	7.02
1	70	0.240	10.4	13915	8.42
1	65	0.280	8.9	11927	9.81
1	60	0.320	7.8	10436	11.21
1	55	0.363	6.9	9191	12.73
1	50	0.403	6.2	8287	14.13
2	95	0.040	45.0	60111	2.00
2	90	0.080	22.5	30056	3.92
2	85	0.117	15.4	20571	5.70
2	80	0.157	11.5	15362	7.63
2	75	0.200	9.0	12022	9.74
2	70	0.240	7.5	10019	11.68
2	65	0.280	6.4	8587	13.62
2	60	0.320	5.6	7514	15.57
2	55	0.363	5.0	6618	17.68
2	50	0.403	4.5	5961	19.62

*Baseline parameters:

B = 1, b = 3340 km, $\beta = 2.5^\circ$, R = 12.0 R_E , f = 250 kHz.

B = 2, b = 2400 km, $\beta = 1.8^\circ$, R = 12.0 R_E , f = 250 kHz.

[†] d_1 is large amplifier solution.

[‡] d_2 is small amplifier solution.

Table 5
AKR Source Size Predicted by Multiple
Amplifying Region Model

B*	Correlation (%)	a(deg $\times 10^{-3}$)	d (km) [†]
1	95	5.26	7.03
1	90	7.54	10.07
1	85	9.36	12.51
1	80	10.97	14.66
1	75	12.46	16.64
1	70	13.87	18.53
1	65	15.25	20.37
1	60	16.60	22.18
1	55	17.96	24.00
1	50	19.34	25.83
2	95	7.32	9.78
2	90	10.49	14.02
2	85	13.03	17.41
2	80	15.27	20.40
2	75	17.34	23.16
2	70	19.31	25.79
2	65	21.22	28.34
2	60	23.10	30.86
2	55	24.99	33.39
2	50	26.91	35.95

*Baseline parameters:

B = 1, b = 3340 km, $\beta = 2.5^\circ$, R = 12.0 R_E, f = 250 kHz.

B = 2, b = 2400 km, $\beta = 1.8^\circ$, R = 12.0 R_E, f = 250 kHz.

[†]d is small amplifier solution.

Figure 1. The ISEE-1 plasma wave experiment block diagram (from Gurnett et al. [1978]), showing the narrow band sweep frequency receiver, the coarse resolution spectrum analyzer, the wave normal analyzer, the wideband receiver, the three electric dipole antennas, and the triaxial search coil magnetometer.

D-677-775-3

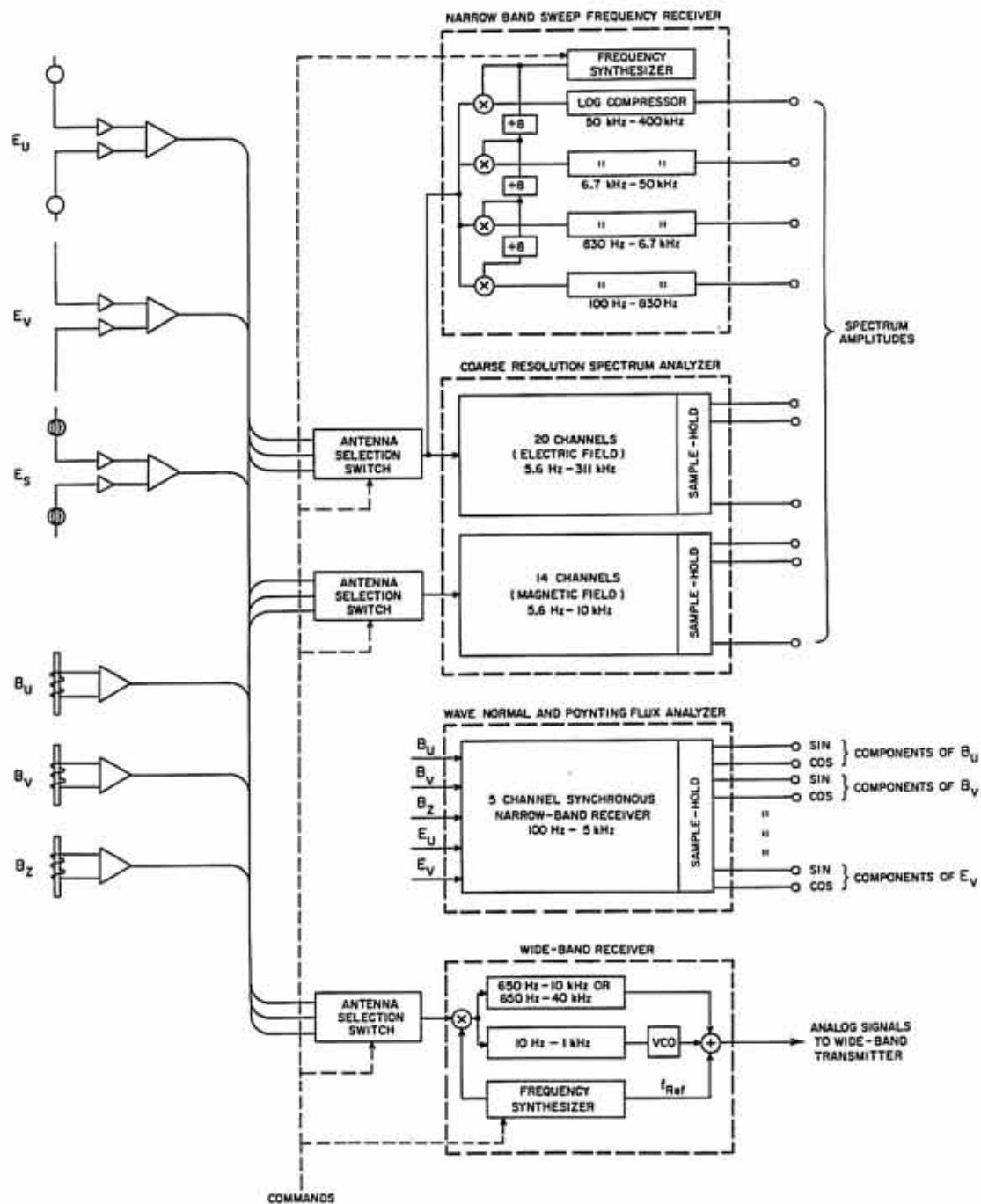


Figure 1

Figure 2. A diagram of the ISEE-1 spacecraft (from Gurnett et al. [1978]) showing the physical locations of the six electric field antennas and the triaxial search coil magnetometer.

C-677-783-1

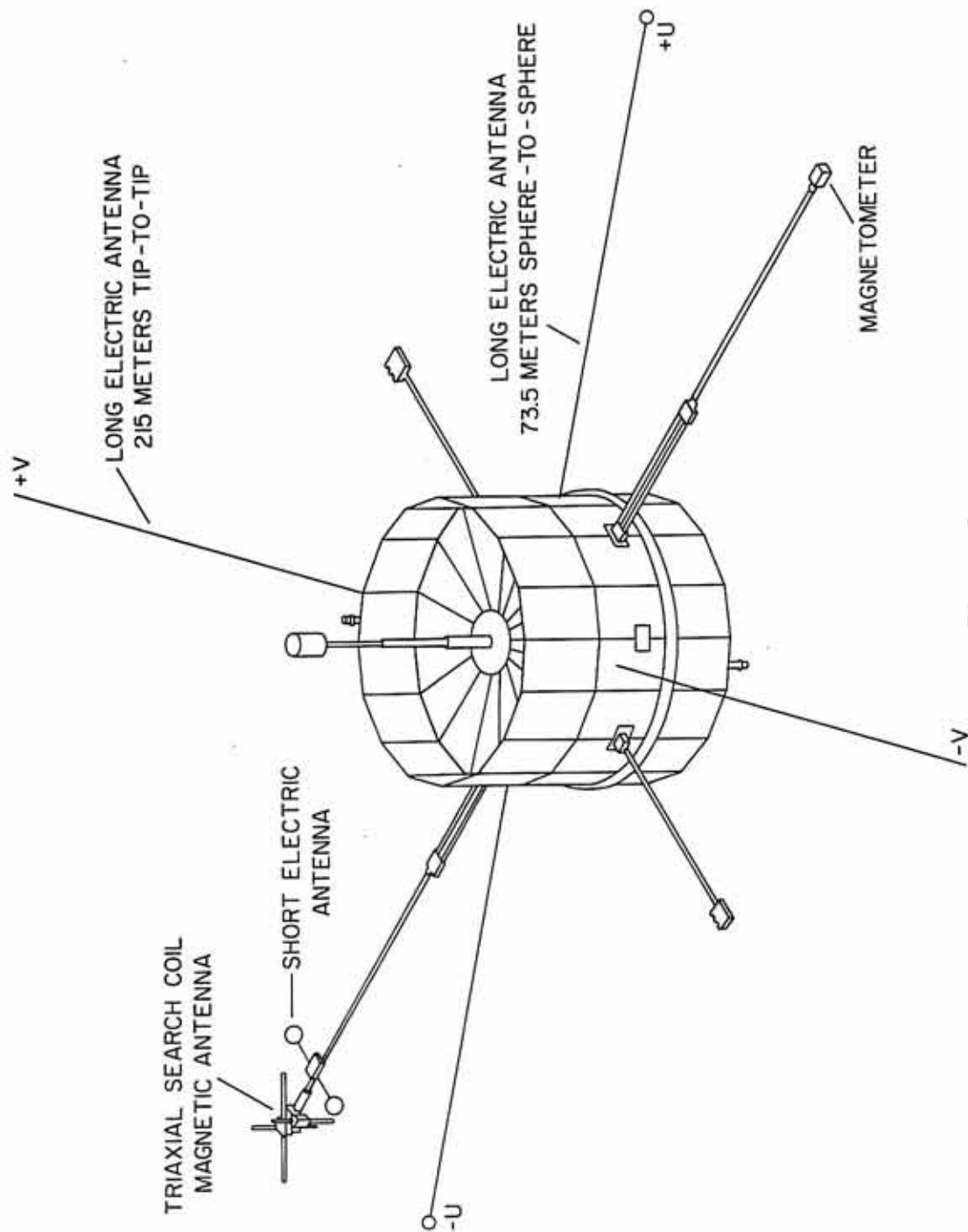


Figure 2

Figure 3. A block diagram of the ISEE-1 wideband receiver electronics (from Shawhan [1979]). The ISEE-2 wideband receiver is identical to the ISEE-1 wideband receiver, except that no 40 kHz bandwidth mode exists, and the reference frequency mixed with the received signal is 15.125 kHz instead of 62.5 kHz.

WIDEBAND/LBI RECEIVER

D-674-833

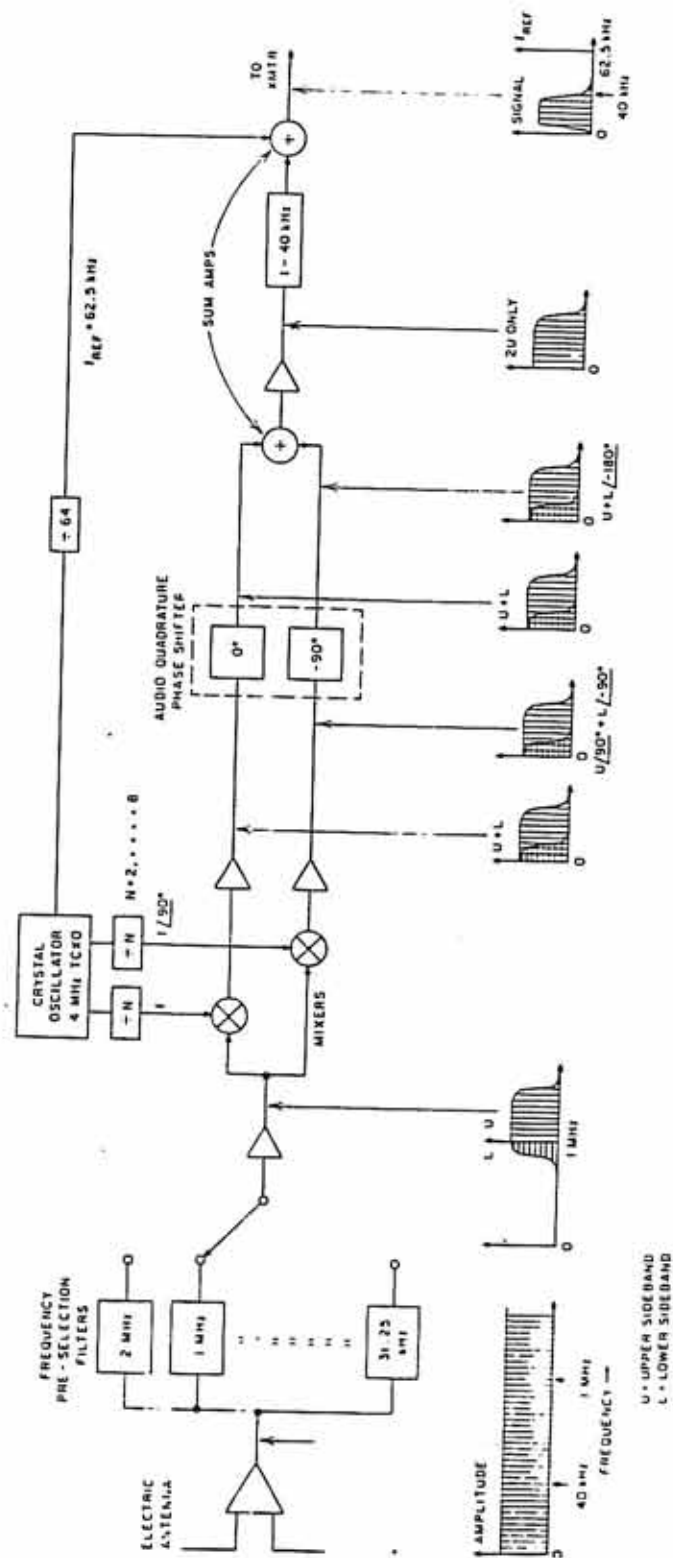


Figure 3

Figure 4. A block diagram of the ISEE-2 plasma wave experiment (from Gurnett et al. [1978]) showing the two electric dipole antennas, the coarse resolution spectrum analyzer, and wideband receiver.

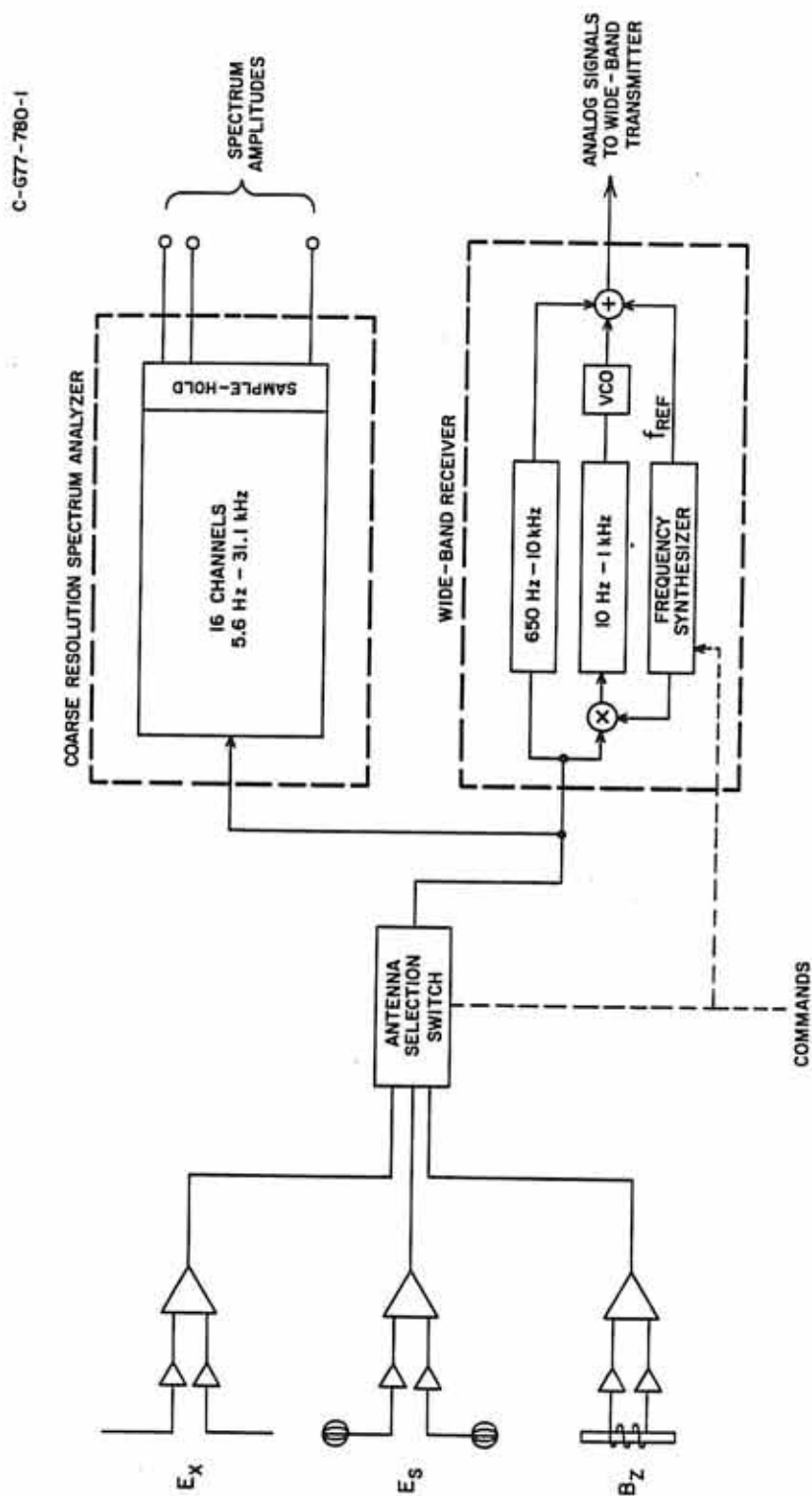


Figure 4

Figure 5. A diagram of the ISEE-2 spacecraft (from Gurnett et al. [1978]) showing the physical locations of the two electric field antennas and the search coil magnetometer.

C-077-784-1

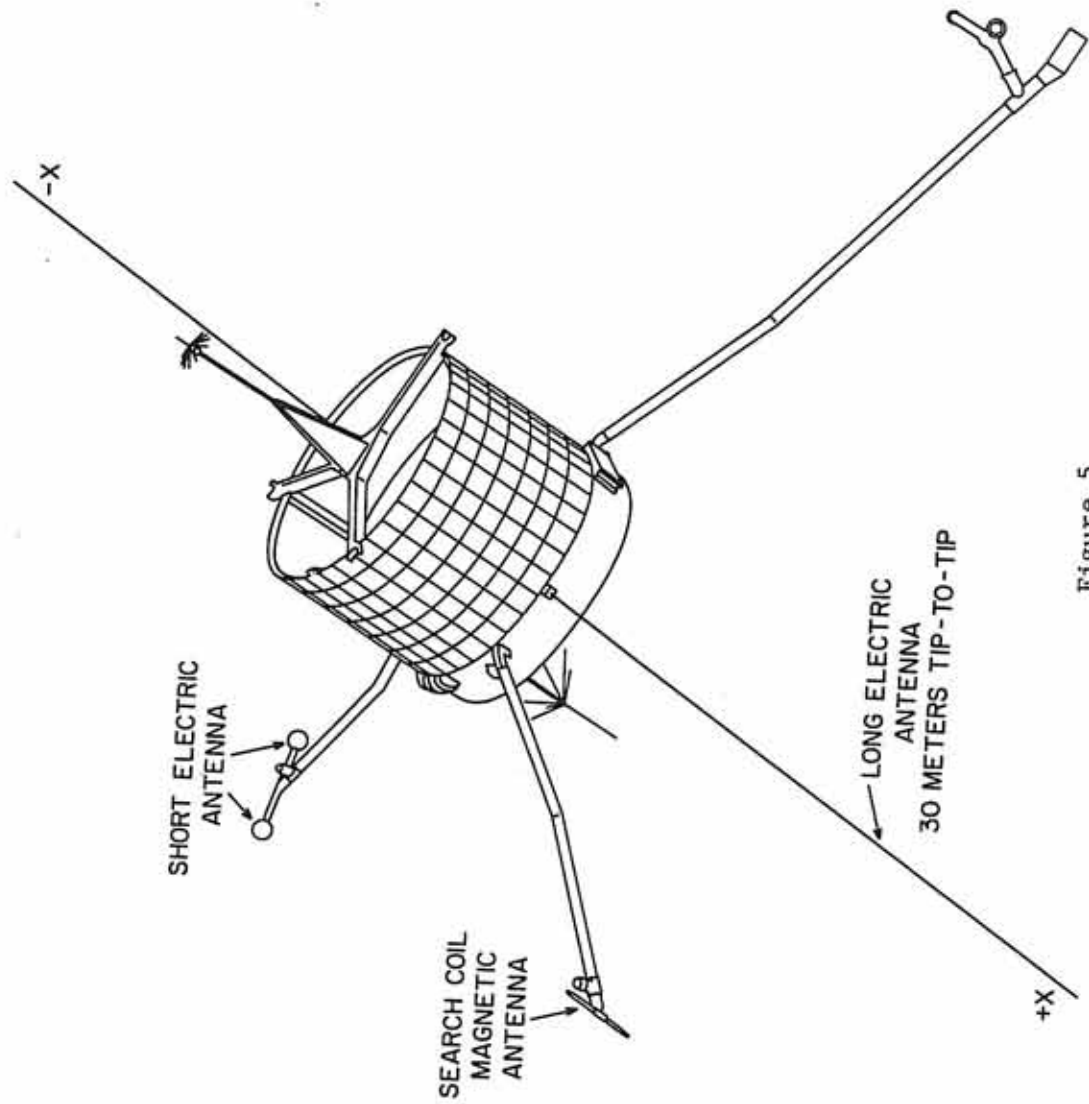
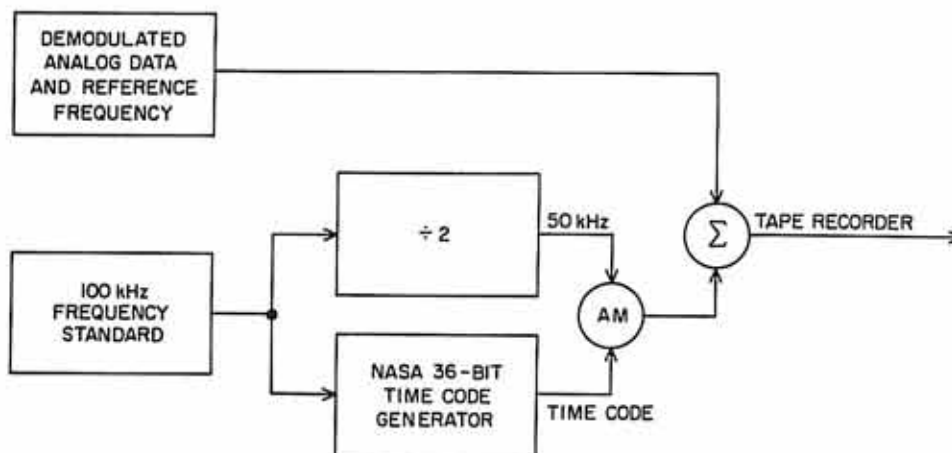


Figure 5

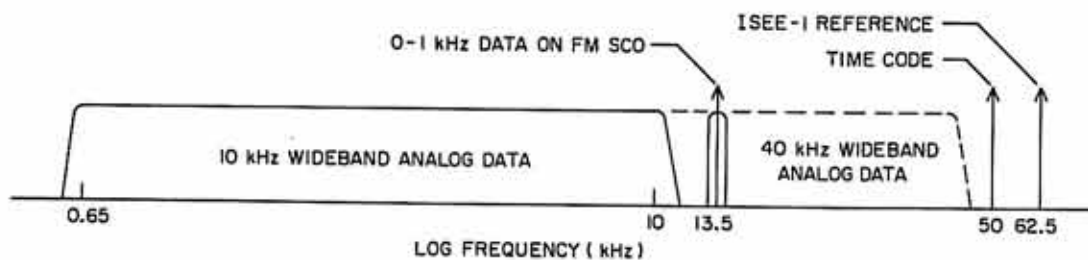
Figure 6. The ISEE interferometer tape recording scheme (from Shawhan [1979]). The analog data, frequency references, and time code information for one spacecraft are recorded on the same tape recorder track. The reference frequencies can be used to determine the exact local-oscillator frequency for each wideband receiver and the time code can be used for precise time alignment of the data.

C-684-370

ISEE GROUND RECORDING SCHEME



ISEE - I RECORDED SPECTRUM



ISEE - 2 RECORDED SPECTRUM

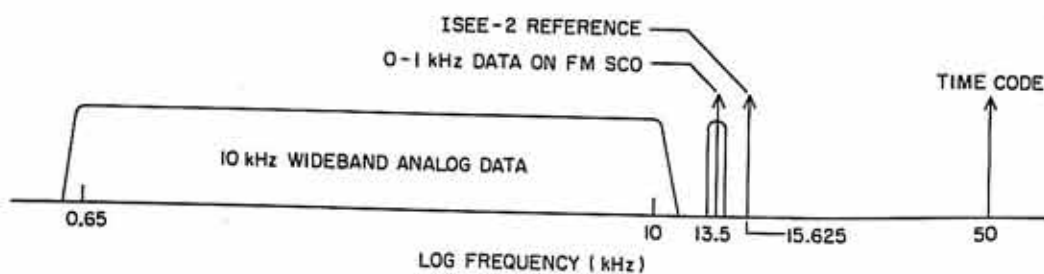


Figure 6

Figure 7. The ISEE interferometer analog tape processing scheme. The analog tape can be processed to produce three types of outputs. Strip chart recordings can be produced, giving the correlation fringe amplitude, the digital output from a Nicolet UA-500 A spectrum analyzer is interfaced to a computer for further analysis of the spectral characteristics, and 70 mm survey plots and correlograms can be produced over large time intervals. The one-bit digitized data can also be computer processed to produce delay-time correlograms.

ANALOG TAPE PROCESSING SCHEME

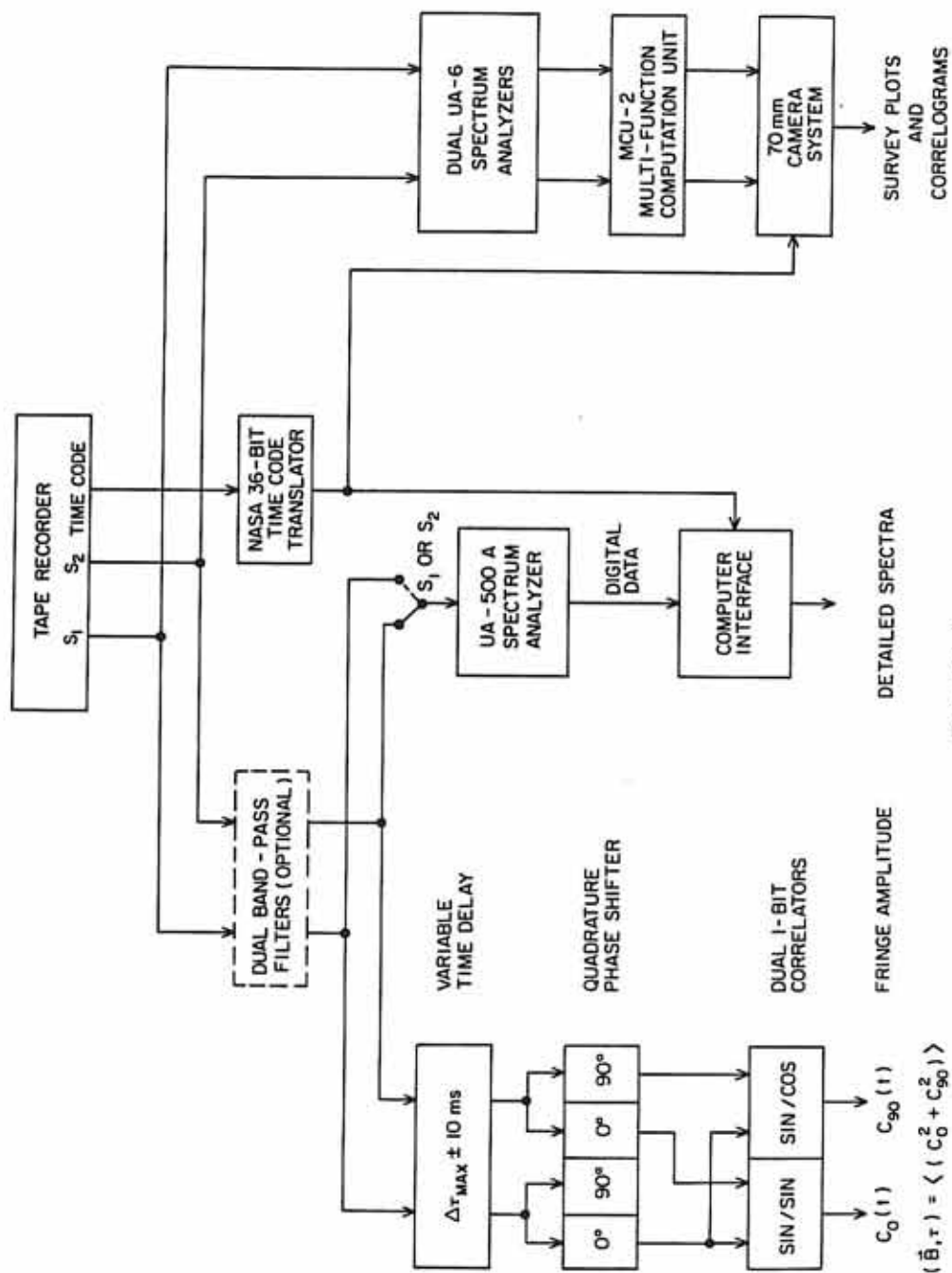


Figure 7

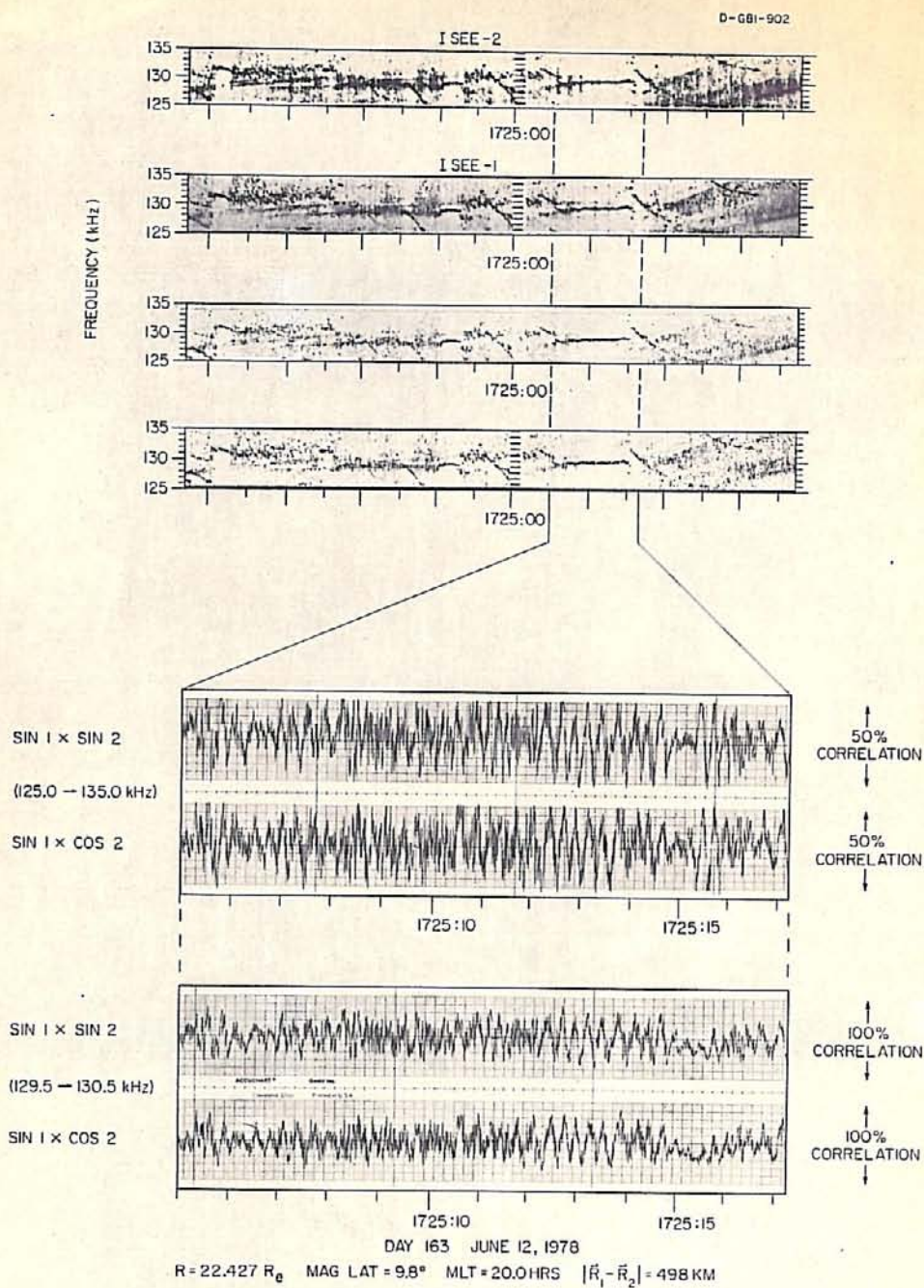


Figure 8

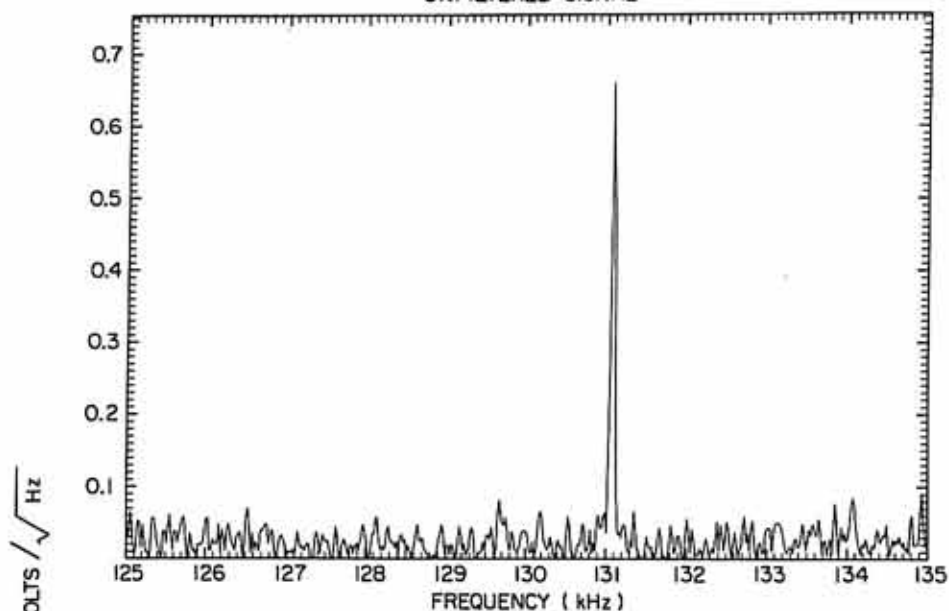
Figure 9. The top panel shows the detailed spectrum of an AKR burst over the full 10 kHz bandwidth. This burst has an extremely narrow signal bandwidth. The background noise levels can be measured and filtered before performing the correlation. The bottom panel shows the spectrum of the bandpass filtered signal, with the background noise removed.

D-G85-932

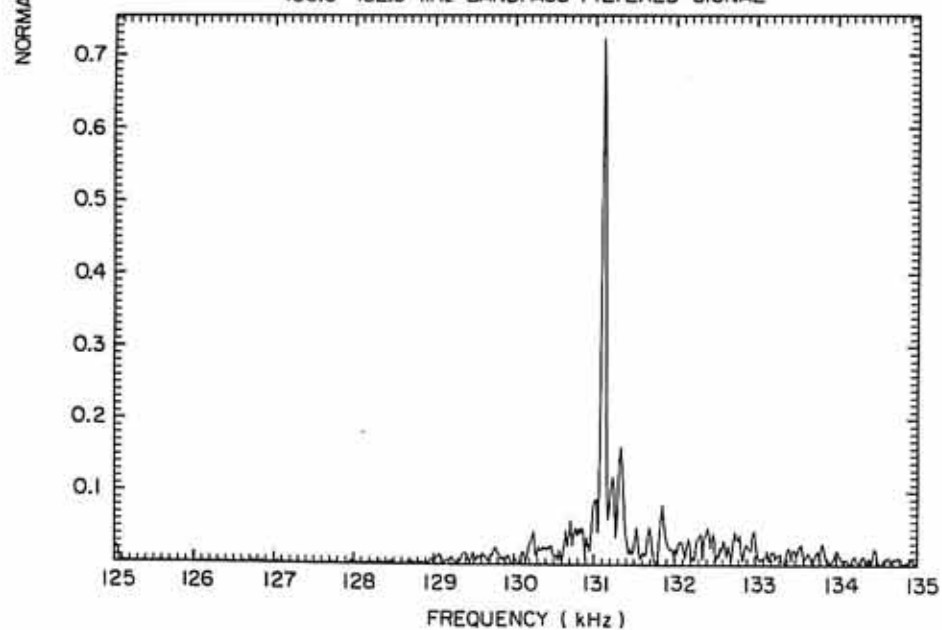
ISEE - I

FEBRUARY 27, 1978 DAY 058 1322:13.9 UT

UNFILTERED SIGNAL



130.0-132.5 kHz BANDPASS FILTERED SIGNAL

 $R = 22.6 R_E$

MAG LAT = 16.3°

LT = 2.38 HRS

Figure 9

Figure 10. This figure is a delay-time correlogram for white-noise test signals with a 10 kHz bandwidth. The correlation is plotted as a function of time for different signal delays. The slope of the striations is a function of the center frequency of the signals and the local-oscillator frequency difference. The rate of decrease in the correlation is determined by the bandwidth of the signal.

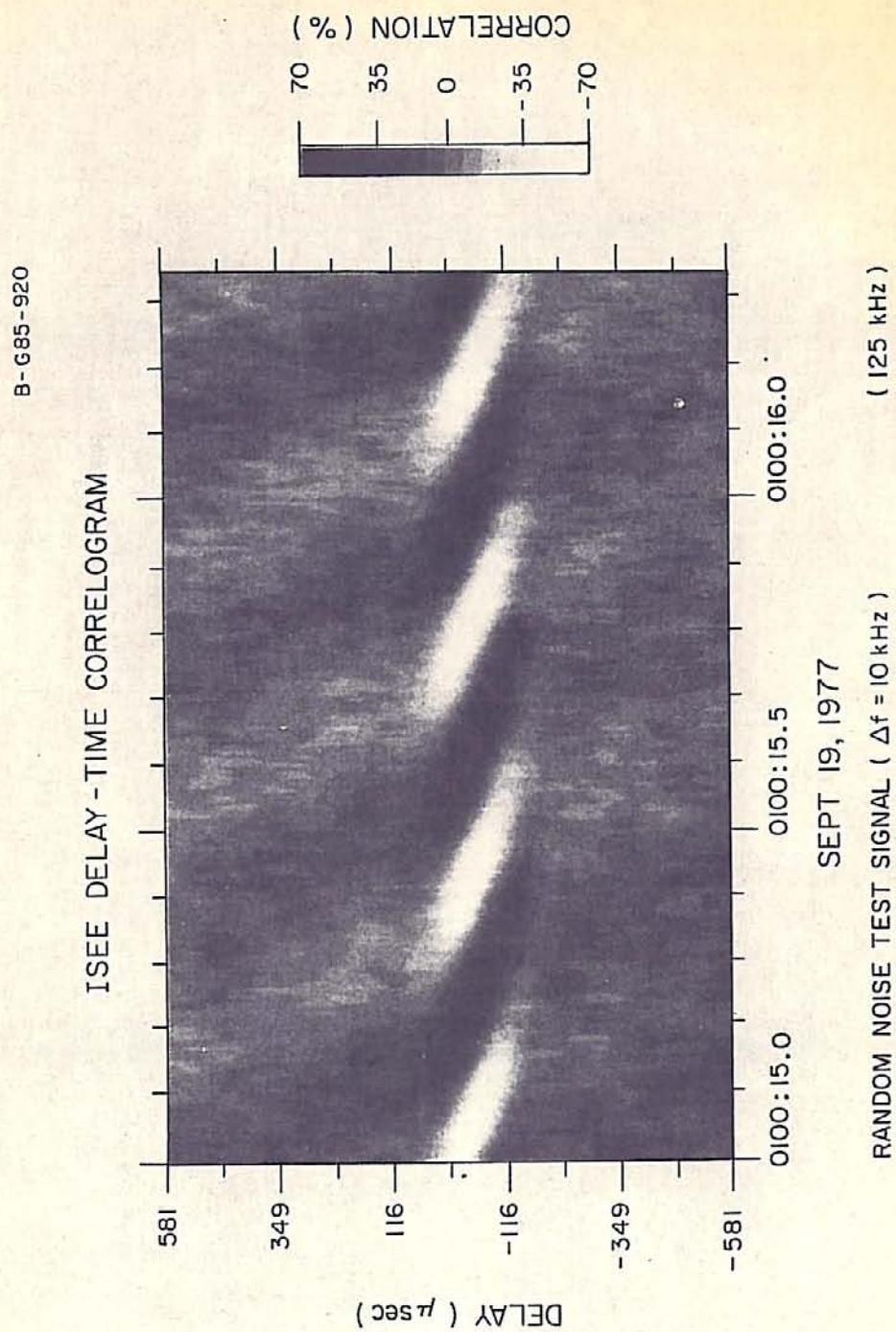


Figure 10

Figure 11. This figure shows the correlation, for different signal delays and bandwidths, of a signal with a white-noise power spectral density. The wider the bandwidth, the faster the correlation decreases.

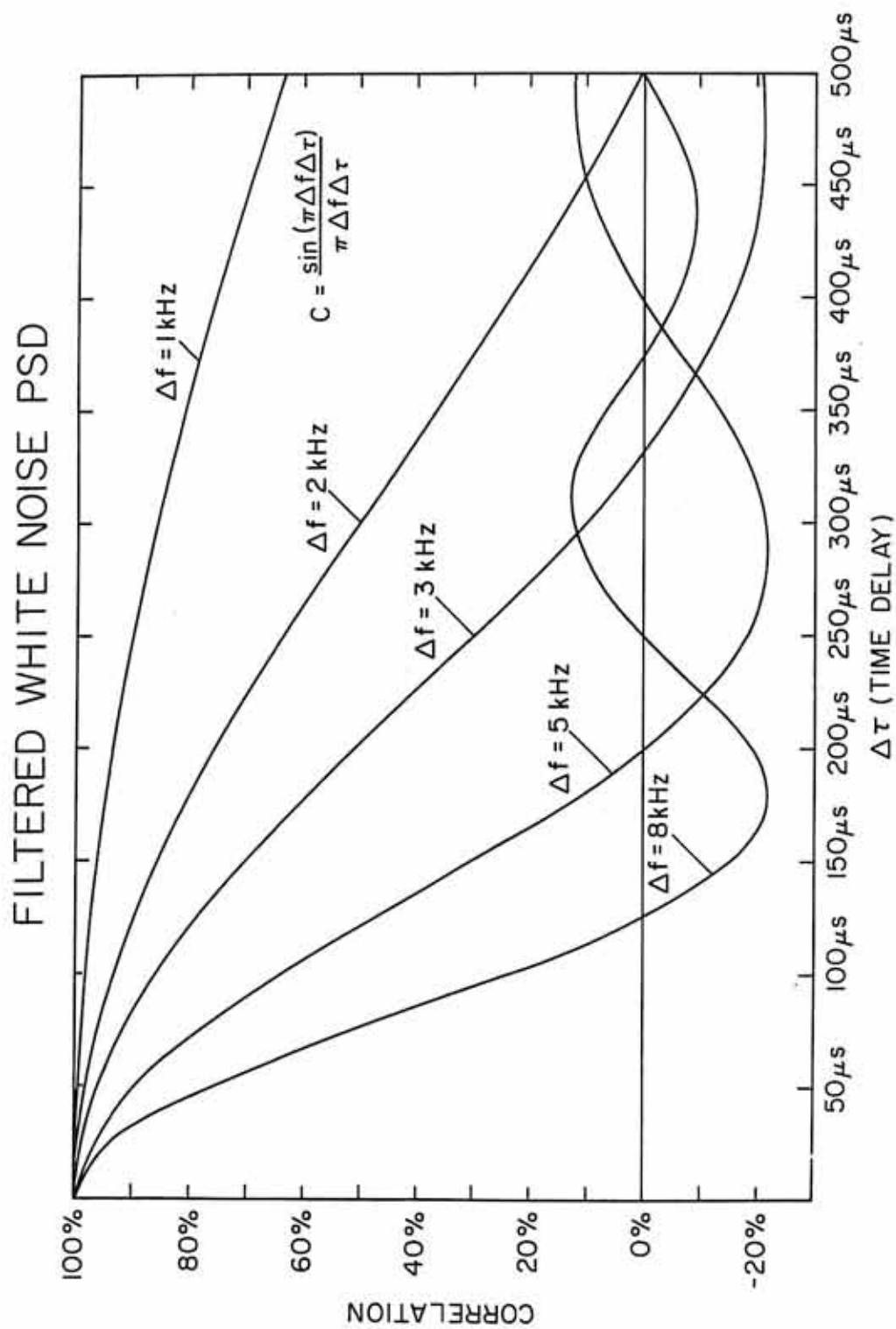


Figure 11

Figure 12. This figure shows the correlation, for different signal delays and bandwidths, of a signal with a Gaussian power spectral density.

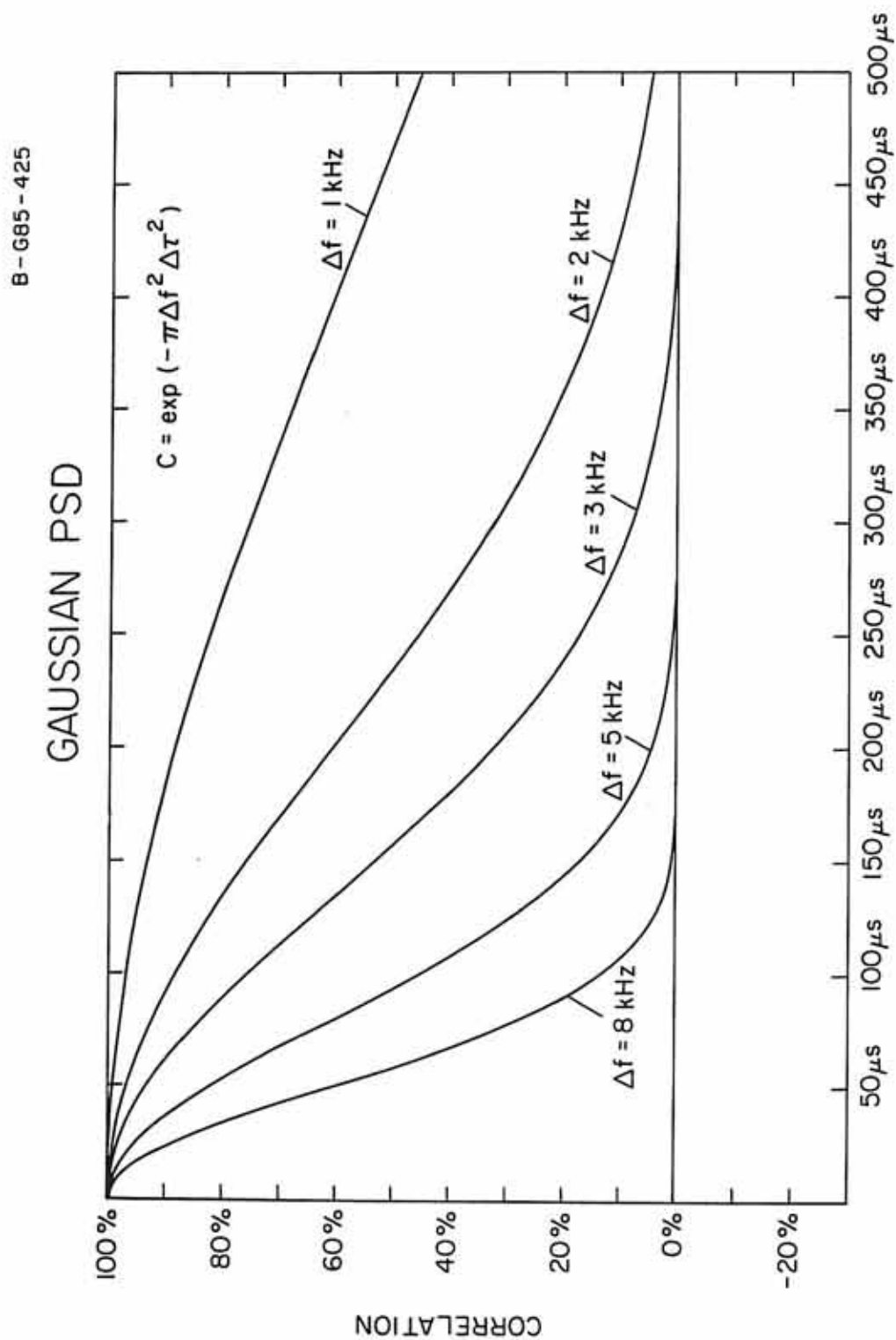
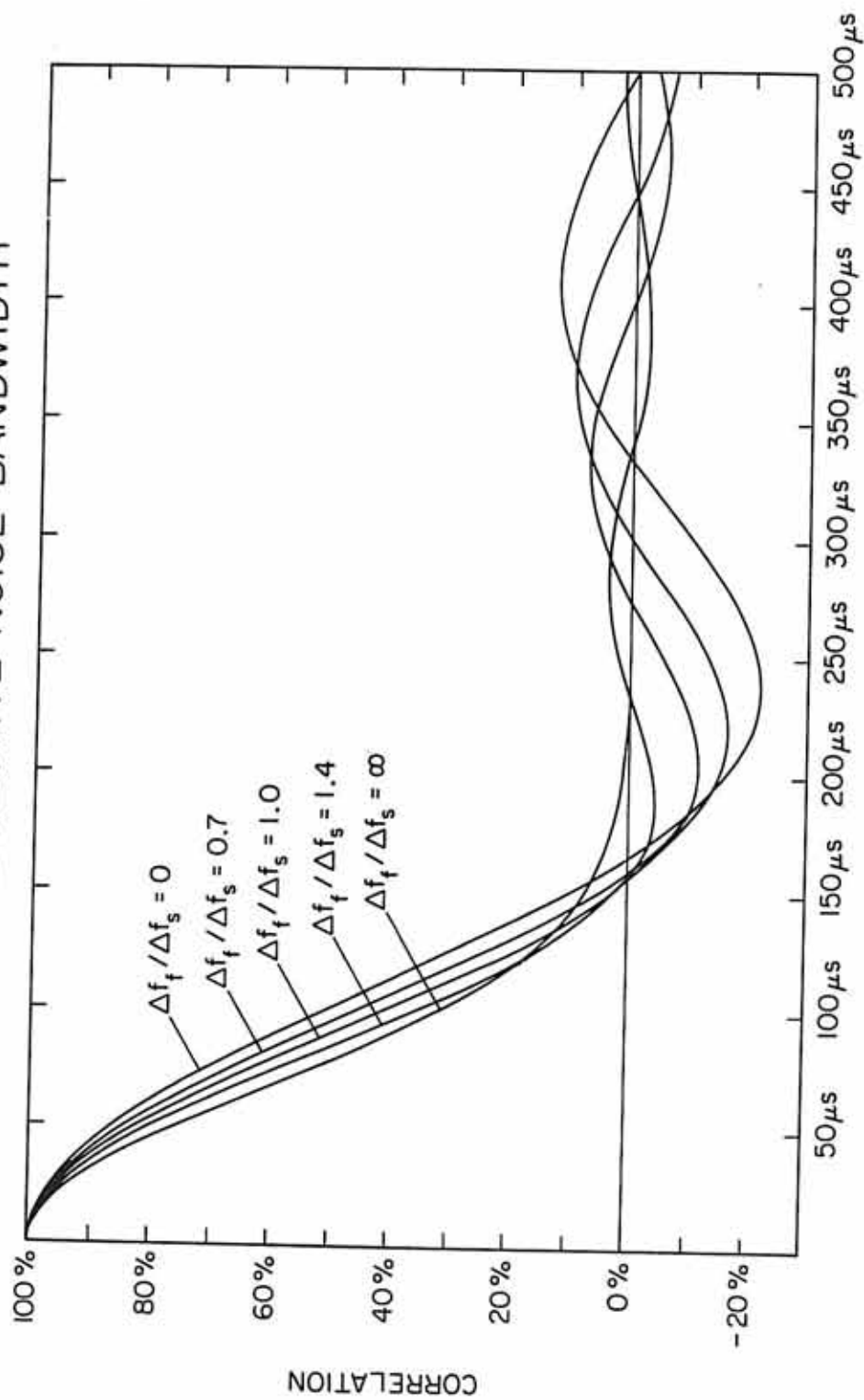
 $\Delta \tau$ (TIME DELAY)

Figure 12

Figure 13. This figure shows the correlation of a signal with a band-pass filtered Gaussian power spectral density, for different signal delays and ratios of filter bandwidth to signal bandwidth. The shape of the curves, for different filter bandwidth to signal bandwidth ratios, are very similar for correlations above 20 percent. This indicates that the bandwidth is more important in determining the rate of decrease in correlation, as a function of signal delay, than spectral shape.

FILTERED GAUSSIAN PSD 6 kHz EFFECTIVE NOISE BANDWIDTH



$\Delta\tau$ (TIME DELAY)

Figure 13

Figure 14. This figure shows the correlation of a two-dimensional Gaussian brightness distribution as a function of the source size multiplied by the baseline. The source size is defined as the angular width of the points where the brightness has been reduced by a factor of $1/e$. An interferometer can directly measure the source size only for incoherent radiation.

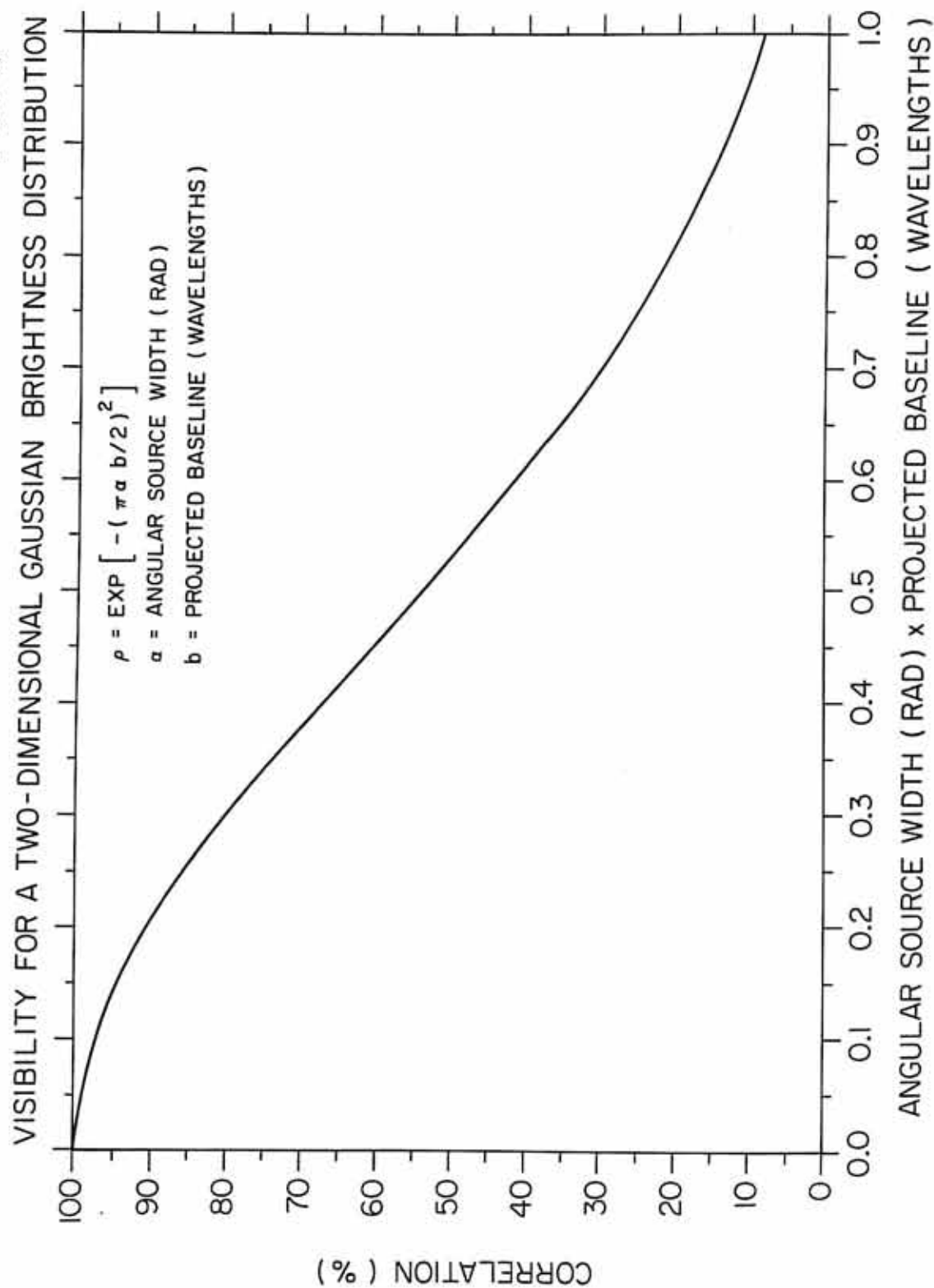
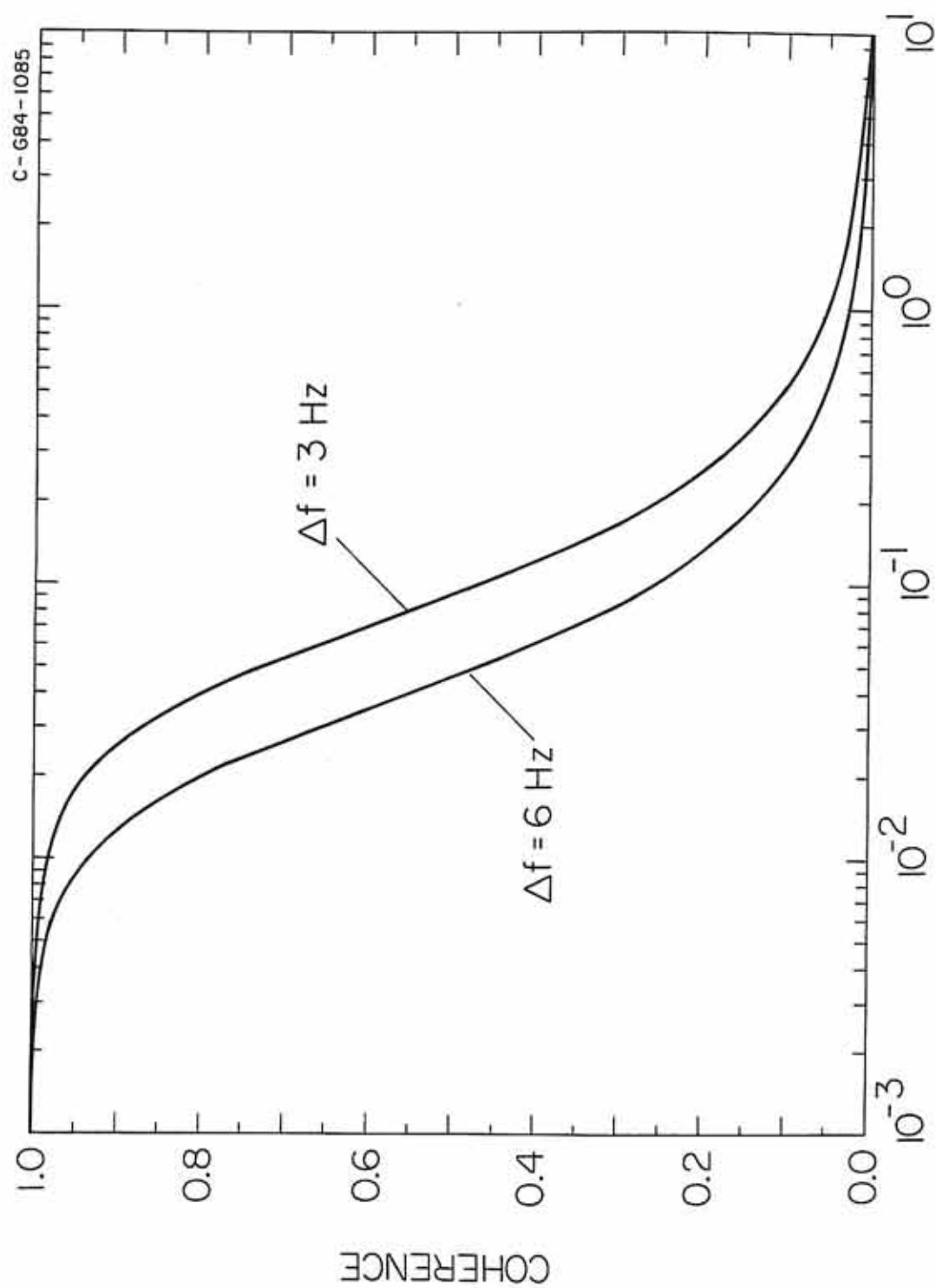


Figure 14

Figure 15. The integration time constant of the correlator will lower the measured correlation if the fringe rate is comparable to the time constant. This figure shows the coherence, as a function of the integration time constant, for fringe frequencies of 6 Hz (the fringe rate at 250 kHz) and 3 Hz (the fringe rate at 125 kHz). The time constant used in the correlator is 10 ms, thus the correlation is reduced by 2 percent for the 125 kHz data and by 5 percent for the 250 kHz data.



INTEGRATION TIME CONSTANT (SECONDS)

Figure 15

Figure 16. This figure shows a series of correlograms that was produced by correlating identical signals with white-noise power spectral densities, obtained during spacecraft integration, with different signal delays. The slope of the striations is a function of the signal delay, and thus can be used to determine the signal delay required to maximize the correlation.

ISEE FREQUENCY - TIME CORRELOGRAM
SEPT 19, 1977

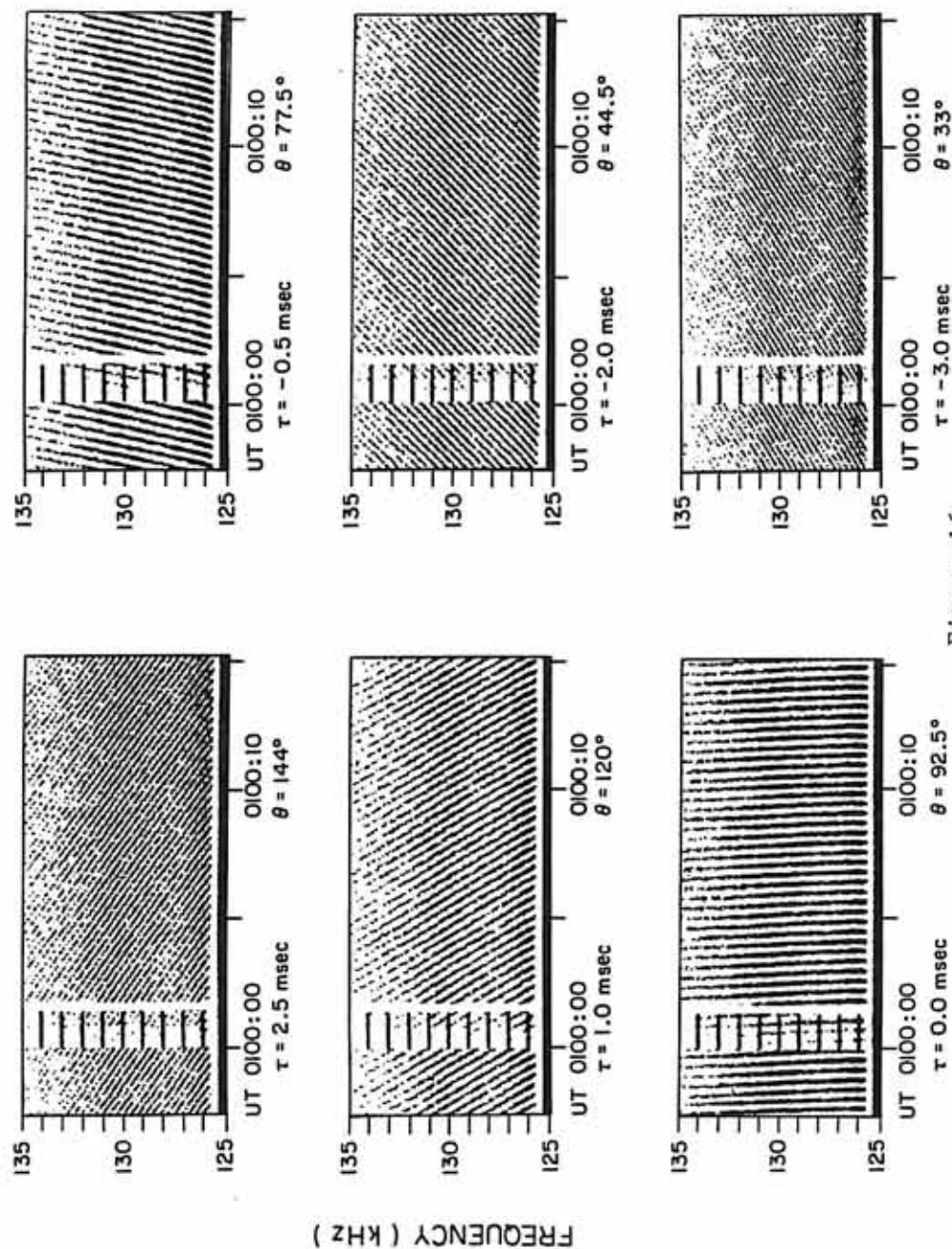


Figure 16

Figure 17. This figure is a plot of the reciprocal of the striation slope as a function of signal delay. From the slope of the striations, the desired signal delay can be determined to within $\pm 100 \mu\text{sec}$.

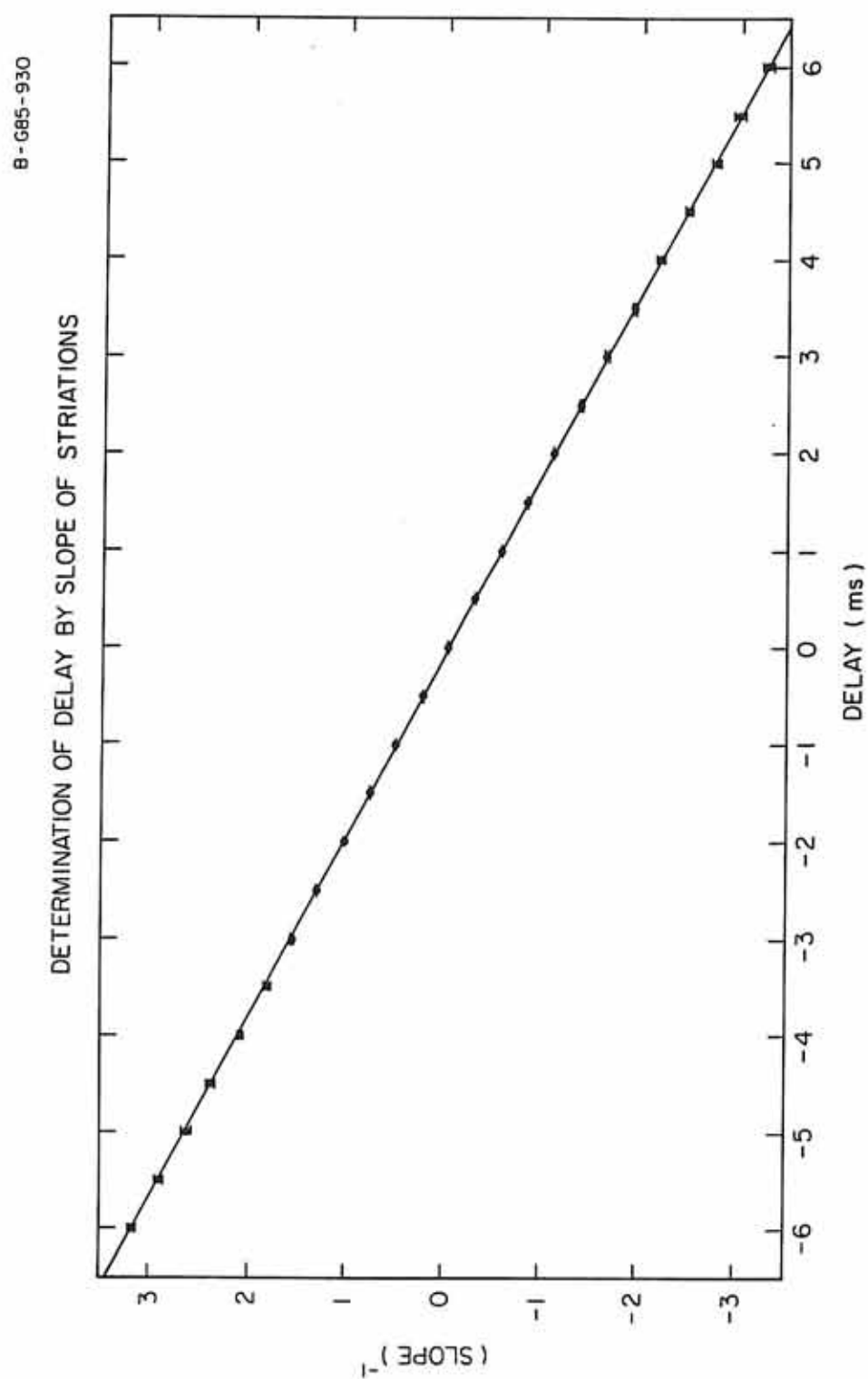


Figure 17

Figure 18. This figure shows the geometry of the field-aligned coordinate system chosen, to determine the projected baselines. The z axis of the source-centered coordinate system is along the source-baseline direction, and the magnetic field is in the y - z plane (the source-centered coordinate system can also be rotated so that the gradient of the magnetic field is in the y - z plane), to give baseline components parallel and perpendicular to the magnetic field (or gradient of the magnetic field).

B-G84-400-1

FIELD ALIGNED COORDINATE SYSTEM

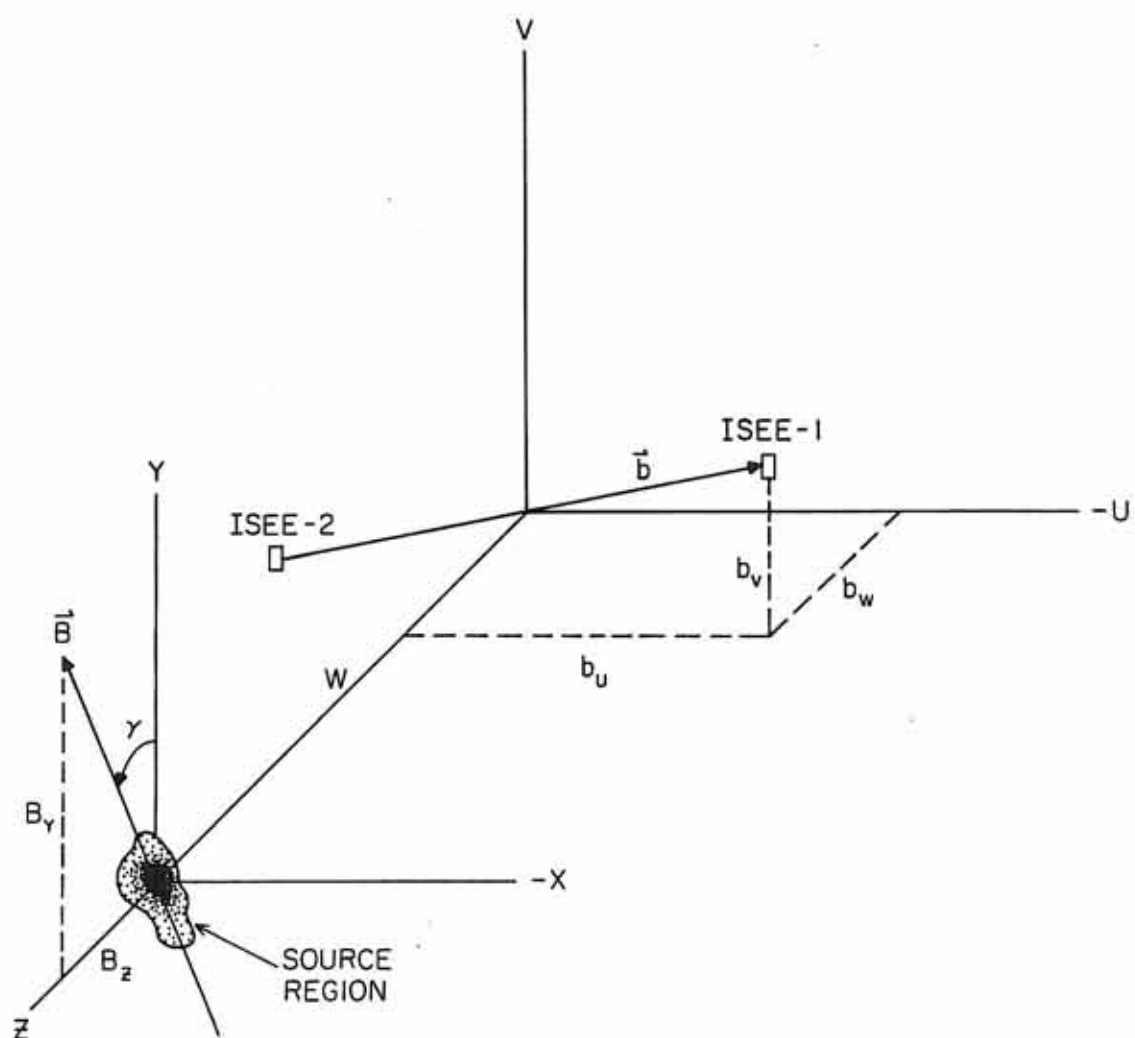


Figure 18

Figure 19. Spectrograms and correlograms for an AKR event detected by ISEE-1 and -2 on June 12, 1978. The top two panels show the independent spectrograms of the signals received by ISEE-2 and -1. The second two panels are frequency-time correlograms for this event. Nearly vertical striations can be seen in the correlograms, indicating that the signals are close to being correctly time aligned.

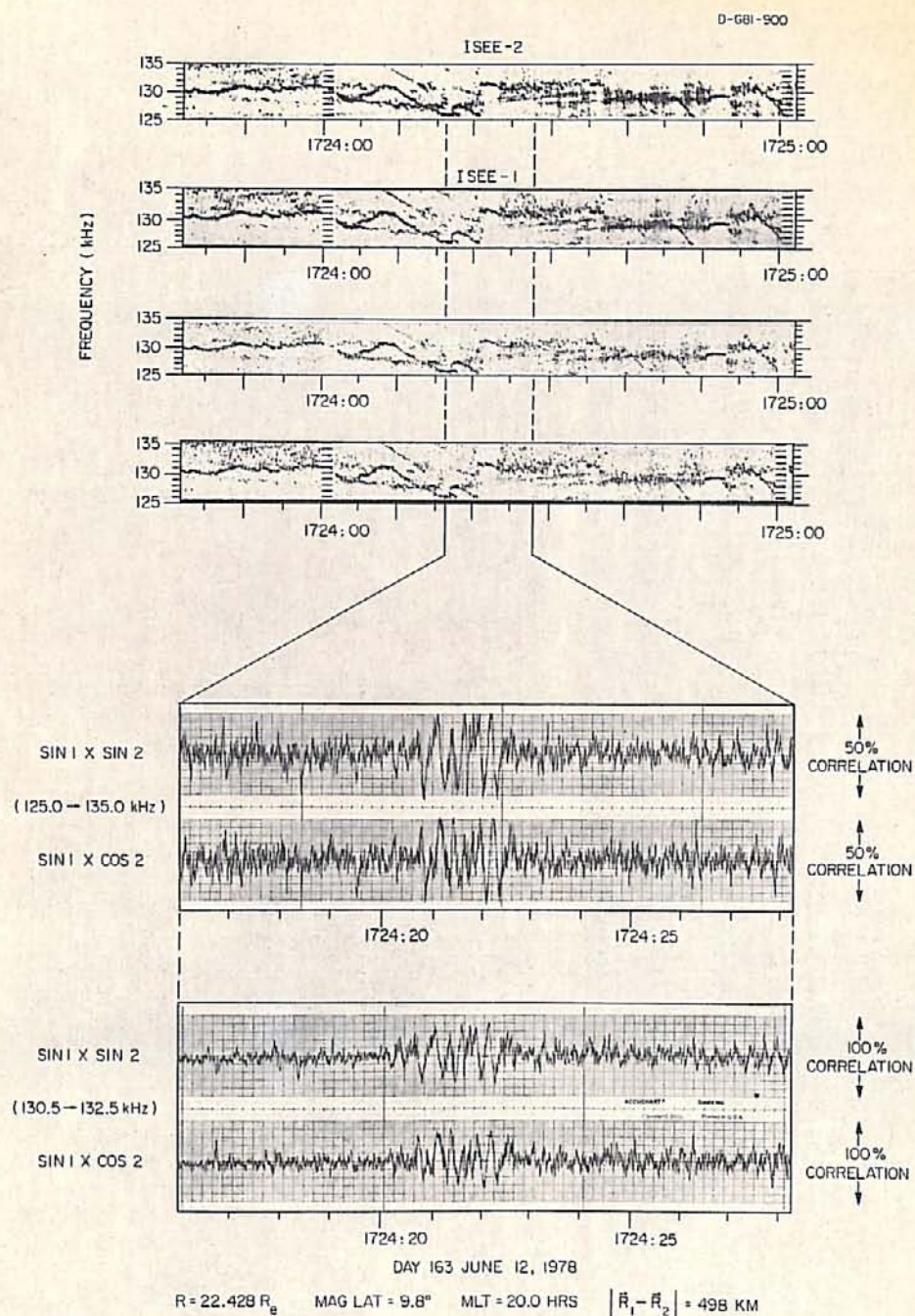


Figure 19

Figure 20. This figure is a continuation of the event shown in Figure 19. This event has regions where the bandwidth is extremely narrow, e.g., between 1725:07 UT and 1725:15 UT, and other regions where the signal bandwidth is several kilohertz. Comparison of the correlograms, for the unfiltered and filtered signals, shows that in addition to having a higher correlation when filtered signals are correlated, small amplitude fringes can be observed in the filtered signal correlogram that were not observed in the unfiltered correlogram (e.g., between 1724:46 UT and 1724:48 UT).

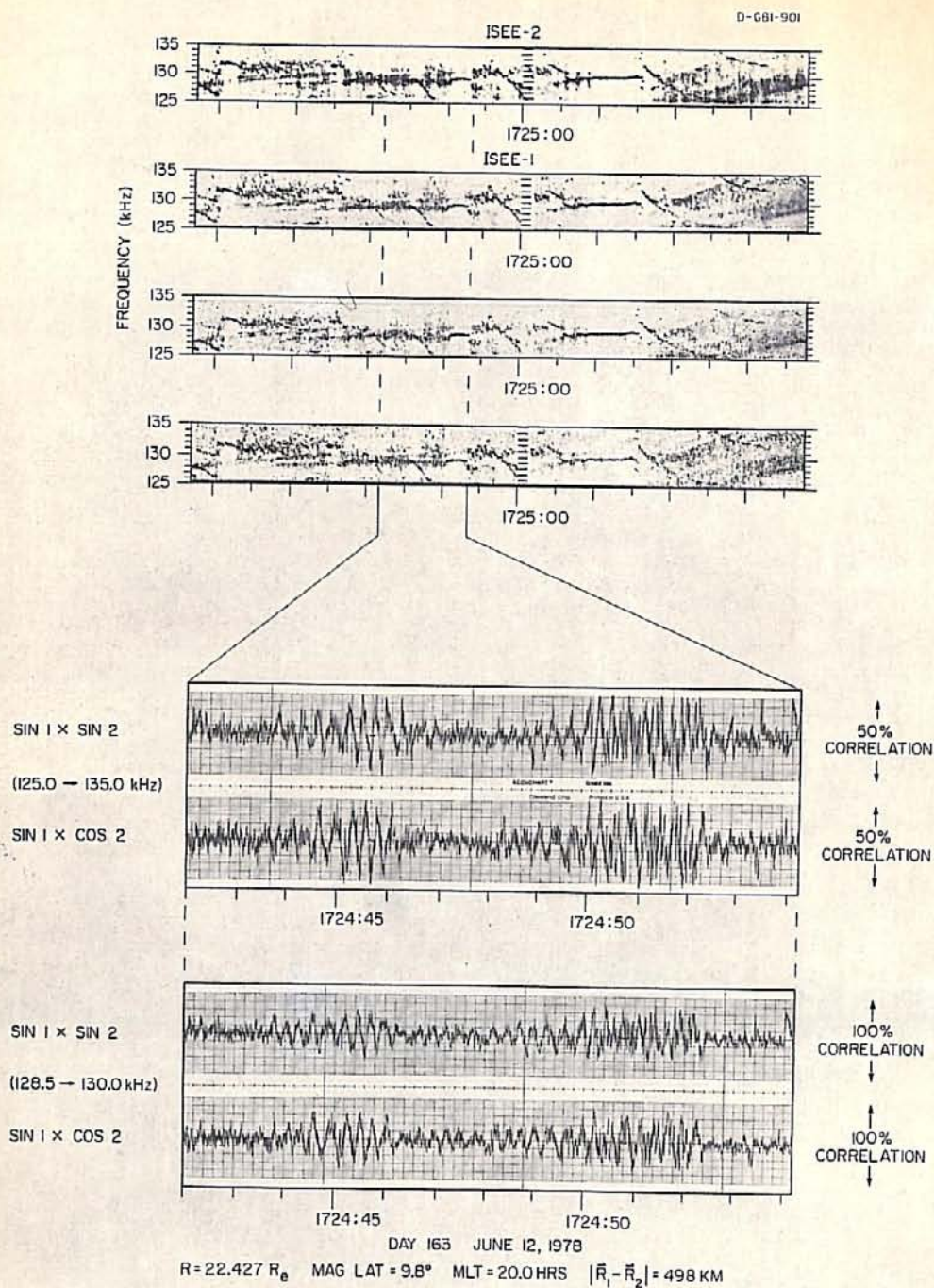


Figure 20

Figure 21. Spectrograms of three events detected by ISEE-1 and -2 on February 20, 1979 between 0038 UT and 0052 UT. Comparison of the signal amplitudes received by both spacecraft may help determine the size of the solid angle that an individual AKR event is beamed into.

B-G85-988

DAY 51, FEBRUARY 20, 1979

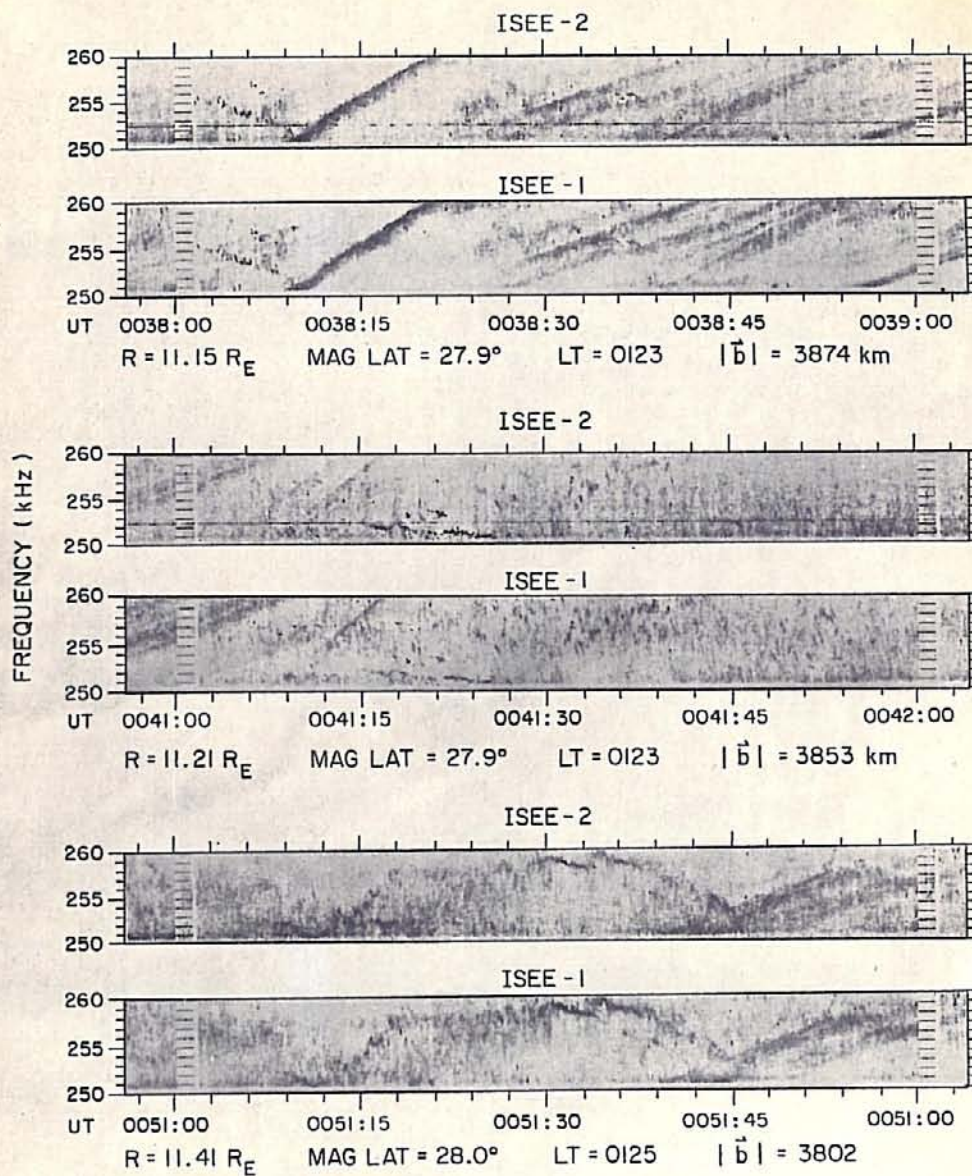


Figure 21

Figure 22. Spectrograms of three events detected by ISEE-1 and -2 on February 20, 1979 between 0307 UT and 0312 UT. The burst starting with a frequency near 4 kHz at 0308:10 appears to rapidly change bandwidth or amplitude. The burst rising in frequency at 0311:20 is another of the bursts analyzed.

B-685-989

DAY 51, FEBRUARY 20, 1979

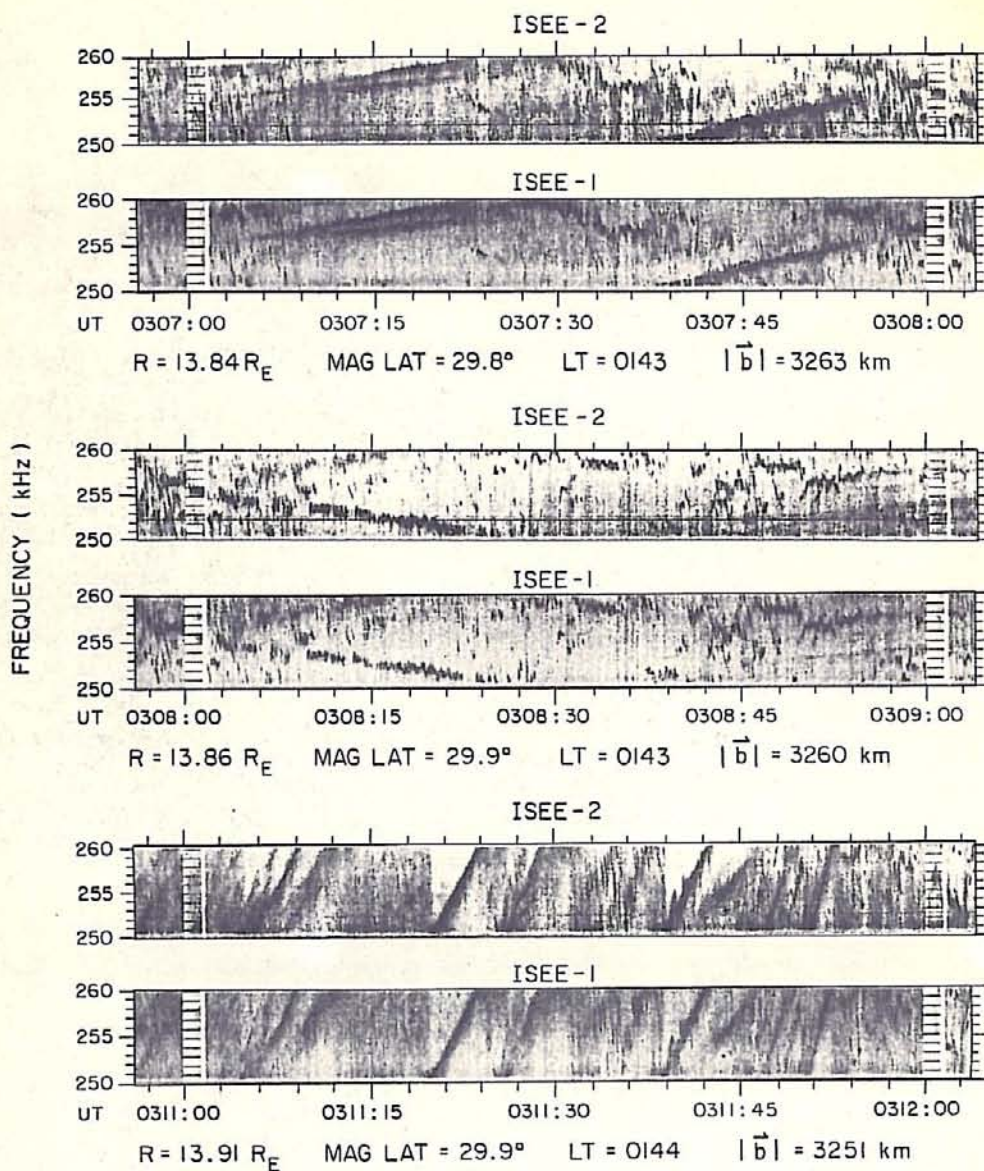


Figure 22

Figure 23. This figure is a delay-time correlogram for an AKR event detected on February 20, 1979. Since this burst has a very narrow bandwidth, the correlation remains large over a wide range of delays.

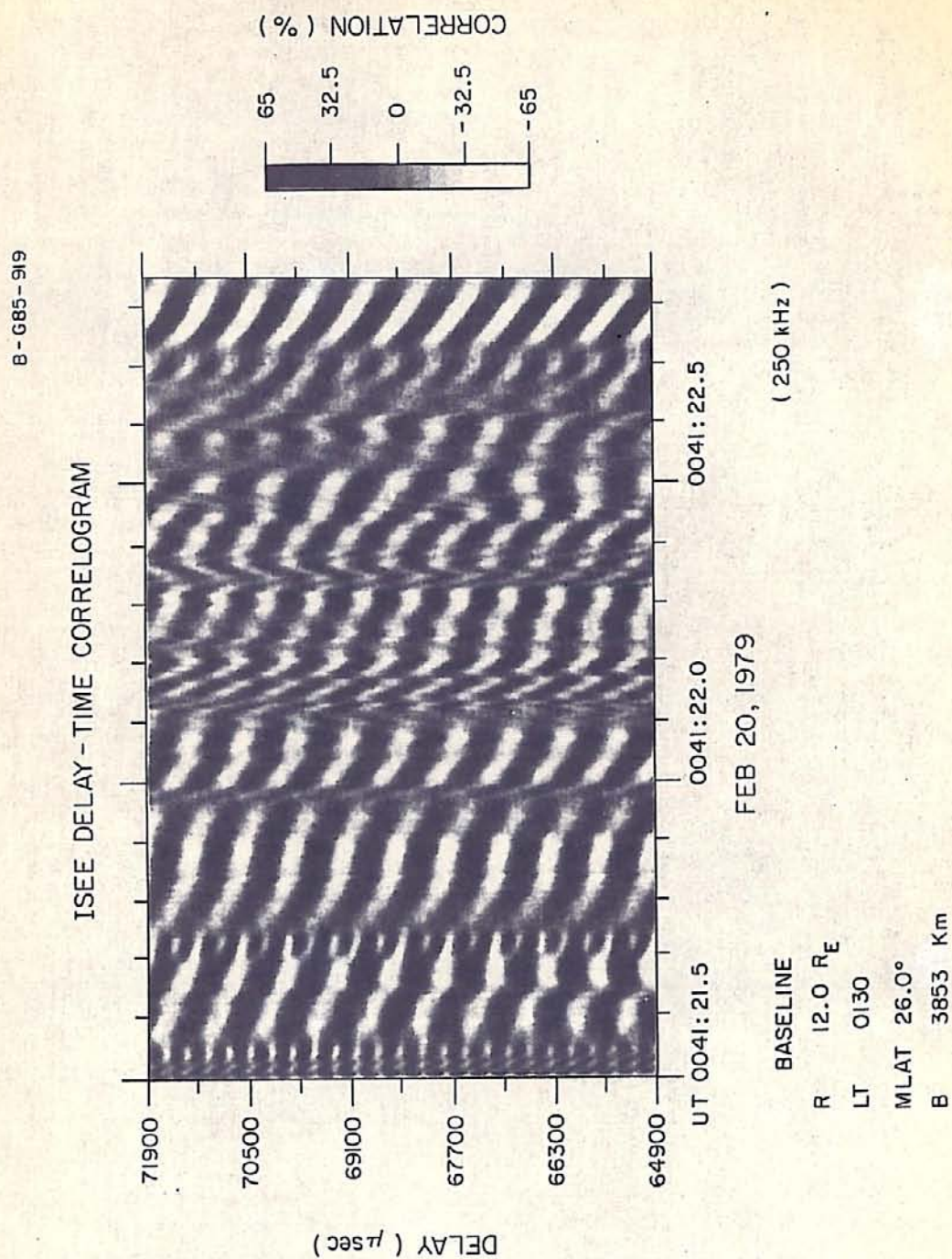


Figure 23

Figure 24. This figure is a time-delay correlogram for the same AKR burst as in Figure 23 but 1 second later. The abrupt phase changes in the correlation are presently not understood.

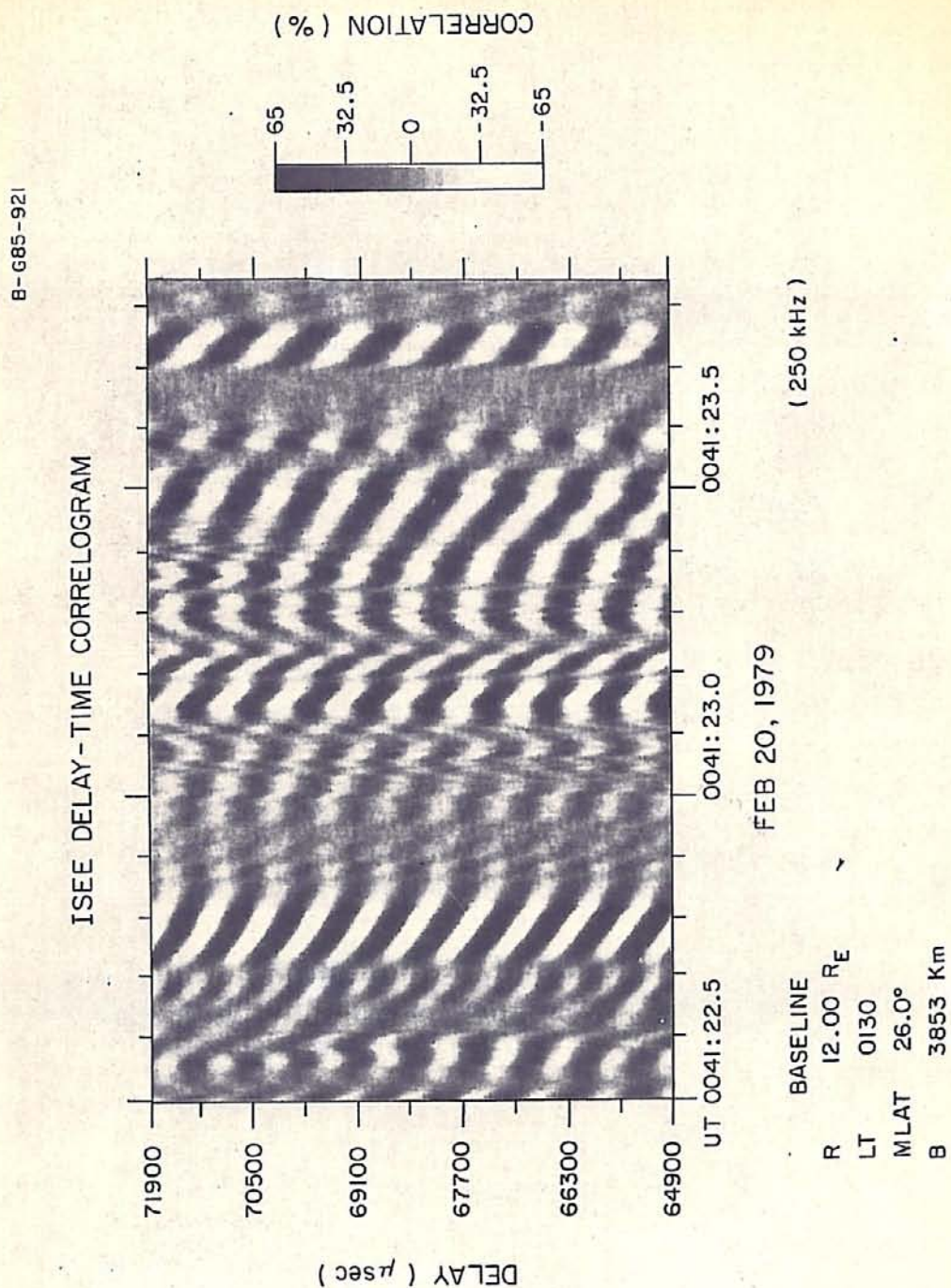
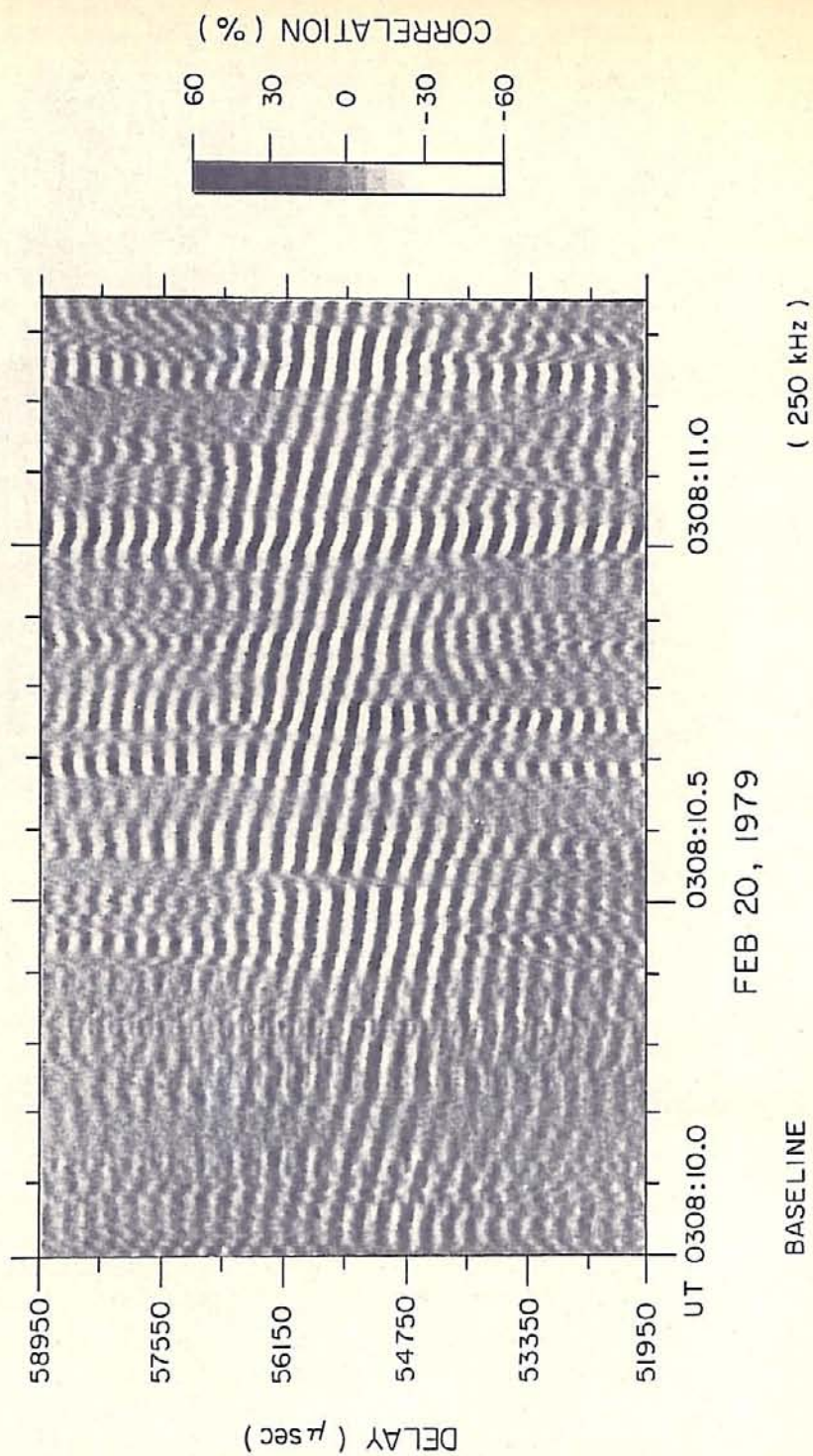


Figure 24

Figure 25. This delay-time correlogram shows the effect of signal bandwidth on the correlation for different signal delays. The correlation is maximized in the region where the striations are most uniform. There appears to be short time intervals where the bandwidth of the burst is narrower than at other times.

B-G85-922-1

ISEE DELAY-TIME CORRELOGRAM



BASELINE

R 14.49 R_E
 LT 0148
 MLAT 28.4°
 B 3260 Km

Figure 25

Figure 26. The vertical spacing of the fringes in a delay-time correlogram is a function of the center frequency of the correlated signals. As the frequency of the signals increases, the spacing of the fringes decreases.

B-G85-868

ISEE DELAY-TIME CORRELOGRAM

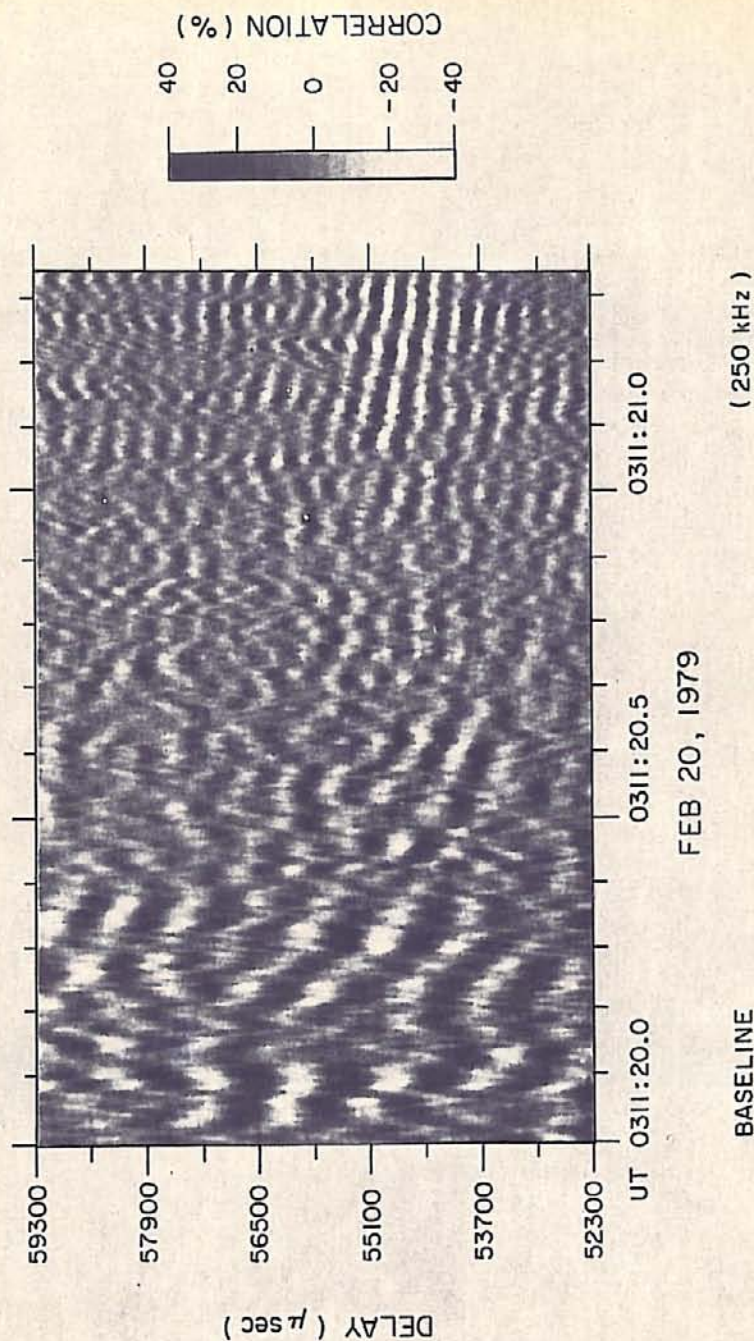


Figure 26

Figure 27. The correlation as a function of baseline is fit to a model source brightness distribution for incoherent sources. The source region diameter is determined primarily by the correlation at the longest baseline.

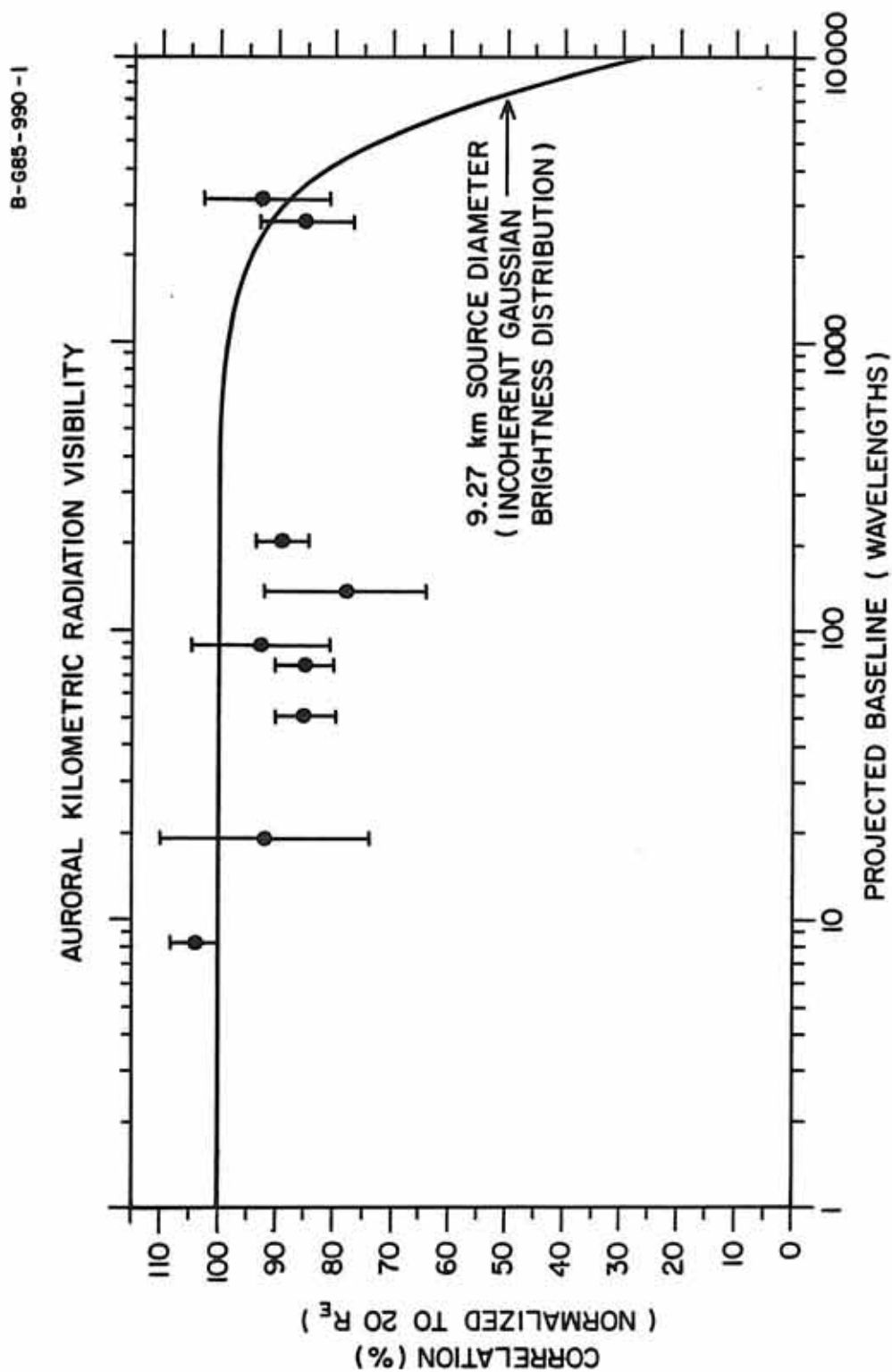


Figure 27

Figure 28. This figure shows the geometry of the amplifying region model. If the size of the amplifying region is comparable to the wavelength of the radiation, the angular size Ω of galactic background illuminating the spacecraft through the amplifier can be larger than the angular size θ of the amplifier as viewed from the spacecraft. For large amplifying regions, the two angular sizes Ω and θ are equal. For this model, the correlation is related to the area of overlap between the illumination cones for each spacecraft.

GEOMETRY OF AMPLIFIER MODEL

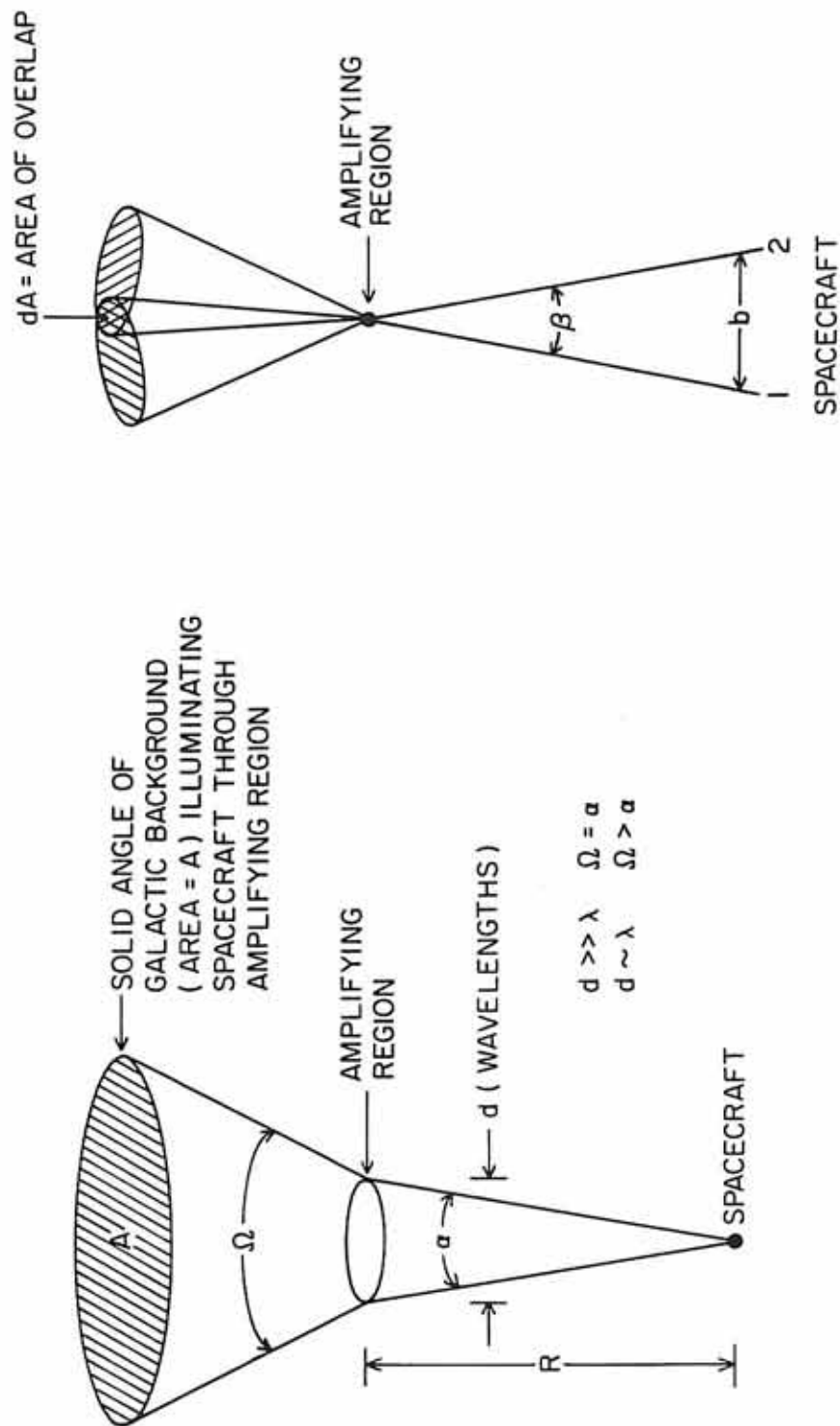


Figure 28

Figure 29. This figure is a plot of the correlation predicted by the amplifier model for different ratios of spacecraft separation to the angular size of the illumination cone. The correlation goes to zero when the illumination cones no longer overlap.

B-G85-944

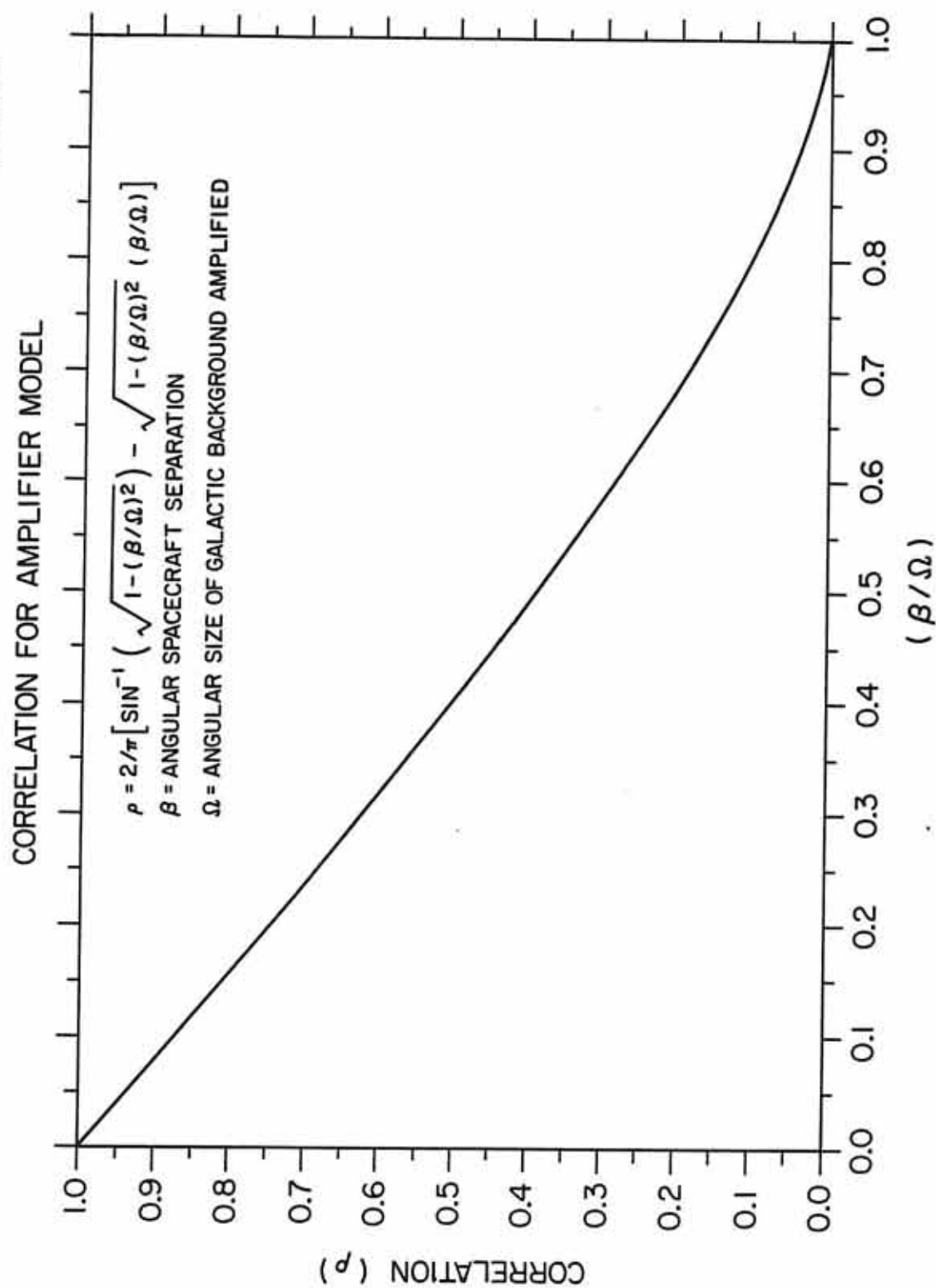


Figure 29

Figure 30. This figure shows the angular size of the radiation pattern from a coherent Gaussian brightness distribution, for different angular diameters of the brightness distribution. The angular size of the radiation pattern remains narrow until approximately 25 km for an emission frequency of 250 kHz.

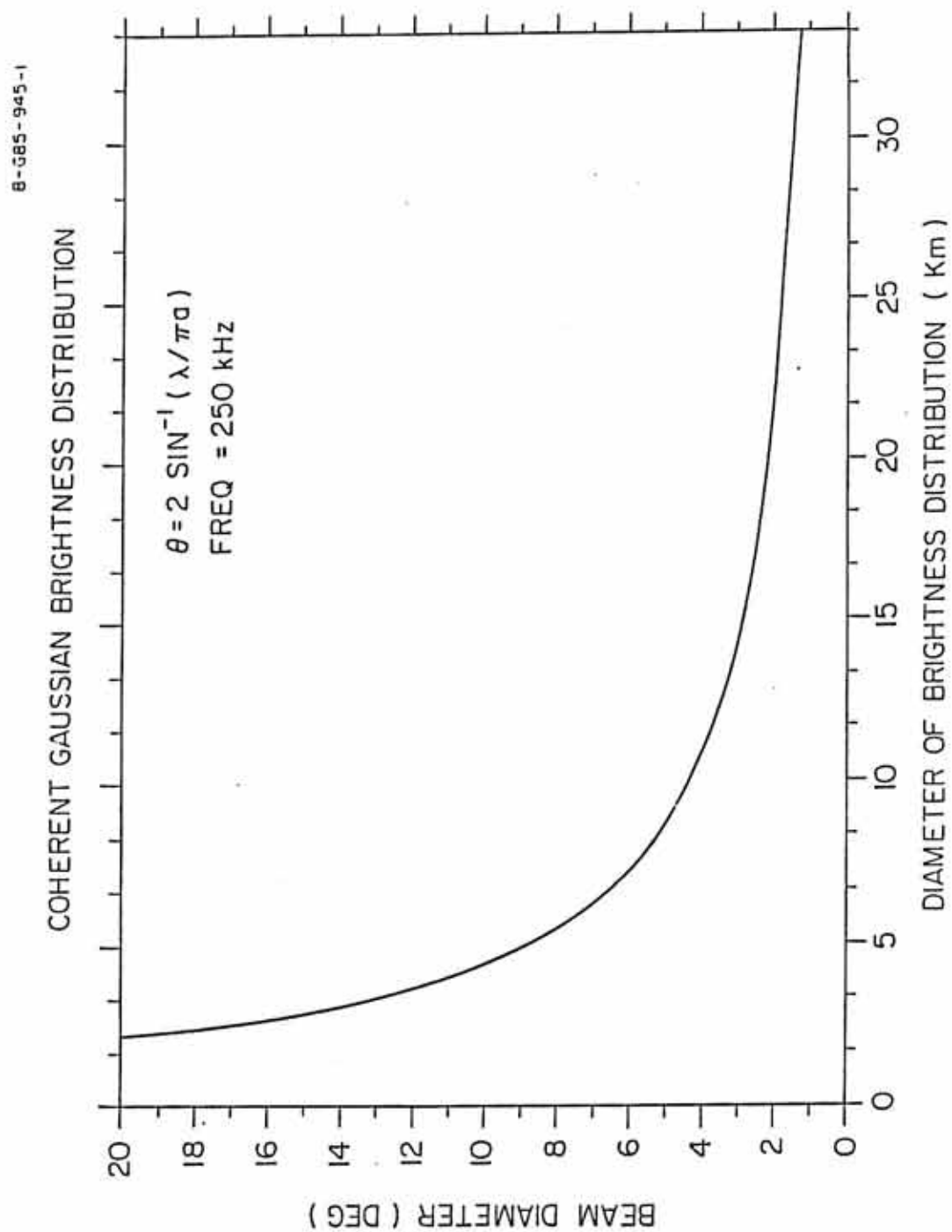


Figure 30

Figure 31. The total wave growth, required to explain the observed intensity of AKR, is plotted as a function of source region diameter. Decreasing the source region diameter by a factor of 10, increases the required wave growth by 20 db.

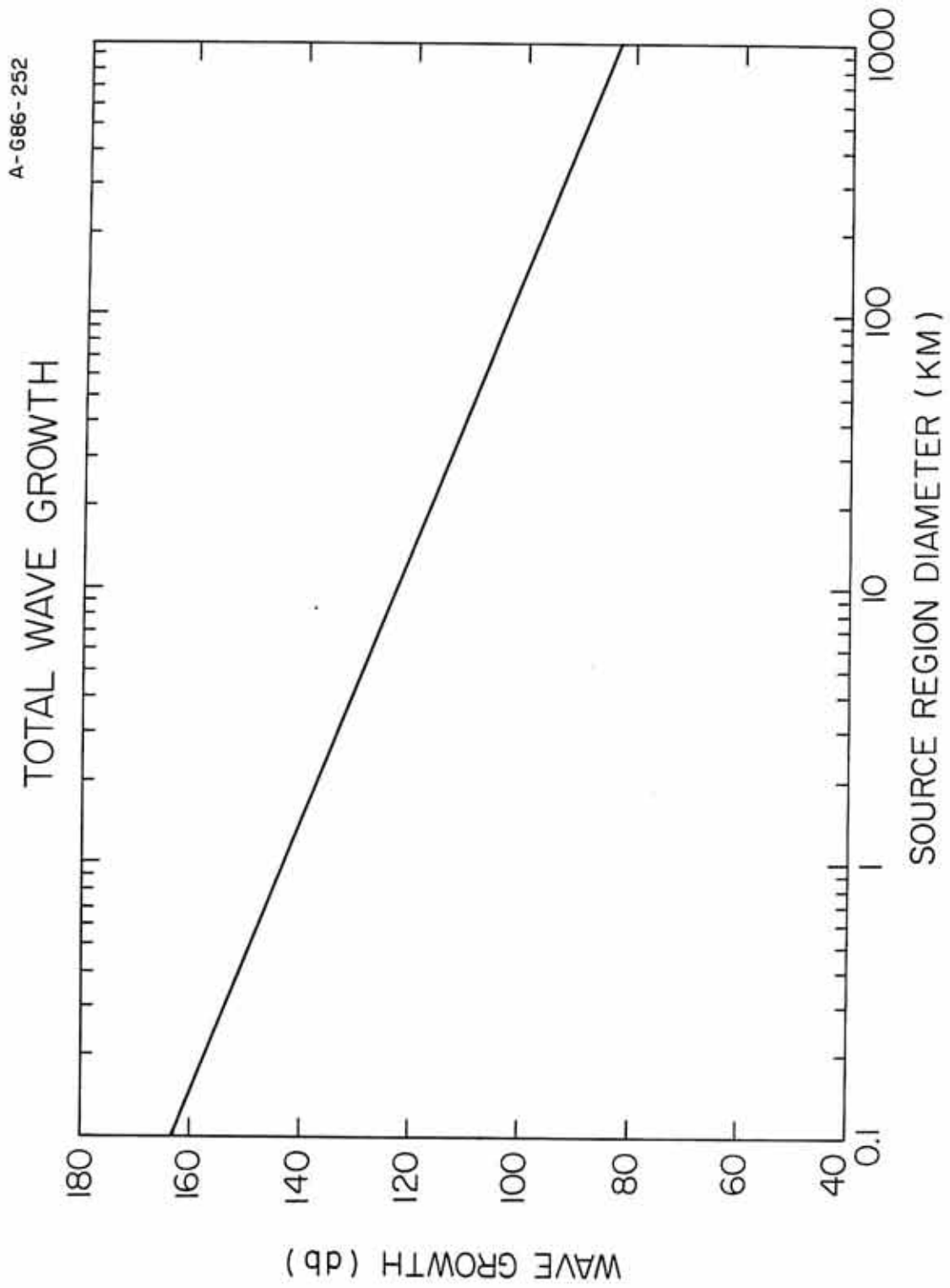


Figure 31

Figure 32. The growth rate, required to explain the observed intensity of AKR, is plotted as a function of source region diameter. The growth rate within the source region is assumed to be constant. The growth rate increases very rapidly for source region diameters less than 10 km.

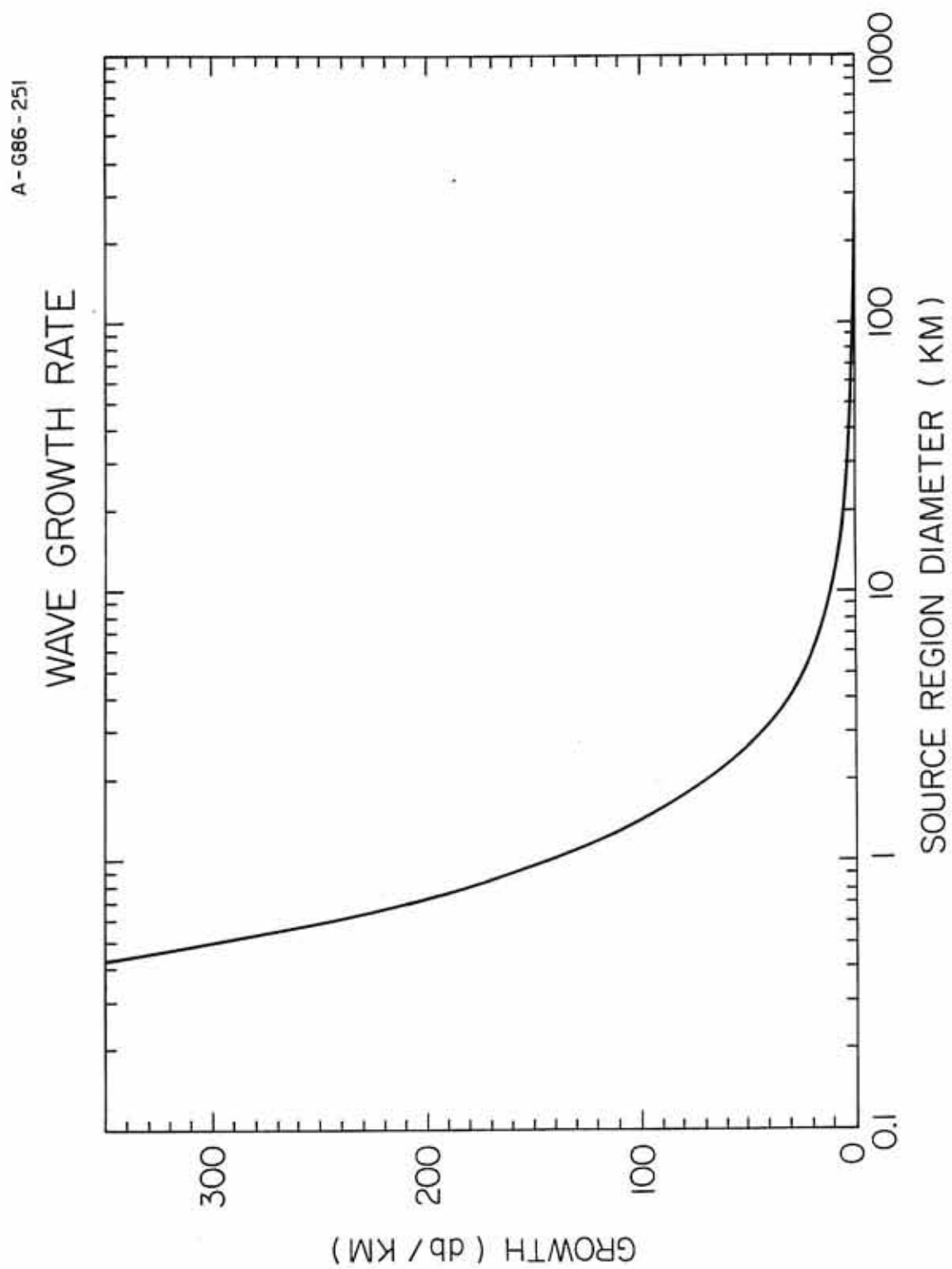


Figure 32

APPENDIX A

CALCULATION OF THE CROSS-CORRELATION FUNCTION

This derivation of the cross-correlation function follows the derivation of Rogers [1976], but includes the additional signal delays encountered with satellite-satellite interferometry.

For simplicity, it is assumed that the radio source is an unresolved point source, i.e., the angular size of the source is much less than the fringe spacing λ/D , and has white-noise or Gaussian spectral characteristics. The signals detected by each spacecraft are identical, but are displaced in time by an amount equal to the source-spacecraft propagation time difference. To compute the cross-correlation function $R_{xy}(\tau)$, the spectral and phase characteristics and delays of the detected signals must be calculated.

A. Cross-Correlation Function for an
Arbitrary Power Spectra

The signals detected by each spacecraft are:

$$x(t) = z(t - \tau_{s1}) \quad \text{for ISEE-1 and} \quad (A-1)$$

$$y(t) = z(t - \tau_{s2}) \quad \text{for ISEE-2} \quad , \quad (A-2)$$

where $z(t)$ represents the signal emitted from the source region, τ_{s1} is the propagation delay from the source region to ISEE-1 and τ_{s2} is the propagation delay from the source region to ISEE-2, and t is the time.

The Fourier transforms of the detected signals are:

$$X(\omega) = Z(\omega)e^{-i\omega\tau_{s1}} \quad \text{for ISEE-1 and} \quad (\text{A-3})$$

$$Y(\omega) = Z(\omega)e^{-i\omega\tau_{s2}} \quad \text{for ISEE-2} \quad . \quad (\text{A-4})$$

At each spacecraft a single-sideband receiver translates the 10 kHz observing frequency window downward to the range of 0 to 10 kHz. The conversion frequency is derived from a crystal oscillator in each receiver. The primary cause of the observed fringes in the cross-correlation function is the small difference (on the order of 1 to 10 Hz) between the conversion frequencies in each receiver. The single-sideband receiver outputs are:

$$x'(t) = x(t)\cos(\omega_x t + \phi_x) + [x(t)\cos(\omega_x t + \phi_x + \pi/2)]_{\mathcal{L}\pi/2} \quad (\text{A-5})$$

$$\begin{aligned} x'(t) = & \frac{1}{2} x(t) \left[\exp\left\{i\left[\left(\omega_0 + \frac{\Delta\omega_0}{2}\right)t + \phi_x\right]\right\} + \exp\left\{-i\left[\left(\omega_0 + \frac{\Delta\omega_0}{2}\right)t + \phi_x\right]\right\} \right] \\ & + \left[\frac{1}{2} \frac{x(t)}{1} \left[\exp\left\{-i\left[\left(\omega_0 + \frac{\Delta\omega_0}{2}\right)t + \phi_x\right]\right\} \right. \right. \\ & \left. \left. - \exp\left\{i\left[\left(\omega_0 + \frac{\Delta\omega_0}{2}\right)t + \phi_x\right]\right\} \right] \right]_{\mathcal{L}\pi/2} \end{aligned} \quad (\text{A-6})$$

for ISEE-1 and

$$y'(t) = y(t)\cos(\omega_y t + \phi_y) + [y(t)\cos(\omega_y t + \phi_y + \pi/2)]_{L\pi/2} \quad (\text{A-7})$$

$$\begin{aligned} y'(t) = & \frac{1}{2} y(t) \left[\exp\left\{i\left[\left(\omega_0 - \frac{\Delta\omega_0}{2}\right)t + \phi_y\right]\right\} + \exp\left\{-i\left[\left(\omega_0 - \frac{\Delta\omega_0}{2}\right)t + \phi_y\right]\right\} \right] \\ & + \left[\frac{1}{2} \frac{y(t)}{i} \left[\exp\left\{-i\left[\left(\omega_0 - \frac{\Delta\omega_0}{2}\right)t + \phi_y\right]\right\} \right. \right. \\ & \left. \left. - \exp\left\{-i\left[\left(\omega_0 - \frac{\Delta\omega_0}{2}\right)t + \phi_y\right]\right\} \right] \right]_{L\pi/2} \end{aligned} \quad (\text{A-8})$$

for ISEE-2, where ϕ_x and ϕ_y represent the initial phase of the local oscillators in the ISEE-1 and -2 receivers, and ω_x and ω_y are the conversion frequencies.

Let

$$\omega_x = \omega_0 + \Delta\omega_0/2 \quad \text{and} \quad \omega_y = \omega_0 - \Delta\omega_0/2 \quad , \quad (\text{A-9})$$

where

ω_x is the ISEE-1 receiver conversion frequency,
 ω_y is the ISEE-2 receiver conversion frequency,
 ω_0 is the average receiver conversion frequency, and
 $\Delta\omega_0$ is the difference between the ISEE-1 and ISEE-2
 receiver conversion frequencies.

To compute the Fourier transform of the phase-shifted signal, we must divide the Fourier transform into pieces.

Let

$$X(\omega) = X_{>\omega_X}(\omega) + X_{<\omega_X}(\omega) \quad (\text{A-10})$$

$$= X_{>-\omega_X}(\omega) + X_{<-\omega_X}(\omega) \quad (\text{A-11})$$

and

$$Y(\omega) = Y_{>\omega_X}(\omega) + Y_{<\omega_X}(\omega) \quad (\text{A-12})$$

$$= Y_{>-\omega_X}(\omega) + Y_{<-\omega_X}(\omega) \quad , \quad (\text{A-13})$$

where the subscripts indicate the region in which the transform is nonzero.

$$X_{>\omega_X}(\omega) = \begin{cases} X(\omega) & \omega > \omega_X \\ 0 & \omega < \omega_X \end{cases} \quad (\text{A-14})$$

$$X_{<\omega_X}(\omega) = \begin{cases} X(\omega) & \omega < \omega_X \\ 0 & \omega > \omega_X \end{cases} \quad (\text{A-15})$$

$$X_{>-\omega_X}(\omega) = \begin{cases} X(\omega) & \omega > -\omega_X \\ 0 & \omega < -\omega_X \end{cases} \quad (\text{A-16})$$

$$X_{<-\omega_x}(\omega) = \begin{cases} X(\omega) & \omega < -\omega_x \\ 0 & \omega > -\omega_x \end{cases} \quad (\text{A-17})$$

$$Y_{>\omega_y}(\omega) = \begin{cases} Y(\omega) & \omega > \omega_y \\ 0 & \omega < \omega_y \end{cases} \quad (\text{A-18})$$

$$Y_{<\omega_y}(\omega) = \begin{cases} Y(\omega) & \omega < \omega_y \\ 0 & \omega > \omega_y \end{cases} \quad (\text{A-19})$$

$$Y_{>-\omega_y}(\omega) = \begin{cases} Y(\omega) & \omega > -\omega_y \\ 0 & \omega < -\omega_y \end{cases} \quad (\text{A-20})$$

$$Y_{<-\omega_y}(\omega) = \begin{cases} Y(\omega) & \omega < -\omega_y \\ 0 & \omega > -\omega_y \end{cases} \quad (\text{A-21})$$

The Fourier transform of the single-sideband receiver outputs can be found by taking the Fourier transforms of equations (A-6) and (A-8) and substituting (A-14) through (A-21) into the result.

The Fourier transform of the receiver outputs are:

$$\begin{aligned} X'(\omega) = & \frac{1}{2} [X_{>-\omega_x}(\omega - \omega_0 - \Delta\omega_0/2)e^{i\phi_x} + X_{<-\omega_x}(\omega - \omega_0 - \Delta\omega_0/2)e^{i\phi_x} \\ & + X_{>\omega_x}(\omega + \omega_0 + \Delta\omega_0/2)e^{-i\phi_x} + X_{<\omega_x}(\omega + \omega_0 + \Delta\omega_0/2)e^{-i\phi_x}] \\ & + \frac{i}{2} [X_{>-\omega_x}(\omega - \omega_0 - \Delta\omega_0/2)e^{i\phi_x} + X_{<-\omega_x}(\omega - \omega_0 - \Delta\omega_0/2)e^{i\phi_x} \\ & - X_{>\omega_x}(\omega + \omega_0 + \Delta\omega_0/2)e^{-i\phi_x} - X_{<\omega_x}(\omega + \omega_0 + \Delta\omega_0/2)e^{-i\phi_x}]_{L\pi/2} \end{aligned} \quad (\text{A-22})$$

$$\begin{aligned}
Y'(\omega) = & \frac{1}{2} [Y_{>-\omega_x}(\omega - \omega_0 + \Delta\omega_0/2)e^{i\phi_y} + Y_{<-\omega_y}(\omega - \omega_0 + \Delta\omega_0/2)e^{i\phi_y} \\
& + Y_{>\omega_y}(\omega + \omega_0 - \Delta\omega_0/2)e^{-i\phi_y} + Y_{<\omega_y}(\omega + \omega_0 - \Delta\omega_0/2)e^{-i\phi_y}] \\
& + \frac{i}{2} [Y_{>-\omega_y}(\omega - \omega_0 + \Delta\omega_0/2)e^{i\phi_y} + Y_{<-\omega_y}(\omega - \omega_0 + \Delta\omega_0/2)e^{i\phi_y} \\
& - Y_{>\omega_y}(\omega + \omega_0 - \Delta\omega_0/2)e^{-i\phi_y} - Y_{<\omega_y}(\omega + \omega_0 - \Delta\omega_0/2)e^{-i\phi_y}]_{L\pi/2}
\end{aligned}
\tag{A-23}$$

Since the phase of a signal is always an odd function of frequency, the Fourier transform of a signal phase shifted by 90° is:

$$F_{L\pi/2}(\omega) = \begin{cases} 1 F(\omega) & , \quad \omega > 0 \\ -1 F(\omega) & , \quad \omega < 0 \end{cases} . \tag{A-24}$$

Applying the 90° phase shift to equations (A-22) and (A-23), and summing gives the Fourier transform of the receiver outputs:

$$\begin{aligned}
X'(\omega) &= X(\omega + \omega_0 + \Delta\omega_0/2)e^{-i\phi_x} \quad \omega > 0 \\
&= X(\omega - \omega_0 - \Delta\omega_0/2)e^{i\phi_x} \quad \omega < 0 \text{ for ISEE-1}
\end{aligned}
\tag{A-25}$$

and

$$Y'(\omega) = Y(\omega + \omega_0 - \Delta\omega_0/2)e^{-i\phi_y} \quad \omega > 0$$

$$Y(\omega - \omega_0 + \Delta\omega_0/2)e^{i\phi_y} \quad \omega < 0 \text{ for ISEE-2} \quad . \quad (\text{A-26})$$

At the telemetry station the received signals are:

$$x''(t) = x'(t - \tau_{g1}) \quad \text{for ISEE-1 and} \quad (\text{A-27})$$

$$y''(t) = y'(t - \tau_{g2}) \quad \text{for ISEE-2} \quad , \quad (\text{A-28})$$

where τ_{g1} is the propagation delay from ISEE-1 to the telemetry station and τ_{g2} is the propagation delay from ISEE-2 to the telemetry station. The Fourier transforms of the signals received at the telemetry stations are:

$$X''(\omega) = X'(\omega)e^{-i\omega\tau_{g1}} \quad \text{for ISEE-1 and} \quad (\text{A-29})$$

$$Y''(\omega) = Y'(\omega)e^{-i\omega\tau_{g2}} \quad \text{for ISEE-2} \quad . \quad (\text{A-30})$$

$X''(\omega)$ and $Y''(\omega)$ in terms of $Z(\omega)$, the Fourier transform of the signal emitted from the source region, can be found by substituting equations (A-3) and (A-25) into equation (A-29) and by substituting equations (A-4) and (A-26) into equation (A-30).

The results of these substitutions are:

$$\begin{aligned} X^*(\omega) &= e^{-i[\omega\tau_{g1} + \phi_x + (\omega + \omega_0 + \Delta\omega_0/2)\tau_{s1}]} Z(\omega + \omega_0 + \Delta\omega_0/2) \quad \omega > 0 \\ &= e^{-i[\omega\tau_{g1} - \phi_x + (\omega - \omega_0 - \Delta\omega_0/2)\tau_{s1}]} Z(\omega - \omega_0 - \Delta\omega_0/2) \quad \omega < 0 \quad (A-31) \end{aligned}$$

and

$$\begin{aligned} Y^*(\omega) &= e^{-i[\omega\tau_{g2} + \phi_y + (\omega + \omega_0 - \Delta\omega_0/2)\tau_{s2}]} Z(\omega + \omega_0 - \Delta\omega_0/2) \quad \omega > 0 \\ &= e^{-i[\omega\tau_{g2} - \phi_y + (\omega - \omega_0 + \Delta\omega_0/2)\tau_{s2}]} Z(\omega - \omega_0 + \Delta\omega_0/2) \quad \omega < 0 \quad . \\ & \hspace{15em} (A-32) \end{aligned}$$

The cross-spectral function,

$$S_{xy}(\omega) = X^*(\omega)Y^{**}(\omega) \quad , \quad (A-33)$$

is the Fourier transform of the cross-correlation function $R_{xy}(\tau)$.

The result of substituting equation (A-31) and the complex conjugate of equation (A-32) into equation (A-33) is:

$$\begin{aligned} S_{xy} &= Z(\omega + \omega_0 + \Delta\omega_0/2)Z^*(\omega + \omega_0 - \Delta\omega_0/2)e^{-i[(\omega + \omega_0)\tau' + \theta]} \quad \omega > 0 \\ &= Z(\omega - \omega_0 - \Delta\omega_0/2)Z^*(\omega - \omega_0 + \Delta\omega_0/2)e^{-i[(\omega - \omega_0)\tau' - \theta]} \quad \omega < 0 \quad , \\ & \hspace{15em} (A-34) \end{aligned}$$

where

$$\tau' = \tau_{s1} + \tau_{g1} - \tau_{s2} - \tau_{g2}$$

and

$$\theta = \phi_x - \phi_y + \Delta\omega_0(\tau_{s1} + \tau_{s2})/2 - \omega_0(\tau_{g1} - \tau_{g2}) \quad . \quad (\text{A-35})$$

Using the approximation

$$F(\omega + \Delta\omega/2)F^*(\omega - \Delta\omega/2) \sim F(\omega)F^*(\omega)e^{-i\Delta\omega t} \quad (\text{A-36})$$

[Rogers, 1976],

$$\begin{aligned} S_{xy} &= Z(\omega + \omega_0)Z^*(\omega + \omega_0)e^{-i[(\omega + \omega_0)\tau' + \theta + \Delta\omega_0 t]} \quad \omega > 0 \\ &= Z(\omega - \omega_0)Z^*(\omega - \omega_0)e^{-i[(\omega - \omega_0)\tau' - \theta - \Delta\omega_0 t]} \quad \omega < 0 \quad . \end{aligned} \quad (\text{A-37})$$

The cross-correlation function $R_{xy}(\tau)$ is defined by

$$R_{xy}(\tau) = \frac{1}{2\pi} \int_{-\infty}^{\infty} S_{xy}(\omega)e^{i\omega\tau} d\omega \quad . \quad (\text{A-38})$$

$$\begin{aligned}
R_{xy}(\tau) &= \frac{1}{2\pi} \int_{-\infty}^0 Z(\omega - \omega_0) Z^*(\omega - \omega_0) e^{-i[(\omega - \omega_0)\tau' - \theta - \Delta\omega_0 t]} e^{i\omega\tau} d\omega \\
&\quad + \frac{1}{2\pi} \int_0^{\infty} Z(\omega + \omega_0) Z^*(\omega + \omega_0) e^{-i[(\omega + \omega_0)\tau' + \theta + \Delta\omega_0 t]} e^{i\omega\tau} d\omega .
\end{aligned}$$

(A-39)

Let

$$\omega' = \omega - \omega_0 \quad \text{for } \omega < 0 \text{ and}$$

$$\omega' = \omega + \omega_0 \quad \text{for } \omega > 0 .$$

Thus,

$$\begin{aligned}
R_{xy} &= \frac{1}{2\pi} \int_{-\infty}^{-\omega_0} Z(\omega') Z^*(\omega') e^{-i(-\Delta\omega_0 t + \omega' \tau' - \theta)} e^{i(\omega' + \omega_0)\tau} d\omega' \\
&\quad + \frac{1}{2\pi} \int_{\omega_0}^{\infty} Z(\omega') Z^*(\omega') e^{-i(\Delta\omega_0 t + \omega' \tau' + \theta)} e^{i(\omega' - \omega_0)\tau} d\omega'
\end{aligned}$$

(A-40)

$$\begin{aligned}
R_{xy} &= \frac{1}{2\pi} [e^{i(\Delta\omega_0 t + \theta + \omega_0 \tau)}] \int_{-\infty}^{-\omega_0} Z(\omega') Z^*(\omega') e^{i\omega'(\tau - \tau')} d\omega' \\
&\quad + \frac{1}{2\pi} [e^{-i(\Delta\omega_0 t + \theta + \omega_0 \tau)}] \int_{\omega_0}^{\infty} Z(\omega') Z^*(\omega') e^{i\omega'(\tau - \tau')} d\omega' .
\end{aligned}$$

(A-41)

We can introduce the receiver bandwidth into equation (A-41) by integrating from $-\omega_1$, to $-\omega_0$ and from ω_0 to ω_1 , where ω_1 is the upper band-edge frequency for the receiver.

$$R_{xy} = \frac{1}{2\pi} [e^{i(\Delta\omega_0 t + \theta + \omega_0 \tau)}] \int_{-\omega_1}^{-\omega_0} Z(\omega') Z^*(\omega') e^{i\omega'(\tau - \tau')} d\omega' \\ + \frac{1}{2\pi} [e^{-i(\Delta\omega_0 t + \theta + \omega_0 \tau)}] \int_{\omega_0}^{\omega_1} Z(\omega') Z^*(\omega') e^{i\omega'(\tau - \tau')} d\omega' ,$$

(A-42)

where

$\underbrace{\theta = \phi_x - \phi_y}_{\text{Local oscillator phase difference at } \tau = 0}$	$\underbrace{+\Delta\omega_0 (\tau_{s1} + \tau_{s2})/2}_{\text{Average source-spacecraft propagation time}}$	$\underbrace{-\omega_0 (\tau_{g1} - \tau_{g2})}_{\text{Spacecraft-ground station propagation time difference}}$
---	--	---

and

$$\tau' = \underbrace{\tau_{s1} + \tau_{g1} - \tau_{s2} - \tau_{g2}}_{\text{Total propagation time difference}} ,$$

$\Delta\omega_0 \equiv$ frequency difference between receiver local oscillators
(radians/sec),

$\omega_0 \equiv$ average local oscillator frequency (radians/sec),

$\tau \equiv$ delay (sec), and

$t \equiv$ time (sec).

B. Cross-Correlation Function for a White-Noise Power Spectra

We will now compute the cross-correlation function for a rectangular filtered 'white-noise' power spectra with a center frequency ω_c , within the passband of the receiver.

For a rectangular filtered 'white-noise' power spectra, normalized so that $\int_{-\infty}^{\infty} Z(\omega)Z^*(\omega)d\omega = 2\pi$,

$$Z(\omega)Z^*(\omega) = \begin{cases} \pi/\Delta\omega & \text{for } \omega_c - \Delta\omega/2 < |\omega| < \omega_c + \Delta\omega/2 \\ 0 & \text{otherwise} \end{cases} \quad (A-43)$$

Substituting equation (A-43) into equation (A-42) gives the cross-correlation function:

$$\begin{aligned} R_{xy} = & \frac{1}{2\Delta\omega} [e^{i(\Delta\omega_0 t + \theta + \omega_0 \tau)}] \int_{-\omega_c - \Delta\omega/2}^{-\omega_c + \Delta\omega/2} e^{i\omega'(\tau - \tau')} d\omega' \\ & + \frac{1}{2\Delta\omega} [e^{-i(\Delta\omega_0 t + \theta + \omega_0 \tau)}] \int_{\omega_c - \Delta\omega/2}^{\omega_c + \Delta\omega/2} e^{i\omega'(\tau - \tau')} d\omega' \quad (A-44) \end{aligned}$$

$$\begin{aligned}
R_{xy} = & \frac{1}{2} \left\{ e^{-i[\Delta\omega_0 t + \theta + \omega_0 \tau - \omega_c(\tau - \tau')]} \right\} \frac{\sin\left[\frac{\Delta\omega}{2}(\tau - \tau')\right]}{\frac{\Delta\omega}{2}(\tau - \tau')} \\
& + \frac{1}{2} \left\{ e^{i[\Delta\omega_0 t + \theta + \omega_0 \tau - \omega_c(\tau - \tau')]} \right\} \frac{\sin\left[\frac{\Delta\omega}{2}(\tau - \tau')\right]}{\frac{\Delta\omega}{2}(\tau - \tau')} \quad (A-45)
\end{aligned}$$

$$R_{xy} = \cos[\Delta\omega_0 t + \theta + \omega_0 \tau - \omega_c(\tau - \tau')] \frac{\sin\left[\frac{\Delta\omega}{2}(\tau - \tau')\right]}{\frac{\Delta\omega}{2}(\tau - \tau')} \quad (A-46)$$

C. Cross-Correlation Function for a Gaussian-Shaped Power Spectra

We will now compute the cross-correlation function for a Gaussian-shaped power spectra with a center frequency ω_c , within the passband of the receiver.

For a Gaussian-shaped power spectra, normalized so that

$$\int_{-\infty}^{\infty} Z(\omega) Z^*(\omega) d\omega = 2\pi,$$

$$Z(\omega) Z^*(\omega) = \frac{\pi}{\Delta\omega} \left[e^{-\pi(\omega - \omega_c)^2 / \Delta\omega^2} + e^{-\pi(\omega + \omega_c)^2 / \Delta\omega^2} \right] \quad (A-47)$$

Substituting equation (A-47) into equation (A-42) gives the cross-correlation function:

$$\begin{aligned}
R_{xy} = & \frac{1}{2\Delta\omega} [e^{i(\Delta\omega_0 t + \theta + \omega_0 \tau)}] \int_{-\omega_1}^{-\omega_0} [e^{-\pi(\omega' - \omega_c)^2 / \Delta\omega^2} \\
& + e^{-\pi(\omega' + \omega_c)^2 / \Delta\omega^2}] e^{i\omega'(\tau - \tau')} d\omega' + \frac{1}{2\Delta\omega} [e^{-i(\Delta\omega_0 t + \theta + \omega_0 \tau)}] \\
& \times \int_{\omega_0}^{\omega_1} [e^{-\pi(\omega' - \omega_c)^2 / \Delta\omega^2} + e^{-\pi(\omega' + \omega_c)^2 / \Delta\omega^2}] e^{i\omega'(\tau - \tau')} d\omega' \quad .
\end{aligned}$$

(A-48)

For a Gaussian-shaped power spectra with a bandwidth that is narrow compared to the bandwidth of the receiver the cross-correlation function can be approximated by integrating from $-\infty$ to $+\infty$.

$$\begin{aligned}
R_{xy} \approx & \frac{1}{2\Delta\omega} [e^{i(\Delta\omega_0 t + \theta + \omega_0 \tau)}] \int_{-\infty}^{\infty} e^{-\pi(\omega' + \omega_c)^2 / \Delta\omega^2} e^{i\omega'(\tau - \tau')} d\omega' \\
& + \frac{1}{2\Delta\omega} [e^{-i(\Delta\omega_0 t + \theta + \omega_0 \tau)}] \int_{-\infty}^{\infty} e^{-\pi(\omega' - \omega_c)^2 / \Delta\omega^2} e^{i\omega'(\tau - \tau')} d\omega'
\end{aligned}$$

(A-49)

$$\begin{aligned}
R_{xy} \approx & \frac{1}{2} \{ e^{i[\Delta\omega_0 t + \theta + \omega_0 \tau - \omega_c(\tau - \tau')]} e^{-\Delta\omega^2(\tau - \tau')^2 / 4\pi} \\
& + e^{-i[\Delta\omega_0 t + \theta + \omega_0 \tau - \omega_c(\tau - \tau')]} e^{-\Delta\omega^2(\tau - \tau')^2 / 4\pi} \}
\end{aligned}$$

(A-50)

$$R_{xy} = \cos[\Delta\omega_0 t + \theta + \omega_0 \tau - \omega_c(\tau - \tau')] \\ \times e^{-\Delta\omega^2(\tau - \tau')^2/4\pi} \quad . \quad (A-51)$$

APPENDIX B

DERIVATION OF AN INTERFEROMETER'S RESPONSE
TO AN EXTENDED SOURCE

This derivation of an interferometer's response to an incoherent extended source follows the derivation of Tyler [1966] but uses the geometry pertinent to satellite-satellite interferometry. For this derivation, the exact details of the receiver's operation are neglected. (See Appendix A for an analysis of the receiver-correlator response to a wide bandwidth signal from a point source.) The quadrature outputs of the receiver-correlator are modeled as a phase shift, multiplication, and low pass filtering of the radio signals detected by each spacecraft. The baseline length is assumed to be very much shorter than the distance to the source, the source is assumed to be small (i.e., smaller than the angular beamwidth of the individual antennas), and the brightness distribution is assumed to go to zero away from the center of the source. The brightness of the source is normalized so that the integral of the brightness distribution over all space is equal to 1.

A. Definition of Coordinate System and Parameters

Consider an arbitrary orthogonal coordinate system (x', y', z') centered on the midpoint of the ISEE-1 and -2 baseline, as shown in Figure B-1. The r , θ , and ϕ components are the normal spherical polar coordinates, with distances measured in wavelengths. The parameters and vectors used to define the baseline and source location in the (x', y', z') coordinate system are:

D/λ	Length of baseline (wavelengths)
$\vec{b} = (\frac{1}{2} D/\lambda, \theta_b, \phi_b)$	Length and direction of baseline vector
$\hat{b} = (1, \theta_b, \phi_b)$	Baseline unit vector
$\vec{s}_0 = (s_0, \theta_0, \phi_0)$	Distance and direction to center of source location
$\hat{s}_0 = (1, \theta_0, \phi_0)$	Unit vector pointing to center of source
$\vec{s} = (s, \theta, \phi)$	Distance and direction of arbitrary vector extending to point s
$\hat{s} = (1, \theta, \phi)$	Unit vector in direction of \vec{s}
δ	Angle between \hat{b} and \vec{s}
δ_0	Angle between \hat{b} and \vec{s}_0

The orthogonal source centered coordinate system (x, y, z) is chosen so that: (1) its origin is at the center of the source region, (2) its z axis is in the same direction as \vec{s}_0 , and (3) the dot product of \hat{x} and \hat{z}' is zero (i.e., \hat{x} has no \hat{z}' component). The

brightness distribution, in source-centered coordinates, has coordinates measured as angular positions, relative to the origin of the baseline-centered coordinate system. The parameters used to define the baseline and brightness distribution relative to the source centered coordinate system are:

$x = (\phi_0 - \phi) \sin \theta$ Source-centered coordinate (radians)

$y = (\theta_0 - \theta)$ Source-centered coordinate (radians)

$S(x,y)$ Two-dimensional brightness distribution
in source-centered coordinates

$$(\iint S(x,y) dx dy = 1)$$

u Projection of the baseline in the
 \hat{x} direction (wavelengths)

v Projection of the baseline in the
 \hat{y} direction (wavelengths)

w Projection of the baseline in the
 \hat{z} direction (wavelengths)

The correlator has two quadrature phase outputs, C_0 and C_{90} . The C_0 output is the correlation of the ISEE-1 signal with the ISEE-2 signal. The C_{90} output is the correlation of the ISEE-1 signal with the 90° phase-shifted ISEE-2 signal.

B. Source Relative Baseline Projections

The response of an interferometer to a two-dimensional brightness distribution is dependent upon the projections of the baseline relative to a the source-centered coordinate system. The baseline projections are computed by taking a vector dot product of the baseline unit vector \hat{b} with unit vectors in the source-centered coordinate system (\hat{x} , \hat{y} , and \hat{z}) and multiplying by the length of the baseline.

From the geometry shown in Figure B-1, the direction to the center of the source location is:

$$\hat{s}_0 = \sin \theta_0 (\cos \phi_0 \hat{x}' + \sin \phi_0 \hat{y}') + \cos \theta_0 \hat{z}' \quad , \quad (B-1)$$

the unit vectors of the source-centered coordinate system are:

$$\hat{x} = \sin \phi_0 \hat{x}' - \cos \phi_0 \hat{y}' \quad (B-2)$$

$$\hat{y} = -\cos \theta_0 (\cos \phi_0 \hat{x}' + \sin \phi_0 \hat{y}') + \sin \theta_0 \hat{z}' \quad (B-3)$$

$$\hat{z} = \sin \theta_0 (\cos \phi_0 \hat{x}' + \sin \phi_0 \hat{y}') + \cos \theta_0 \hat{z}' \quad , \quad (B-4)$$

and the baseline unit vector is:

$$\hat{b} = (\sin \theta_b (\cos \phi_b \hat{x}' + \sin \phi_b \hat{y}') + \cos \theta_b \hat{z}') \quad . \quad (B-5)$$

The baseline projections are:

$$u = D/\lambda \hat{x} \cdot \hat{b} = D/\lambda \sin \theta_b \sin(\phi_0 - \phi_b) \quad (B-6)$$

$$\begin{aligned} v &= D/\lambda \hat{y} \cdot \hat{b} \\ &= D/\lambda (-\cos \theta_0 \sin \theta_b \cos(\phi_0 - \phi_b) + \sin \theta_0 \cos \theta_b) \end{aligned} \quad (B-7)$$

$$\begin{aligned} w &= D/\lambda \hat{z} \cdot \hat{b} \\ &= D/\lambda (\sin \theta_0 \sin \theta_b \cos(\phi_0 - \phi_b) + \cos \theta_0 \cos \theta_b) \end{aligned} \quad , \quad (B-8)$$

where u , v , and w are the baseline projections in the \hat{x} , \hat{y} , and \hat{z} directions, respectively.

We can compute the angle between the baseline and an arbitrary source element $S(x,y)$ by taking the vector dot product of the baseline unit vector \hat{b} and a unit vector \hat{s} (with components $1, \theta, \phi$) pointing toward the source element.

Thus,

$$\cos(\delta) = \sin \theta \sin \theta_b \cos(\phi - \phi_b) + \cos \theta \cos \theta_b \quad , \quad (B-9)$$

where δ is the angle between \hat{b} and \hat{s} . By examining equation (B-9) and equations (B-6) through (B-8), we see that the baseline projections can also be written as:

$$u = - D/\lambda \left[\frac{1}{\sin \theta} \frac{\partial(\cos \delta)}{\partial \phi} \right] \Big|_{\phi_0, \theta_0} \quad (\text{B-10})$$

$$v = - D/\lambda \left[\frac{\partial(\cos \delta)}{\partial \theta} \right] \Big|_{\phi_0, \theta_0} \quad (\text{B-11})$$

$$w = D/\lambda (\cos \delta) \Big|_{\phi_0, \theta_0} = D/\lambda \cos \delta_0 \quad . \quad (\text{B-12})$$

C. Response of an Interferometer to a Point Source

We want to determine the response of the interferometer to a point source of flux density $S(x,y) = \delta(x - x_0)\delta(y - y_0)$ with position coordinates (s, θ, ϕ) . The normalized outputs from each receiver (assumes a gain of $\sqrt{2}$ for each antenna-receiver combination) are:

$$E_1 = \sqrt{2} \sin\left(\omega t - \frac{\pi D}{\lambda} \cos \delta\right) \quad \text{for ISEE-1} \quad (\text{B-13})$$

and

$$E_2 = \sqrt{2} \sin\left(\omega t + \frac{\pi D}{\lambda} \cos \delta\right) \quad \text{for ISEE-2} \quad . \quad (\text{B-14})$$

The phase-shifted ISEE-2 receiver output is:

$$E_{2_{L\pi/2}} = \sqrt{2} \cos\left(\omega t + \frac{\pi D}{\lambda} \cos \delta\right) , \quad (\text{B-15})$$

where δ is the angle between the baseline unit vector and the vector \vec{s} , which points toward the source.

The output of the multiplier, $C_0'(\delta)$, is therefore

$$C_0'(\delta) = E_1 E_2 = \left[\cos\left(\frac{2\pi D}{\lambda} \cos \delta\right) - \cos(2\omega t) \right] . \quad (\text{B-16})$$

The low-pass filter rejects the higher frequency term, giving the output of the correlator:

$$C_0(\delta) = \cos\left(\frac{2\pi D}{\lambda} \cos \delta\right) \quad (\text{B-17})$$

and in a similar fashion

$$C_{90}(\delta) = -\sin\left(\frac{2\pi D}{\lambda} \cos \delta\right) . \quad (\text{B-18})$$

D. Response of an Interferometer to an Extended Source

To determine the response of an interferometer for an extended source region, we must integrate equations (B-17) and (B-18) over the extended source. Consider the elemental solid angle

$d\Omega = \sin \theta d\theta d\phi = dx dy$ located at (θ, ϕ) or (x, y) , having brightness $S(x, y)$. From equation (B-17), the response of the interferometer due to this small portion of the source is:

$$d^2 C_0(x, y, u, v, w) = S(x, y) \cos\left(\frac{2\pi D}{\lambda} \cos \delta\right) dx dy \quad . \quad (B-19)$$

By expanding $\cos(\delta)$ in a Taylor series about the origin of the source-centered coordinate system and keeping only the first-order terms, we get an expression for $\cos(\delta)$ in terms of the source-centered coordinates, x and y .

$$\begin{aligned} \cos \delta \sim & \sin \theta_0 \sin \theta_b \cos(\phi_0 - \phi_b) + \cos \theta_0 \cos \theta_b \\ & + (\phi - \phi_0) \left. \frac{\partial(\cos \delta)}{\partial \phi} \right|_{\theta_0, \phi_0} + (\theta - \theta_0) \left. \frac{\partial(\cos \delta)}{\partial \theta} \right|_{\theta_0, \phi_0} + \dots \end{aligned} \quad (B-20)$$

$$\cos \delta \sim \cos \delta_0 - x \frac{1}{\sin \theta_0} \left. \frac{\partial(\cos \delta)}{\partial \phi} \right|_{\theta_0, \phi_0} - y \left. \frac{\partial(\cos \delta)}{\partial \theta} \right|_{\theta_0, \phi_0} \quad . \quad (B-21)$$

Substituting the expressions for the baseline projections [equations (B-10), (B-11), and (B-12)] into (B-21), we get:

$$\cos \delta \sim \lambda/D(ux + vy + w) \quad . \quad (B-22)$$

Substituting equation (B-22) into equation (B-19) gives:

$$\begin{aligned} d^2 C_0(x, y, u, v, w) &= S(x, y) \cos[2\pi(ux + vy + w)] dx dy \\ &= S(x, y) \{ \cos(2\pi w) \cos[2\pi(ux + vy)] \end{aligned} \quad (B-23)$$

$$- \sin(2\pi w) \sin[2\pi(ux + vy)] \} dx dy \quad . \quad (B-24)$$

Integrating over the entire source region gives:

$$\begin{aligned} C_0(u, v, w) &= \cos 2\pi w \iint S(x, y) \cos[2\pi(ux + vy)] dx dy \\ &\quad - \sin 2\pi w \iint S(x, y) \sin[2\pi(ux + vy)] dx dy \end{aligned} \quad (B-25)$$

$$C_0(u, v, w) = \cos 2\pi w C(u, v) - \sin 2\pi w S(u, v) \quad , \quad (B-26)$$

where

$$C(u, v) = \iint S(x, y) \cos[2\pi(ux + vy)] dx dy \quad (B-27)$$

$$S(u, v) = \iint S(x, y) \sin[2\pi(ux + vy)] dx dy \quad . \quad (B-28)$$

In a similar fashion the quadrature output $C_{90}(u, v, w)$ can be shown to be:

$$C_{90}(u, v, w) = - \sin 2\pi w C(u, v) - \cos 2\pi w S(u, v) \quad . \quad (B-29)$$

We can define the complex visibility v of the interference pattern as:

$$v(x,y) = e^{i2\pi w} (C_0 + iC_{90}) \quad . \quad (B-30)$$

The $e^{i2\pi w}$ factor compensates for the different source-spacecraft signal propagation time for each spacecraft.

$$\begin{aligned} v(x,y) = e^{i2\pi w} [(\cos 2\pi w - i \sin 2\pi w)C(u,v) \\ - i(\cos 2\pi w - i \sin 2\pi w)S(u,v)] \end{aligned} \quad (B-31)$$

$$v(x,y) = e^{i2\pi w} e^{-i2\pi w} [C(u,v) - i S(u,v)] \quad (B-32)$$

$$v(x,y) = [C(u,v) - i S(u,v)] \quad (B-33)$$

$$v(x,y) = V(u,v)e^{-i\phi(u,v)} \quad , \quad (B-34)$$

where

$$V(u,v) = [C^2(u,v) + S^2(u,v)]^{1/2} \quad (B-35)$$

and

$$\Phi = -\tan^{-1}\left[\frac{S(u,v)}{C(u,v)}\right] . \quad (B-36)$$

$V(u,v)$ represents the magnitude of the complex correlation and Φ is the phase of the complex correlation.

Upon substituting equations (B-27) and (B-28) into equation (B-33), we get:

$$\begin{aligned} v(u,v) &= \iint S(x,y) \cos[2\pi(ux+vy)] dx dy + i \iint S(x,y) \sin[2\pi(ux+vy)] dx dy \\ &= \iint S(x,y) e^{-i2\pi(ux+vy)} dx dy . \end{aligned} \quad (B-37)$$

By having the brightness distribution go to zero at a small distance from the center of the source region, we can extend the limits of integration to plus and minus infinity, with the right-hand side of equation (B-37) becoming the normalized Fourier transform of the brightness distribution. Therefore,

$$S(x,y) = \iint v(x,y) e^{i2\pi(ux+vy)} du dv . \quad (B-38)$$

Thus, if it is possible to measure the amplitude and phase of the visibility over all u and v , we can compute the brightness distribution by taking the inverse Fourier transform of the complex visibility.

In practice, the complex visibility is measured at discrete values of u and v . The necessary sample spacing in the u - v plane is determined by the angular size of the brightness distribution. For a brightness distribution with maximum dimensions of X by Y radians, the necessary sample spacings (in wavelengths) Δu and Δv are:

$$\Delta u < \frac{1}{2X} \quad (\text{B-39})$$

and

$$\Delta v < \frac{1}{2Y} \quad (\text{B-40})$$

[Tyler, 1966].

The desired resolution of the radio map determines the maximum baseline required. For a resolution of Δx by Δy radians, the visibility needs to be sampled only up to the maximum baselines U and V are given by:

$$U < \frac{1}{2\Delta x} \quad (\text{B-41})$$

and

$$V < \frac{1}{2\Delta y} \quad (\text{B-42})$$

[Tyler, 1966].

Figure B-1. This figure shows the source-baseline geometry, relative to a coordinate system moving with the spacecraft (primed system), and the coordinate system associated with the source region (unprimed system).

C-684-199-1

SOURCE-BASELINE GEOMETRY

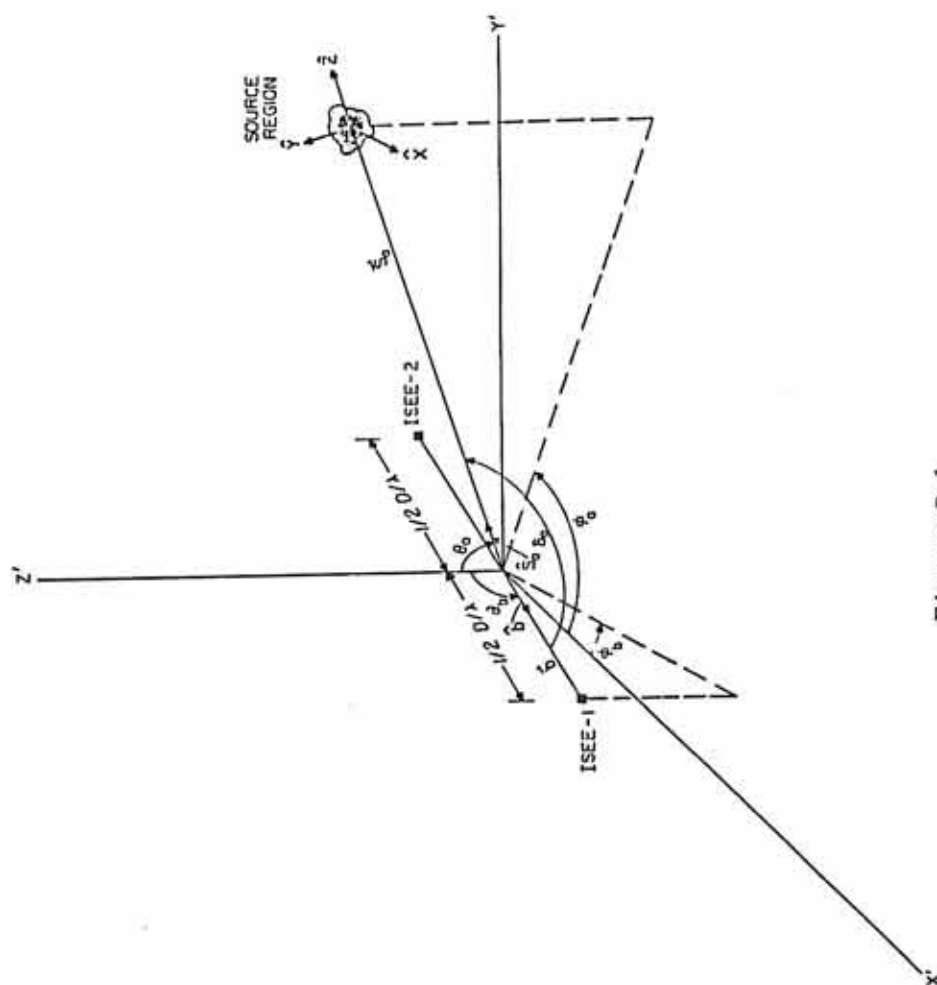


Figure B-1

APPENDIX C

RAY-TRACING RESULTS

A ray-tracing analysis was performed to determine the effects that different source region locations have upon the measured source region size, the wave propagation times, and the projected baseline. The ray-tracing analysis was performed for waves which propagate directly to the spacecraft and for waves which reflect from the plasmopause. For direct source-spacecraft propagation paths, the source region location affects: (1) the angular width of the source region, as viewed from the spacecraft, (2) the projected baseline, (3) the propagation time for the waves to reach the spacecraft, and (4) the emission angle, with respect to the local magnetic field in the source region, of the waves detected by the spacecraft. For waves reflecting from the plasmopause, the different source region locations and L-values of the plasmopause affect, in addition to the four parameters for direct propagation paths: (1) the shape and orientation of the resulting source region image, relative to the projected baseline, and (2) the size and location of the solid angle of amplified galactic background radiation detected by the spacecraft.

A. The Ray-Tracing Program

1. The Source Region

For the ray-tracing analysis, the source region is assumed to be spherical with a radius of $0.02 R_E$ (127.56 km). Since the source region can be located at any position within the auroral region, calculations were performed for source regions with positions along magnetic field lines between 65° and 75° Mlat and between 18.0 and 6.0 hrs MLT. The altitude of the source region was chosen to be the altitude where the local gyrofrequency is 250 kHz.

2. The Spacecraft Positions

The spacecraft positions used in the analysis are the approximate positions of ISEE-1 and -2 on February 20, 1979 between 0030 and 0050 UT, and between 0300 and 0320 UT. These times correspond to the measurements made at the two longest baselines. The actual spacecraft positions used in the ray-tracing analysis are listed in Table C-1.

3. The Reflecting Surface

Measurements of the polarization of AKR have found that AKR is predominantly R-X mode radiation [Kaiser et al., 1978; Mellott et al., 1984]. Free space R-X mode radiation has a lower frequency cutoff of:

$$\omega = \frac{|\omega_{ce}|}{2} + \sqrt{\left(\frac{\omega_{ce}}{2}\right)^2 + \omega_{pe}^2} \quad , \quad (C-1)$$

where ω_{ce} is the electron gyrofrequency and ω_{pe} is the electron plasma frequency [Stix, 1962]. The index of refraction for right-hand polarized waves (wave propagation parallel to the local magnetic field) is [Stix, 1962]:

$$n^2 = 1 - \frac{\omega_{pe}^2}{\omega(\omega + |\omega_{ce}|)} \quad , \quad (C-2)$$

and the index of refraction for extraordinary mode waves (wave propagation perpendicular to the local magnetic field) is [Stix 1962]:

$$n^2 = 1 - \frac{\omega_{pe}^2}{\omega^2} \left(\frac{\omega^2 - \omega_{pe}^2}{\omega^2 - \omega_{ce}^2 - \omega_{pe}^2} \right) \quad . \quad (C-3)$$

Within the magnetosphere, the plasmopause can be a suitable surface for kilometric waves to reflect from. The plasmopause is the boundary between the plasmasphere and the outer magnetosphere. Inside the plasmopause there is a cool dense plasma, and outside the plasmopause there is a much more dilute and hotter plasma. At the plasmopause, the density changes abruptly from several hundred particles per cm^{-3} on the inside to approximately 10 cm^{-3} on the outside. Within the plasmopause, the density is nearly constant along magnetic field lines, and proportional to L^{-m} , where m is between 3.0 and 4.0 [Carpenter et al., 1981; R. Anderson, personal communication, 1986]. The plasmopause is typically found between L-values of 3.0 and 5.0.

The shape of the plasmopause is not symmetric in magnetic local time, but contains a bulge at approximately 18.0 hrs MLT [Carpenter, 1966]. During magnetically active times, the plasmopause contracts and during magnetically quiet times the plasmopause expands [Block, 1973].

Figure C-1 shows the geometry of the plasmopause, the source region, and the R-X mode cutoff surface. In Figure C-1, the plasmopause is assumed to be located at an L-value of 3.75, the density outside the plasmopause is assumed to be 10 cm^{-3} , and the density inside the plasmopause is assumed to be:

$$n_e = 2.5 \times 10^4 L^{-3} . \quad (\text{C-4})$$

Equation (C-4) predicts a density of 475 cm^{-3} at an L-value of 3.75. The density predicted by equation (C-4) represents the median density deduced from over 150 ISEE-1 plasmopause crossings, with L-values between 2.0 and 5.0 and radial distances between 2.0 and 3.5 R_E . From Figure C-1, in the region where the ray-tracing analysis predicts the reflections should occur, the R-X mode cutoff closely follows the plasmopause. When there is a steep density gradient at the plasmopause, the index of refraction can go from zero at the plasmopause to nearly one just outside of the plasmopause. In the region where the ray-tracing analysis predicts the reflections should occur, the gyrofrequency is approximately 100 kHz and the plasma frequency, outside of the plasmopause, is approximately 28 kHz. From equation (C-2), the index of refraction for right-hand polarized waves propagating

outside of the plasmopause is 0.989, and from equation (C-3), the index of refraction for extraordinary mode waves propagating outside of the plasmopause is 0.992. Since the waves are not propagating exactly perpendicular or parallel to the magnetic field, the actual index of refraction for the waves is between the values of the index of refraction for right-hand polarized waves and the index of refraction for extraordinary mode waves. With a steep gradient in the density, most of the refraction takes place very close to the plasmopause, and can be approximated as a total reflection at the plasmopause. The ray-tracing program assumes that the waves are totally reflected at the plasmopause.

4. The Computed Parameters

For waves which propagate directly to the spacecraft, the ray-tracing program computes the angular width of the source region, the difference between the source-spacecraft propagation times, the projected baseline, and the wave-normal angle (at the source region) of the waves detected by the spacecraft. For waves which reflect from the plasmopause, the ray-tracing program computes the size and shape of the solid angle of amplified galactic background radiation detected by the spacecraft, the size and shape of the source region image, the difference between the source-spacecraft propagation times, the projected baseline, the angle between the projected baseline and the major axis of the source region image, and the wave-normal direction (at the source region) of the waves detected by the spacecraft. The angular widths and projected baselines are used to compute the

source region diameter. The propagation time difference can be used to estimate the approximate source region location. The wave-normal angles, for directly propagating waves and reflected waves, can be compared to the theoretical wave-normal angles for consistency.

B. The Apparent Source Size

The correlation, as a function of angular width and projected baseline, for a source region with a circularly symmetric Gaussian brightness distribution [equation (24)] is:

$$\rho = e^{-(\pi b \alpha / 2)^2} , \quad (C-5)$$

where b is the projected baseline in wavelengths and α is the angular source region width. The angular source region width, as a function of the source diameter d , and source-spacecraft distance R_{SS} , is:

$$\alpha = 2 \tan^{-1}(d/2R_{SS}) . \quad (C-6)$$

For source diameters which are small compared to the source-spacecraft distance, equation (C-6) can be approximated as:

$$\alpha = d/R_{SS} . \quad (C-7)$$

Substituting equation (C-7) into equation (C-5) gives the correlation as a function of projected baseline, source diameter, and source-spacecraft distance:

$$\rho = e^{-(\pi b d / 2 R_{ss})^2} . \quad (C-8)$$

Solving equation (C-8) for the source diameter, as a function of correlation, projected baseline, and source-spacecraft distance gives:

$$d = \frac{2}{\pi b} R_{ss} \sqrt{-\ln \rho} . \quad (C-9)$$

From equation (C-9), the source diameter is proportional to R_{ss}/b , when the correlation is held fixed. Thus, only the source-spacecraft distance and the projected baseline affect the measured source diameter, for waves propagating directly to the spacecraft.

For waves which reflect from the plasmopause, the shape and size of the source region image is a complicated function of the shape and position of the reflecting surface. For source region or image brightness distributions which are not circularly symmetric, the two-dimensional visibility can be found by taking the Fourier transform of the brightness distribution [equation (B-37)]. A two-dimensional Gaussian brightness distribution of an elliptically shaped source region has the form:

$$S(x,y) = \frac{4}{\pi \alpha_1 \alpha_2} e^{-[(2x/\alpha_1)^2 + (2y/\alpha_2)^2]} , \quad (C-10)$$

where α_1 is the angular width of the major axis and α_2 is the angular width of the minor axis of the source region. Substituting equation (C-10) into equation (B-37) and integrating gives the visibility of an elliptically shaped source region:

$$v(u,v) = e^{-[\pi^2(u^2\alpha_1^2 + v^2\alpha_2^2)/4]} \quad , \quad (C-11)$$

where u and v are the components of the projected baseline. The baseline projections can be transformed into circular coordinates with the equations:

$$\begin{aligned} u &= b \cos \theta \\ v &= b \sin \theta \quad , \end{aligned} \quad (C-12)$$

where b is the magnitude of the projected baseline and θ is the angle between the major axis of the elliptically shaped source region and the projected baseline. Substituting equation (C-12) into equation (C-11) gives the visibility of an elliptically shaped source region with a Gaussian brightness distribution:

$$v = e^{-[\pi^2 b^2 (\alpha_1^2 \cos^2 \theta + \alpha_2^2 \sin^2 \theta)/4]} \quad . \quad (C-13)$$

From equation (C-13), the visibility is a function of the projected baseline, the size and eccentricity of the elliptically shaped source

region, and the angle between the projected baseline and the major axis of the elliptically shaped source region. Comparison of equations (C-5) and (C-13), gives the effective angular width, α_e , of an elliptically shaped source region as:

$$\alpha_e = \alpha_1^2 \cos^2 \theta + \alpha_2^2 \sin^2 \theta \quad . \quad (C-14)$$

From equation (C-14), if the angle between the major axis of the source region image and the projected baseline is 0° , interferometry will measure the angular width of the major axis of the source region image, and if the angle between the major axis of the source region image and the projected baseline is 90° , interferometry will measure the angular width of the minor axis of the source region image.

C. The Ray-Tracing Results

1. Signal Propagation Times

An estimate of the true source position can be obtained by comparing the predicted signal propagation time difference with the actual delay which maximizes the correlation. If the actual signal propagation time differences were known, it would be possible to determine a surface on which the source region must be located. The uncertainty in the propagation time differences can be estimated by examining the ways in which the signals can be delayed in the telemetry link and recording process. Manufacturing tolerances for the type of tape recorders used for recording and playback of data

are: (1) head separation is $1.5 \pm .001$ in and (2) gap scatter is ± 100 μ inch [Willard Zoerner, Sangamo/Weston, personal communication, 1986]. Thus, tape recorder head alignment could cause a maximum time offset of 146.6 μ sec between the two data channels, at a recording speed of 15 in sec^{-1} . For data recorded during spacecraft calibration, a -87 μ sec time offset was found between the calibration signals from each spacecraft. In addition to an offset caused by tape recorder head alignment, there is an additional signal delay in the ground station telemetry equipment. Measurements of the telemetry equipment at NASA ground stations put an upper limit on the site delay of ± 50 μ sec [Jim Braun, NASA, personal communication, 1986]. The combination of tape recorder head alignment and site delay produces an upper limit for the total time offset of ± 200 μ sec.

Figure C-2 is a plot of the propagation time difference, as a function of magnetic local time, predicted for a direct propagation path to the spacecraft. The spacecraft positions used to compute the data in Figure C-2 are the approximate positions of the spacecraft on February 20, 1979 between 0030 and 0050 UT. From Figure C-2, it can be seen that for source regions in the local evening, along magnetic-field lines between 65° and 75° magnetic latitude, the signal propagation time difference changes by less than 50 μ sec for a 5° change in magnetic latitude of the source region field line. For source regions near 6.0 hrs MLT, the signal propagation time difference changes by 300 μ sec for a 5° change in magnetic latitude of the source region field line. For waves propagating directly to the spacecraft, the

signal propagation time difference can decrease by as much as 2 msec as the source location is moved from 18.0 hrs to 6.0 hrs MLT. For a source region along a 70° Mlat field line at 21.0 hrs MLT, the predicted signal propagation time difference is -35.8 msec. The propagation time difference, for the data received on February 20, 1979 between 0030 and 0050 UT, which maximized the correlation, was 520 ± 200 μ sec less than the predicted propagation time difference for a source location along a 70° Mlat field line at 21.0 hrs MLT. The actual propagation time difference corresponds to source region locations in the range from 22.75 to 2.25 hrs MLT.

Figure C-3 is a plot of the propagation time differences, as a function of magnetic local time, predicted for waves which reflect from the plasmopause. The spacecraft positions used to compute the data in Figure C-3 are also the approximate positions of the spacecraft on February 20, 1979 between 0030 and 0050 UT. From Figure C-3 it can be seen that for source regions in the local evening, along magnetic-field lines between 65° and 75° magnetic latitude, the signal propagation time difference can change by as much as 1.0 msec for a 5° change in magnetic latitude of the source region field line. For source regions near 6.0 hrs MLT, the signal propagation time difference changes by 250 μ sec for a 5° change in magnetic latitude of the source region field line. For waves reflecting from the plasmopause, the signal propagation time difference can decrease by as much as 4.2 msec as the source region location is moved from 18.0 hrs to 6.0 hrs MLT. The propagation time difference for waves reflecting from the

plasmopause is up to 3.3 msec longer for source regions located at 18.0 hrs MLT and 1.7 msec longer for source regions located at 6.0 hrs MLT, than for waves propagating directly to the spacecraft. For reflected waves, a source-spacecraft propagation difference of -35.3 ± 0.2 msec is consistent with source regions located at positions from 3.0 to 6.0 hrs MLT.

2. The Projected Baseline

The projected baseline is dependent upon the exact positions of both spacecraft and the location of the source region, or the source region image for waves reflecting from the plasmopause. Figure C-4 is a plot of the projected baseline, for waves propagating directly to the spacecraft and for waves reflecting from the plasmopause, as a function of magnetic local time, for source region locations along 65° , 70° and 75° magnetic-field lines. The spacecraft positions used in the calculations for Figures C-4 and C-5 are the approximate positions for the correlations measured on February 20, 1979 between 0030 and 0050 UT.

For waves propagating directly to the spacecraft, the minimum projected baselines occur near 18.5 hrs MLT with values between 3495 and 3546 km, and the maximum projected baselines occur near 6.0 hrs MLT with values between 4456 and 4860 km. The source regions located along lower magnetic latitude field lines have larger projected baselines at 6.0 hrs MLT than do the source regions located along higher magnetic latitude field lines. For source regions located at 21.0 hrs

MLT, the projected baselines are in the range of 3611 to 3635 km and for source region locations between 22.75 and 2.25 hrs MLT, the projected baselines are in the range of 3777 to 4467 km.

From Figure C-4, the minimum projected baselines, for waves reflecting from the plasmopause, occur near 19.75 hrs MLT with values between 3874 and 4182 km, and the maximum projected baselines occur near 6.0 hrs MLT with values between 4940 and 5092 km. The projected baseline for source regions located on lower magnetic latitude field lines varies over a larger range of values than the projected baseline for source regions located on higher magnetic latitude field lines. For source locations at 21.0 hrs MLT, the projected baselines are in the range of 3911 to 4205 km, and for source locations between 3.0 and 6.0 hrs MLT the projected baselines are in the range of 4729 to 5092 km.

Figure C-5 shows the projected baseline as a function of magnetic local time, for waves reflecting at different plasmopause L-values. For source locations at a fixed magnetic local time, waves reflecting from lower L-values have a larger projected baseline. For source locations between 18.0 and 6.0 hrs MLT, an increase in the L-value of the reflecting surface by 0.25 decreases the projected baseline by approximately 50 km.

Figures C-4 and C-5 also show that the projected baseline for waves reflecting from the plasmopause is greater than the projected baseline for waves propagating directly to the spacecraft. For source regions along 75° Mlat field lines, the difference between the

projected baselines for waves reflecting from the plasmopause and for waves propagating directly to the spacecraft can be as large as 672 km at 18.0 hrs MLT. For source regions along 65° Mlat field lines, the difference between the projected baselines for waves reflecting from the plasmopause and for waves propagating directly to the spacecraft can be as small as 181 km near 2.5 hrs MLT.

3. Angular Source Region Shape

For waves which propagate directly to the spacecraft, the angular width of the source region is dependent upon the source region diameter and the source-spacecraft distance. For directly propagating waves, the shape of the source region image is not distorted by refraction. Source regions located near the magnetic local time of the spacecraft, and at low magnetic latitudes, will have the largest angular source width. The angular width of the source region, as a function of magnetic local time, varies by ± 6 percent for source regions along 65° Mlat field lines, and by ± 4 percent for source regions along 75° Mlat fields lines.

Since the plasmopause is a curved surface, the image of the source region is distorted when the waves reflect from the plasmopause. For small source region diameters, the shape of the source region image is approximately elliptical, and for large source region diameters, the source region image is shaped like a sausage. Figure C-6 is a plot of the angular magnification and orientation of the source region image, for a source region located along a 70° Mlat

field line at 21.0 hrs MLT with the wave reflecting from the plasma-pause at an L-value of 4.0. The position of the spacecraft, used in the computation of the source region image shape in Figure C-6, is the approximate position of ISEE-1 and -2 on February 20, 1979 between 0030 and 0050 UT. The angular width of the major axis of the elliptically shaped source region image is 1.066 times larger than the angular width of the source region, when viewed directly by the spacecraft, and the minor axis of the elliptically shaped source region image is 0.239 times smaller than the angular width of the source region, when viewed directly by the spacecraft. The solid angle extended by the source region image is 0.255 times smaller than the solid angle extended by the source region, when viewed directly by the spacecraft. For source region field lines located between 18.0 hrs and 6.0 hrs MLT, the eccentricity of the elliptically shaped source region varies from 0.95 to 0.99, depending upon the magnetic latitude of the source region magnetic-field line and the L-value of the reflecting surface.

4. Source Region Diameter

From equation (C-9), the diameter of the source region, when the correlation is held fixed and the waves propagate directly to the spacecraft, is proportional to the source-spacecraft distance divided by the baseline. Figure C-7 is a plot of the normalized source region diameter, as a function of magnetic local time, for source regions located on 65° to 75° Mlat field lines, when the waves propagate directly to the spacecraft and the correlation is held fixed. The

normalized source region diameters are relative to the diameter of a source region located along a 70° Mlat field line at 21.0 hrs MLT, with the waves propagating directly to the spacecraft. The normalized source region diameter, for source regions located along 65° Mlat field lines, varies from a maximum value of 1.10 at 18 hrs MLT to a minimum value of 0.73 at 4.5 hrs MLT. The normalized source region diameter varies over a wider range for source regions located at lower magnetic latitudes than for source regions located at higher magnetic latitudes. The change in projected baseline is the major cause of the variation of the source diameter, as a function of magnetic local time. For source regions located along magnetic field lines from 65° to 75° Mlat and between 22.75 and 2.25 hrs MLT, the source region diameter varies from 0.761 to 0.936 times smaller than the diameter of a source region located along a 70° Mlat field line at 21.0 hrs MLT with the same correlation.

For reflected ray paths, the normalized source region diameter is a complicated function of the ray path and the position of the spacecraft. From equation (C-13), the visibility (correlation) is dependent upon the projected baseline, the shape of the source region image, and the orientation of the source region image relative to the projected baseline. Figure C-8 is a plot of the normalized source region diameter, as a function of magnetic local time, for source regions located on 65° to 75° Mlat field lines, when the waves reflect from the plasmapause at an L-value of 4.0 and the correlation is held fixed. The normalized source region diameters are relative to the

diameter of a source region located along a 70° Mlat field line at 21.0 hrs MLT, with the waves propagating directly to the spacecraft.

From Figure C-8, there are two minimums in the normalized source region diameter as a function of magnetic local time, for source regions along 65° magnetic field lines. These two minimums can be explained by examining the projected baseline, the shape of the source region image, and the angle between the major axis of the source region image and the projected baseline, as a function of magnetic local time. From equation (C-14), the effective angular width of the source region image is large when the angle between the major axis of the source region image and the projected baseline is small. The angle between the major axis of the source region image and the projected baseline has a minimum value of 35.0° at 19.75 hrs MLT and a maximum value of 60.17° at 6.0 hrs MLT. The angular width of the major axis of the source region image reaches its maximum value at 19.25 hrs MLT, and the angular width of the minor axis of the source region image has a maximum at 20.75 hrs MLT. The combination of maximums in the angular width of the major and minor axes of the source region image and a minimum in the angle between the major axis of the source region image and the projected baseline, at nearly the same magnetic local time, produces a maximum in the effective angular width of the source region image. The maximum value of the effective angular width of the source region image is 0.956 at 19.5 hrs MLT. For a constant correlation and projected baseline, the normalized source diameter is inversely proportional to the effective angular

width of the source region image. Although the projected baseline has a minimum at 19.75 hrs MLT, the maximum in the effective angular width of the source region is large enough to produce a minimum in the normalized source region diameter of the source region at 19.75 hrs MLT. For source regions along 70° and 75° Mlat field lines, the angular width of the major and minor axes of the source region image is smaller, and the angle between the major axis of the source region image and the projected baseline is larger, than the values for source regions along 65° Mlat field lines. Thus, the effective angular width of the source region image is smaller for source regions along higher magnetic latitude field lines than for source regions along lower magnetic latitude field lines. The maximum effective angular width of the source region image is 0.788 at 19.25 hrs MLT for source region locations along 70° Mlat field lines, and 0.730 at 19.0 hrs MLT for source region locations along 75° Mlat field lines.

The second minimum in the normalized source region diameter occurs at 3.0 hrs MLT, for source regions located along 65° Mlat field lines. From Figure C-4, it can be seen that the projected baseline increases for source regions located between 20.0 and 6.0 hrs MLT. The combination of the decreasing effective angular source region image width and the increasing projected baseline produces a minimum in the normalized source region diameter at 3.0 hrs MLT. Minimums in the normalized source diameter are also found between 3.0 and 4.0 hrs MLT for source regions located along 70° and 75° Mlat field lines.

Figure C-9 is a plot of the normalized source region diameter, as a function of magnetic local time, for source regions located along 70° Mlat field lines, with the waves reflecting from the plasmopause at L-values between 4.25 and 3.75. The normalized source region diameter has a maximum value of 1.22, for a source location of 18.0 hrs MLT, with the waves reflecting from the plasmopause at an L-value of 4.25, and a minimum value of 1.073 for a source location of 3.75 hrs MLT, with the waves reflecting from the plasmopause at L-values between 4.0 and 4.25. From Figure C-9, the normalized source region diameter changes by only 1 percent for a change of 0.25 in the plasmopause L-value, for source regions located between 3.0 and 6.0 hrs MLT. For source regions along 65° and 75° Mlat field lines located between 3.0 and 6.0 hrs MLT, the maximum normalized source region diameter is 1.17 and the minimum normalized source region diameter is 1.05. Although the individual parameters that determine the normalized source region vary by as much as 35 percent, the normalized source region diameter itself varies by only 15 percent.

5. Wave Emission Angle

In situ measurements of the wave-normal angles of AKR near the source region indicate that the waves are emitted within $\pm 30^\circ$ of the perpendicular to the magnetic field [James, 1980]. Previous ray-tracing results [Omidi and Gurnett, 1984], for waves within the source region, indicate that there can be significant refraction upward. Thus, the wave-normal angle could vary significantly from the wave-normal

measurements at the source region and still be consistent with the current theories. For northern hemisphere source locations, the magnetic field is toward the earth; thus, waves propagating downward have wave-normal angles which are less than 90° and wave travelling upward have wave-normal angles which are greater than 90° .

Figure C-10 is a plot of the wave-normal angle, as a function of magnetic local time, for waves propagating directly to the spacecraft and for waves reflecting from the plasmopause at an L-value of 4.0. For source region locations along 65° Mlat field lines, with the waves propagating directly to the spacecraft, the wave-normal angle has a maximum value of 164.5° at 1.5 hrs MLT and a minimum value of 79.0° at 18.0 hrs MLT. The wave-normal angles vary over a wider range for source region locations along 65° Mlat field lines than for source region locations along 75° Mlat field lines. For source regions along 65° to 75° Mlat field lines located between 22.75 and 2.25 hrs MLT, the wave-normal angle varies from 127.8° to 164.5° .

For waves reflecting from the plasmopause at an L-value of 4.0, the wave-normal angle has a minimum value of 68.1° at 18.0 hrs MLT and a maximum wave-normal angle of 144.5° at 1.75 hrs MLT. The wave-normal angles vary over a wider range for source locations along 65° Mlat field lines than for source region locations along 75° Mlat field lines. Figure C-11 is a plot of the wave-normal angle, as a function of magnetic local time, for source regions along 70° Mlat field lines, with the waves reflecting from the plasmopause at L-values between 3.75 and 4.25. Waves that reflect from the plasmopause at lower

L-values, have larger wave-normal angles than do waves that reflect from the plasmopause at higher L-values. An increase in the L-value of the reflecting surface by 0.25 increases the wave-normal angle by approximately 5°. For source regions along 65° to 75° Mlat field lines located between 3.0 and 6.0 hrs MLT with the waves reflecting from the plasmopause, the wave-normal angle varies from 92.1° to 144.6°.

6. Source Region Brightness Temperature

To compute the brightness temperature of the source region image, equation (28), the flux density as a function of the source region brightness distribution, must be integrated with an elliptically-shaped Gaussian brightness distribution. Substituting the Gaussian brightness distribution,

$$T(x,y) = T_b e^{-4(x^2/\alpha_1^2 + y^2/\alpha_2^2)} , \quad (C-15)$$

into equation (28) and integrating gives the result:

$$s = \frac{k\pi\alpha_1\alpha_2}{2\lambda^2} T_b \quad (C-16)$$

for the flux density, where T_b is the central brightness temperature, k is Boltzmann's constant, λ is the wavelength, α_1 is the angular width of the major axis, and α_2 is the angular width of the minor

axis. Solving equation (C-16) for the brightness temperature, as a function of the source region angular width, gives:

$$T_b = \frac{2s\lambda^2}{k\pi\alpha_1\alpha_2} \quad . \quad (C-17)$$

Equation (C-17) reduces to equation (30) for circularly symmetric Gaussian brightness distributions; i.e., when $\alpha_1 = \alpha_2$. From equation (C-17), the brightness temperature is proportional to the flux density divided by the solid angle that the source region subtends. The flux density can be increased significantly if the waves are focused on the spacecraft by the reflecting surface.

For waves propagating directly to the spacecraft, the flux density s , measured at the spacecraft is related to the flux density s_s , at the outside edge of the source region by:

$$s = \frac{s_s d^2}{4 R_{ss}^2} \quad , \quad (C-18)$$

where d is the diameter of the source region and R_{ss} is the radial distance of the spacecraft from the source region. Within the source region, the wave growth is exponential; thus, the flux density at the outer edge of the source region is:

$$s_s = s_g \times e^{d\gamma} \quad , \quad (C-19)$$

where γ is the growth rate and s_g is the flux density of the galactic background noise. Substituting equations (C-7) and (C-19) into equation (C-18) gives the flux density, as a function of the angular width of the source region and the amplification length within the source region,

$$s = \frac{1}{4} \alpha^2 s_g \times e^{d\gamma} \quad . \quad (C-20)$$

For waves propagating directly to the spacecraft, the solid angle subtended by the source region is equal to the solid angle of amplified galactic background noise illuminating the spacecraft. Thus, the flux density at the spacecraft is:

$$s = \frac{1}{\pi} A_b s_g \times e^{d\gamma} \quad , \quad (C-21)$$

where A_b is the solid angle of amplified galactic background noise illuminating the spacecraft.

For waves which reflect from the plasmopause, the solid angle of amplified galactic background noise illuminating the spacecraft can be significantly greater than the solid angle subtended by the source region image or the solid angle subtended by the source region. Substituting equation (C-21) into equation (C-17) gives the brightness temperature of the source region image:

$$T_b = \frac{\lambda^2 A_b s_g \times e^{d\gamma}}{2\pi k (\frac{1}{4}\pi \alpha'_1 \alpha'_2)} = \frac{\lambda^2 A_b s_g \times e^{d\gamma}}{2\pi k A_1} \quad , \quad (C-22)$$

where $\frac{1}{4}\pi \alpha'_1 \alpha'_2 = A_1$ is the solid angle subtended by the source region image, A_b is the solid angle of amplified galactic background noise illuminating the spacecraft, and d is the amplification length within the source region.

For waves propagating directly to the spacecraft, the brightness temperature is proportional to the flux density of the waves, measured at the spacecraft, divided by the solid angle subtended by the source region [equation (30)]. The source region brightness temperature varies from 0.94, near 18.0 hrs MLT, to 1.81, at 6.0 hrs MLT, times the source region brightness temperature of a source region located at 18.0 hrs MLT along a 70° Mlat field line. For source regions located between 22.75 and 2.25 hrs MLT, the brightness temperature varies from 1.09 to 1.53 times the source region brightness temperature of a source region located at 18.0 hrs MLT along a 70° Mlat field line.

For waves reflecting from the plasmopause, the brightness temperature of the source region image can be much greater than the source region brightness temperature. From equation (C-22), the brightness temperature of the source region image is proportional to the solid angle of amplified galactic background noise illuminating the spacecraft, divided by the solid angle subtended by the source region image. Figure C-12 is a plot of the solid angle of amplified

galactic background noise illuminating the spacecraft, for a source region located along a 70° Mlat field line at 21.0 hrs MLT. Figure C-12 is normalized so that the solid angle of amplified galactic background noise illuminating the spacecraft is a circle of radius equal to one for waves propagating directly to the spacecraft. An equation, which gives a close fit to the calculated solid angle of amplified galactic background noise illuminating the spacecraft is:

$$r^2 = a_1^2 \cos^2(\theta - \phi) + a_2^2 \sin^2(\theta - \phi) \quad , \quad (C-23)$$

where a_1 is the maximum angular radius of the curve, a_2 is the minimum angular radius of the curve, and ϕ is the inclination of the curve.

The solid angle enclosed by the curve defined by equation (C-23) is:

$$A_b = \frac{\pi}{2}(a_1^2 + a_2^2) \quad . \quad (C-24)$$

The solid angle of amplified galactic background noise illuminating the spacecraft, for waves propagating directly to the spacecraft, is:

$$A = \pi \alpha_n^2 \quad , \quad (C-25)$$

where $\alpha_n = 1$ is the normalized angular radius of the source region. The normalized solid angle of galactic background noise illuminating the spacecraft, for waves reflecting from the plasmopause, is defined

as equation (C-24) divided by equation (C-25). Thus the normalized solid angle of galactic background noise is:

$$A_n = \frac{1}{2}(a_1^2 + a_2^2) \quad . \quad (C-26)$$

Figure C-13 is a plot of the normalized solid angle of galactic background noise illuminating the spacecraft, as a function of magnetic local time, for source regions along 65° to 75° Mlat field lines, with the waves reflecting from the plasmopause at an L-value of 4.0. The positions of the spacecraft, used in the computation of Figure C-13, are the approximate positions of ISEE-1 and -2 on February 20, 1979 between 0030 and 0050 UT. The normalized solid angle of galactic background noise is largest for source regions along 65° Mlat field lines and smallest for source regions along 75° Mlat field lines. The largest value for the normalized solid angle of galactic background noise occurs at 1.75 hrs MLT, which corresponds to the magnetic local time of the spacecraft. The largest value for the normalized solid angle of galactic background noise is 78.4 occurring for a source location along a 65° Mlat field line at 1.75 hrs MLT, with the waves reflecting from the plasmopause at an L-value of 4.25. The smallest value for the normalized solid angle of galactic background noise is 11.9, occurring for a source location along a 75° Mlat field line at 18.0 hrs MLT, with the waves reflecting from the plasmopause at an L-value of 4.25. For source regions between 3.0 and 6.0

hrs MLT, the maximum value for the normalized solid angle of galactic background noise is 73.3, at 3.0 hrs MLT, and the minimum value for the solid angle of galactic background radiation is 17.8, at 6.0 hrs MLT. Since the flux density of the waves detected by the spacecraft is proportional to the solid angle of galactic background noise illuminating the spacecraft, the flux density of the waves reflecting from the plasmopause is from 17.8 to 73.3 times greater than the flux density of the waves propagating directly to the spacecraft, for source locations between 3.0 and 6.0 hrs MLT.

From equation (C-22), the brightness temperature of the source region image is proportional to the solid angle of amplified galactic background noise illuminating the spacecraft divided by the solid angle subtended by the source region image. For a source region located along a 65° Mlat field line at 3.0 hrs MLT, with the waves reflecting from the plasmopause at an L-value of 4.25, the solid angle subtended by the source region image is 0.232 times smaller than the solid angle subtended by the source region. Thus, the brightness temperature of the source region image can be up to 316.0 times brighter than the source region. For a source region located along a 65° Mlat field line at 6.0 hrs MLT, with the waves reflecting from the plasmopause at an L-value of 4.25, the solid angle subtended by the source region image is 0.208 times smaller than the solid angle subtended by the source region. Thus, the brightness temperature of the source region image can be a minimum of 85.6 times brighter than the source region.

D. Summary

1. February 20, 1979 from 0030 to 0050 UT

If the waves are assumed to propagate directly to the spacecraft, the propagation time difference predicts a source location of 22.75 to 2.25 hrs MLT. For source locations between 22.75 and 2.25 hrs MLT, the source diameter will be from 0.761 to 0.936 times smaller and from 1.09 to 1.53 times brighter than the results computed with an assumed position of 21.0 hrs MLT along a 70° Mlat field line.

If the waves are assumed to be reflected from the plasmopause, the propagation time difference predicts a source location of 3.0 to 6.0 hrs MLT. For source locations between 3.0 and 6.0 hrs MLT, the source diameter will be from 1.05 to 1.17 times larger than the results computed with an assumed position of 21.0 hrs MLT along a 70° Mlat field line. The brightness temperature of the source region image will be from 85.6 to 316.0 times brighter, and the flux density of the radiation detected by the spacecraft will be from 17.8 to 73.3 times greater than the brightness temperature and flux density if the waves propagate directly to the spacecraft.

2. February 20, 1979 from 0300 to 0320 UT

The ray-tracing results for February 20, 1979 from 0300 to 0320 UT do not differ significantly from the results computed for 0030 to 0050 UT. If the waves are assumed to propagate directly to the spacecraft, the propagation time difference predicts a source location of 21.5 to 1.75 hrs MLT. For source locations between 21.5 and 1.75 hrs

MLT, the source diameter will be from 0.867 to 0.982 times smaller and from 1.02 to 1.22 times brighter than the results computed with an assumed position of 21.0 hrs MLT along a 70° Mlat field line.

If the waves are assumed to be reflected from the plasmopause, the propagation time difference predicts a source location of 1.25 to 6.0 hrs MLT. For source locations between 1.25 and 6.0 hrs MLT, the source diameter will be from 1.10 to 1.34 times larger than the results computed with an assumed position of 21.0 hrs MLT along a 70° Mlat field line. The brightness temperature of the source region image will be from 112.2 to 420.8 times brighter, and the flux density of the radiation detected by the spacecraft will be from 27.5 to 120.6 times greater than the brightness temperature and flux density if the waves propagate directly to the spacecraft.

Table C-1
Spacecraft Coordinates Used in the Ray-Tracing Analysis

Spacecraft	UT	Radial Distance (R_E)	Magnetic Local Time (hrs)	Magnetic Latitude (deg)
ISEE-1	0030-0050	11.249	1.625	27.703
ISEE-2	0030-0050	12.838	1.789	24.633
ISEE-1	0300-0320	13.867	1.935	29.459
ISEE-2	0300-0320	15.149	2.051	27.394

Figure C-1. This figure shows the geometry of the AKR source region, the plasmopause, and the R-X mode cutoff surface. In the region where the waves are predicted to reflect, the R-X cutoff surface closely follows the plasmopause.

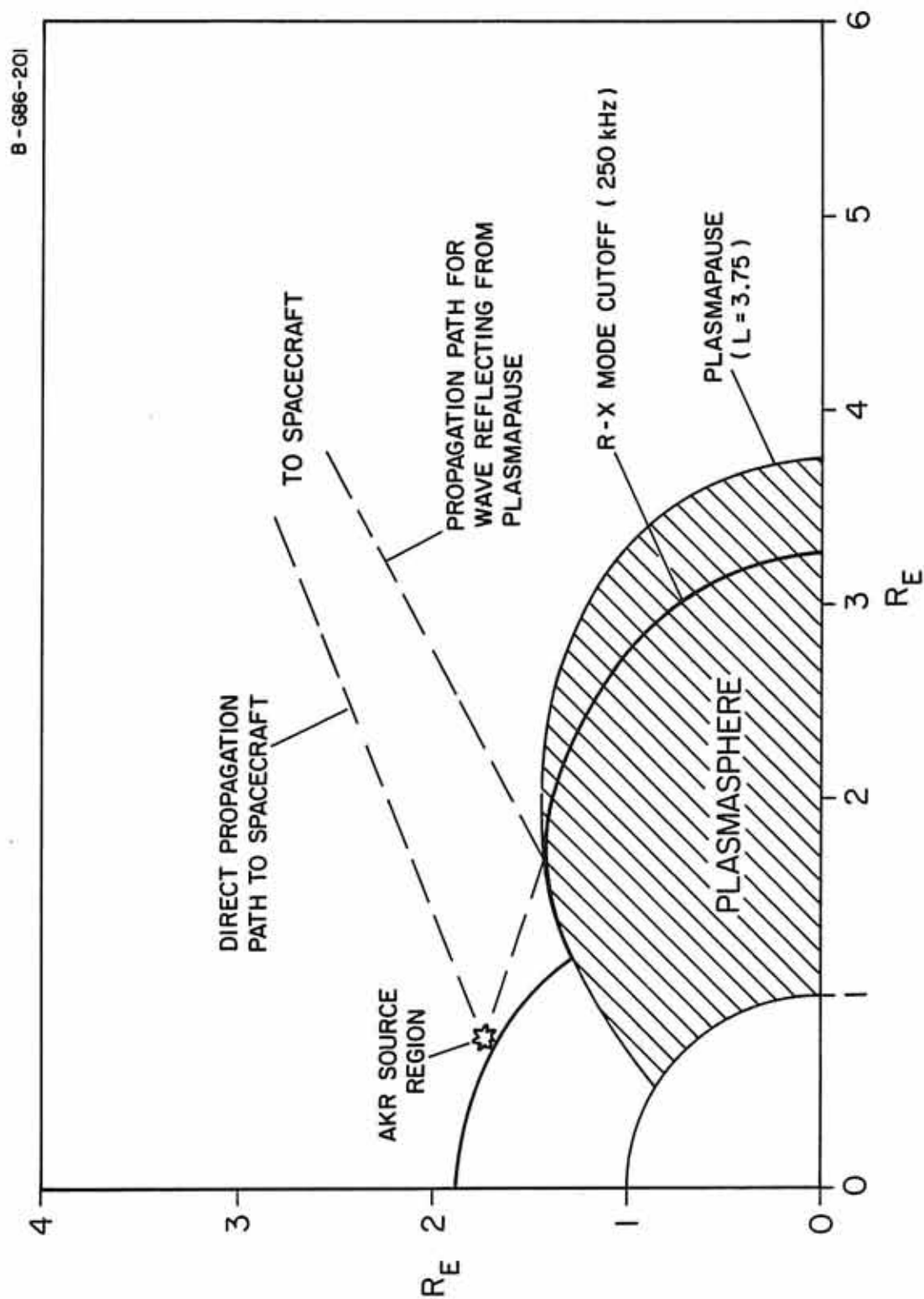


Figure C-1

Figure C-2. This figure shows the propagation time difference, as a function of magnetic local time, for waves which propagate directly to the spacecraft.

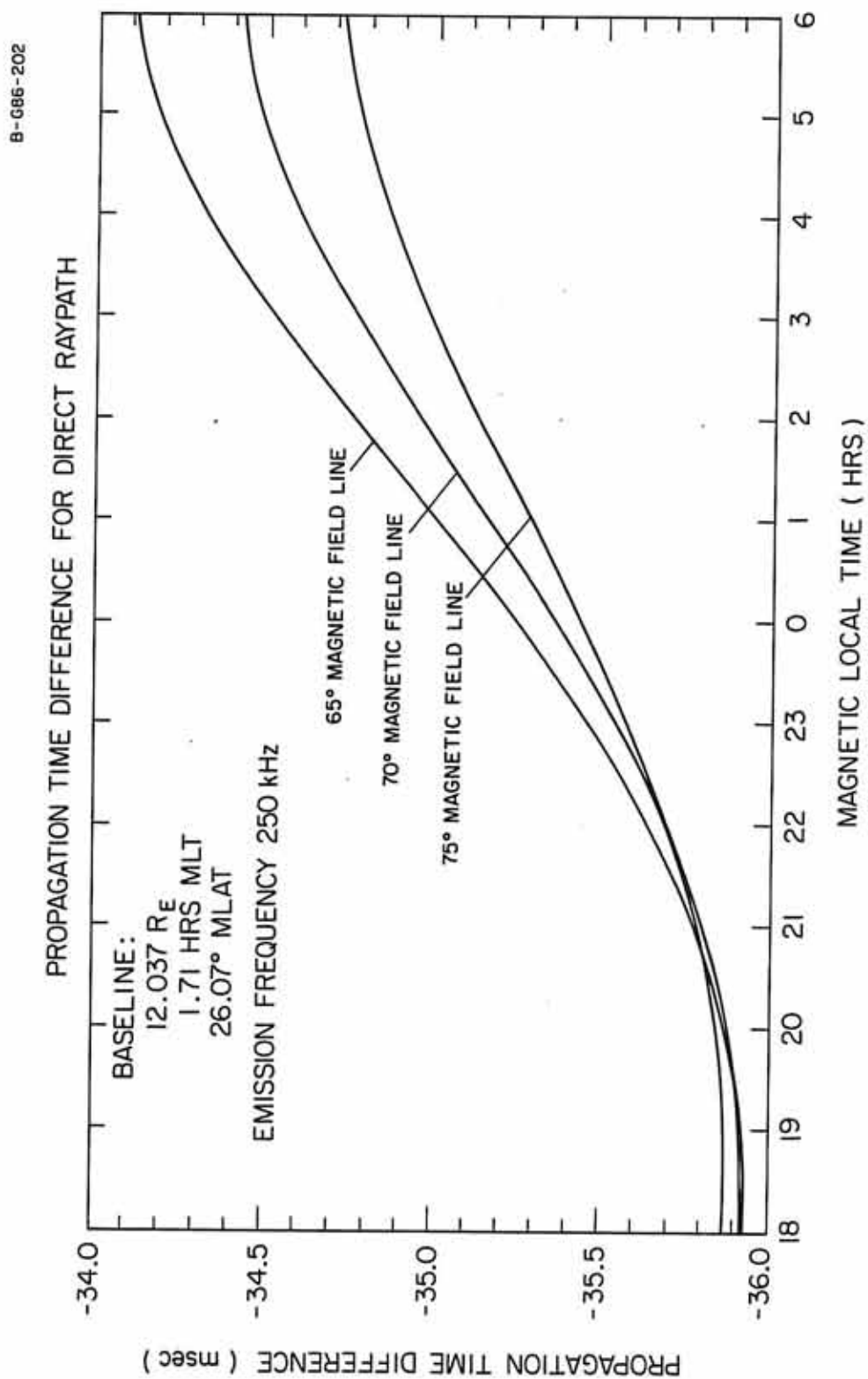


Figure C-2

Figure C-3. This figure shows the propagation time difference, as a function of magnetic local time, for waves which reflect from the plasmapause at an L-value of 4.00.

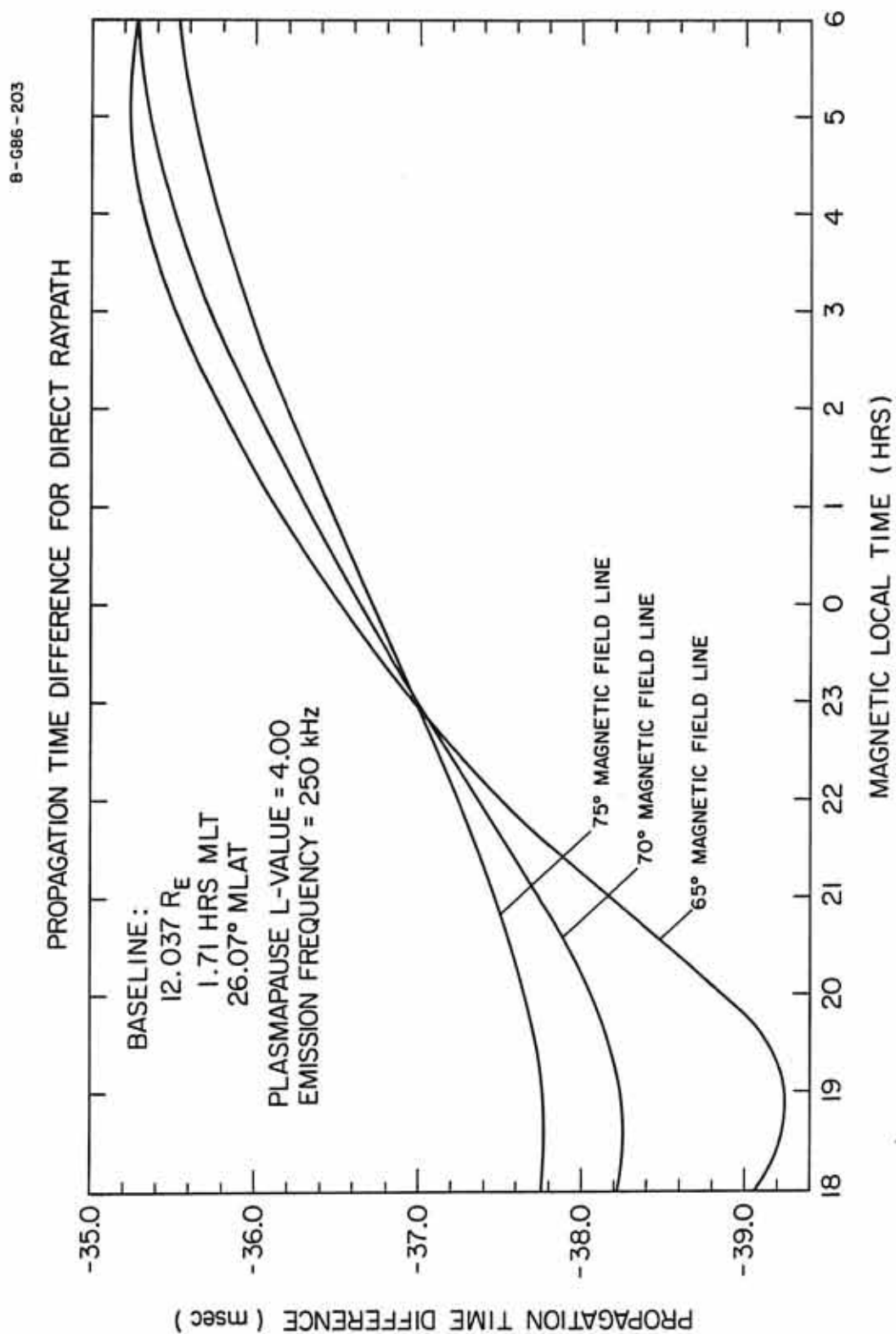


Figure C-3

Figure C-4. This figure shows the projected baseline, as a function of magnetic local time, for waves which propagate directly to the spacecraft and for waves which reflect from the plasmopause at an L-value of 4.00. The projected baseline for waves which reflect from the plasmopause is larger than the projected baseline of waves which propagate directly to the spacecraft.

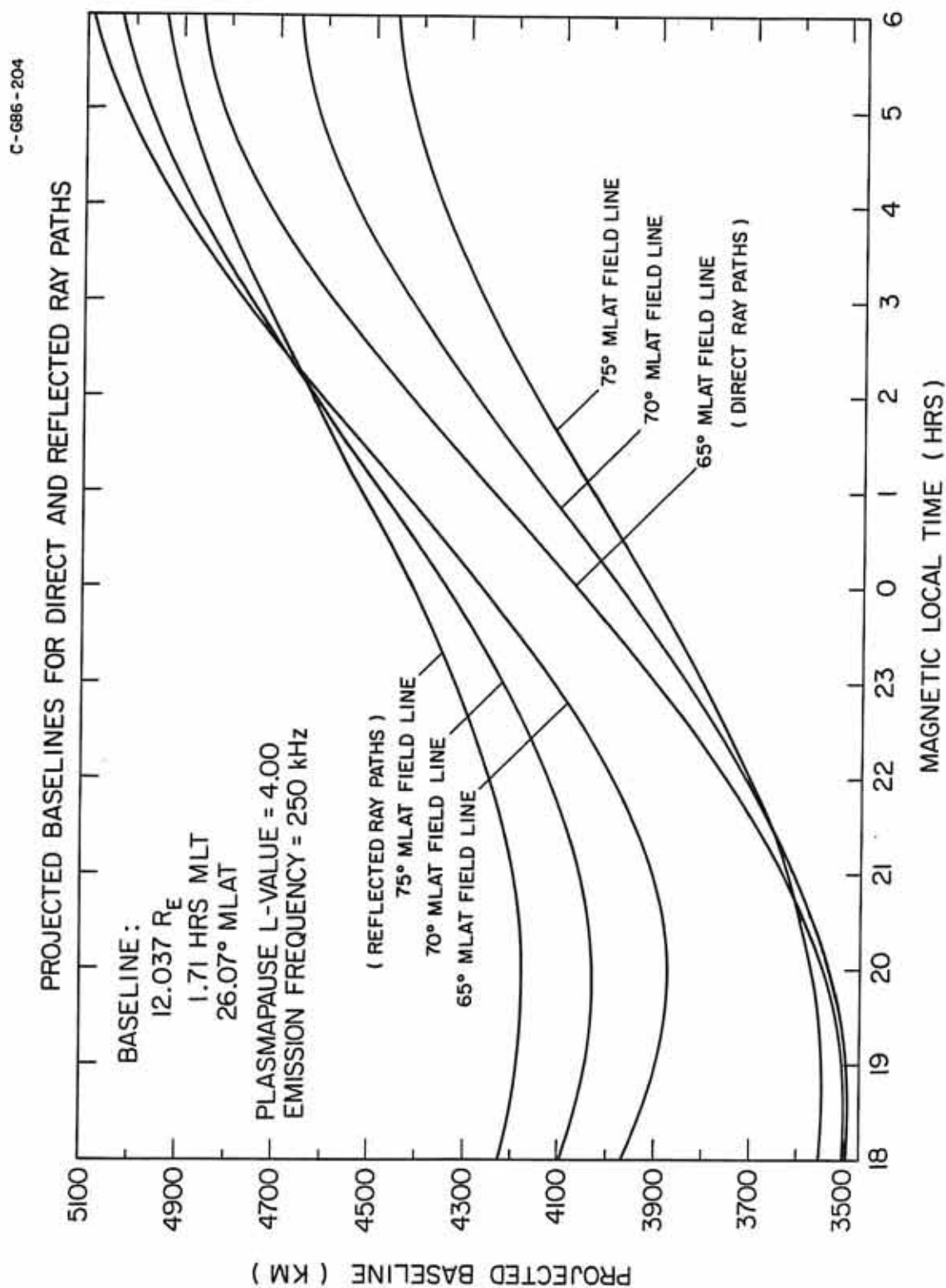


Figure C-4

Figure C-5. This figure shows the projected baseline for waves which reflect from the plasmopause at different L-values, and the projected baseline for waves which propagate directly to the spacecraft, with a source region located along a 70° Mlat field line.

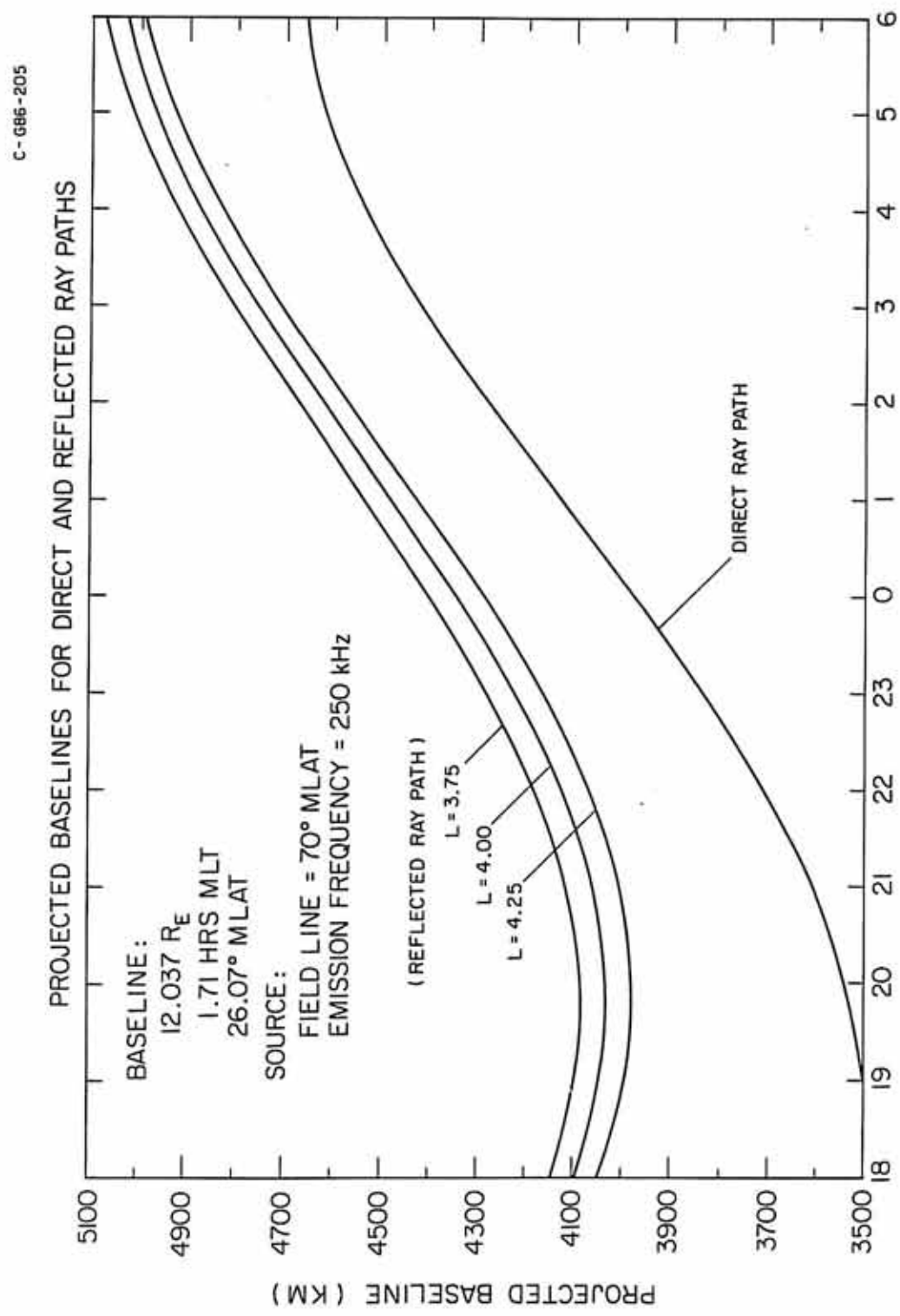


Figure C-5

Figure C-6. This figure shows the size and shape of the source region image when the waves are reflected from the plasmopause. The size is normalized so that the source region has a diameter of one, for waves which propagate directly to the spacecraft. The shape of the source region image is approximately elliptical, for small source regions.

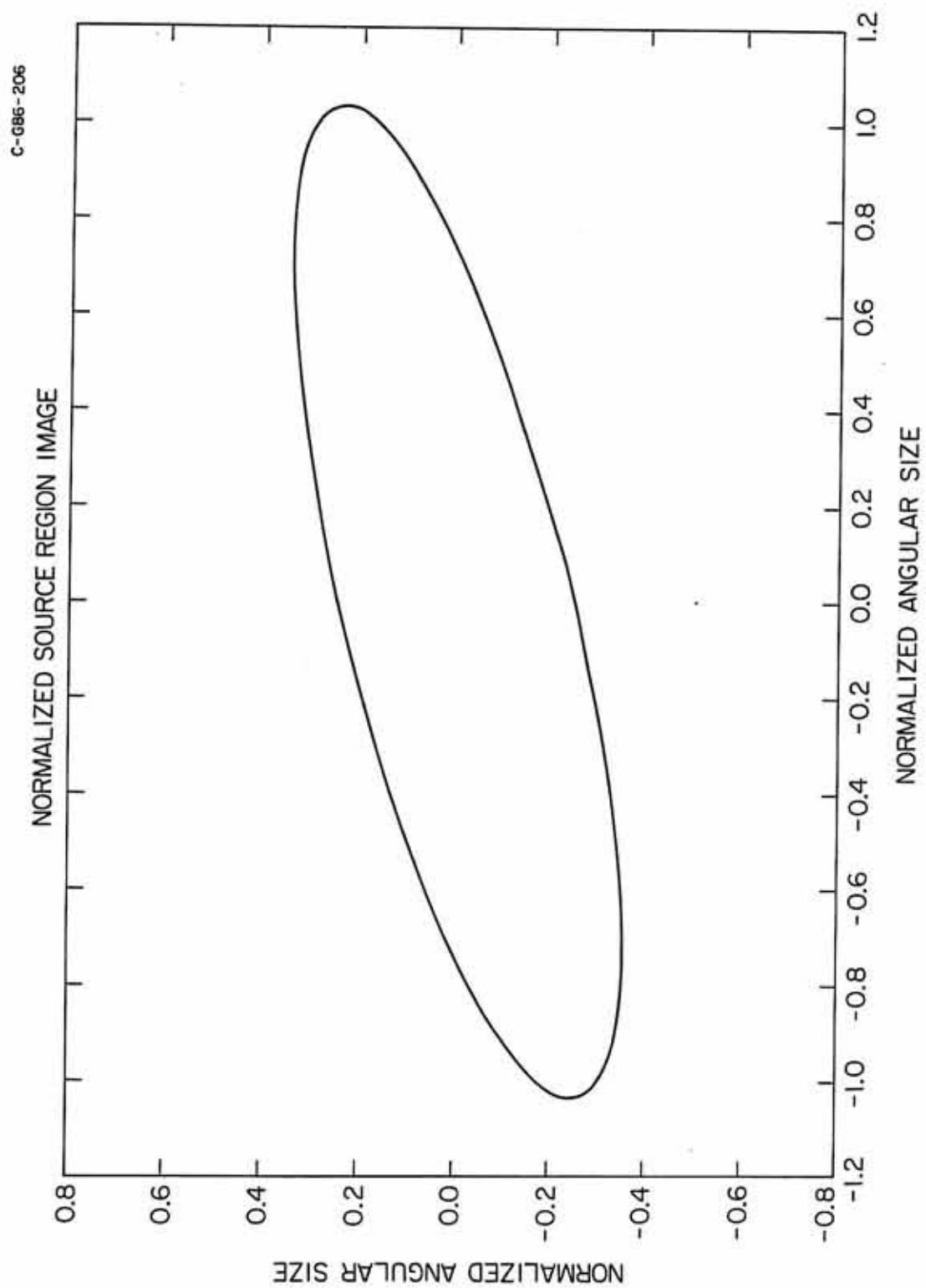


Figure C-7. This figure shows the normalized AKR source region diameter for waves which propagate directly to the spacecraft. The source region diameter is larger for source region locations near 18.0 hrs MLT than for source region locations near 6.0 hrs MLT, with the same correlation.

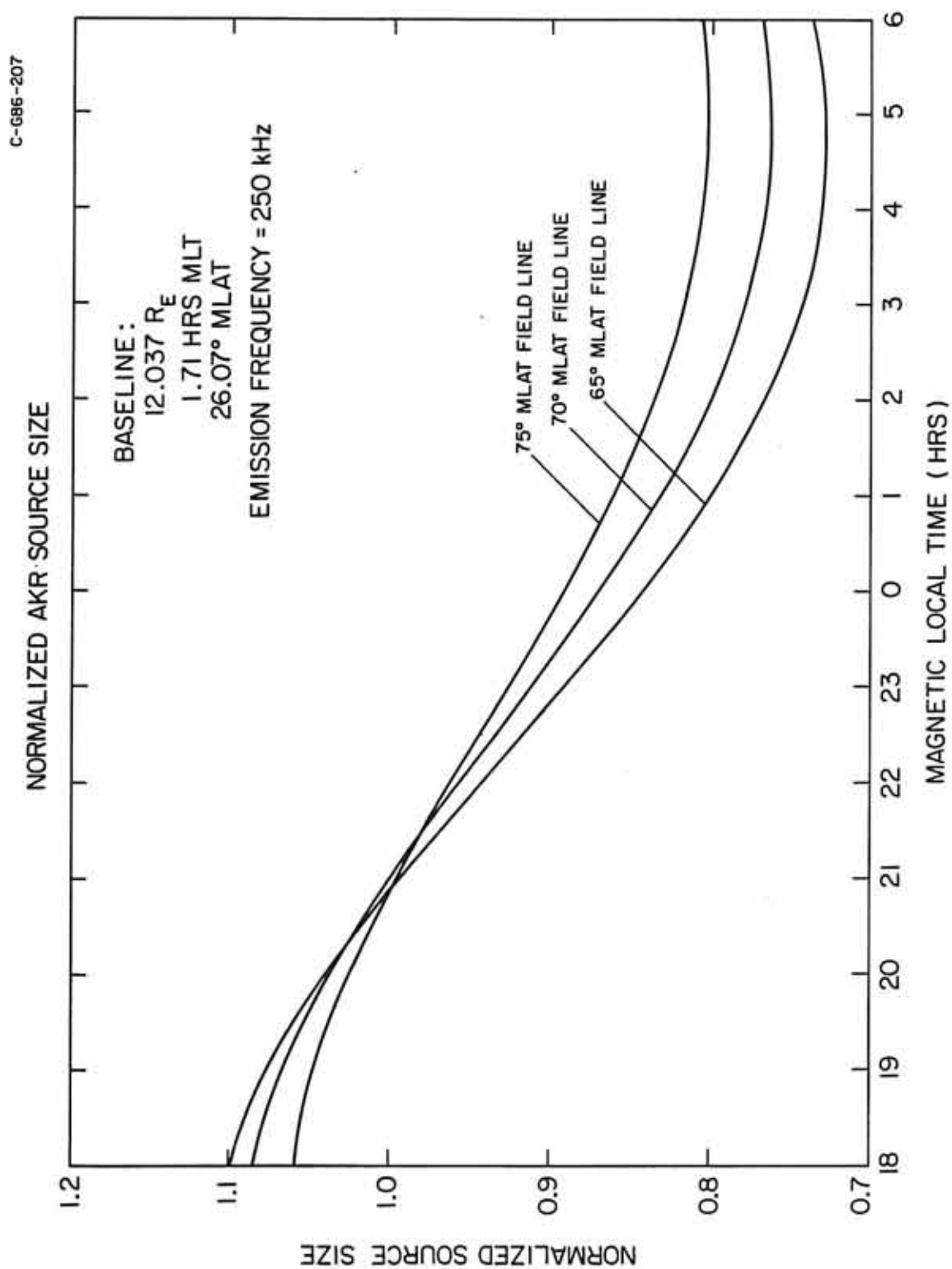


Figure C-7

Figure C-8. This figure shows the normalized AKR source region diameter for waves which reflect from the plasmopause at an L-value of 4.00. The curves are normalized so that a value of one is the same diameter as a source region located along a 70° Mlat field line at 21.0 hrs MLT, with the waves propagating directly to the spacecraft.

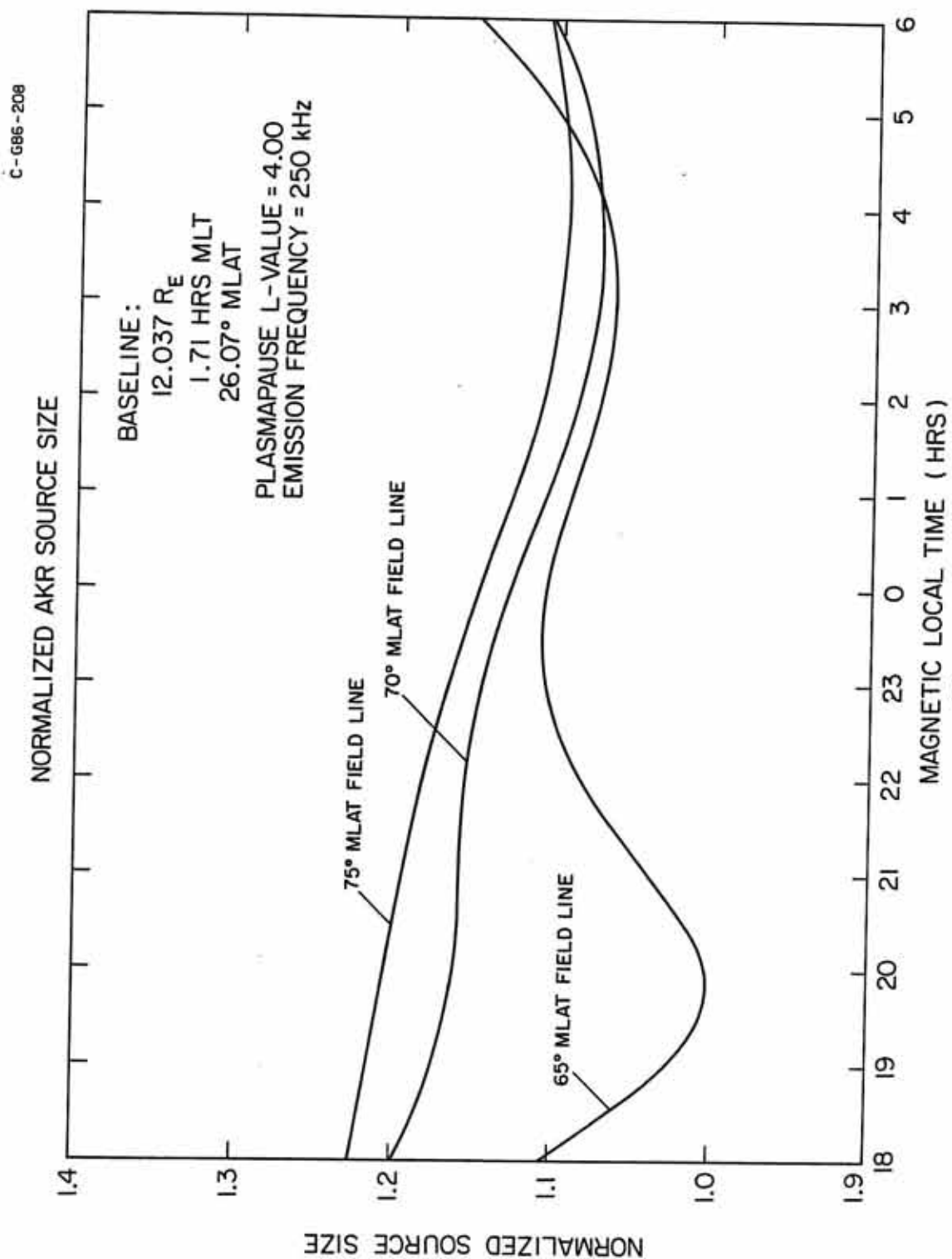


Figure C-9. This figure shows the normalized source region diameter for waves which reflect from the plasmopause at different L-values, and for comparison, a plot of the normalized source region diameter for waves propagating directly to the spacecraft. The normalized source diameter changes only slightly for different L-values of the reflecting surface.

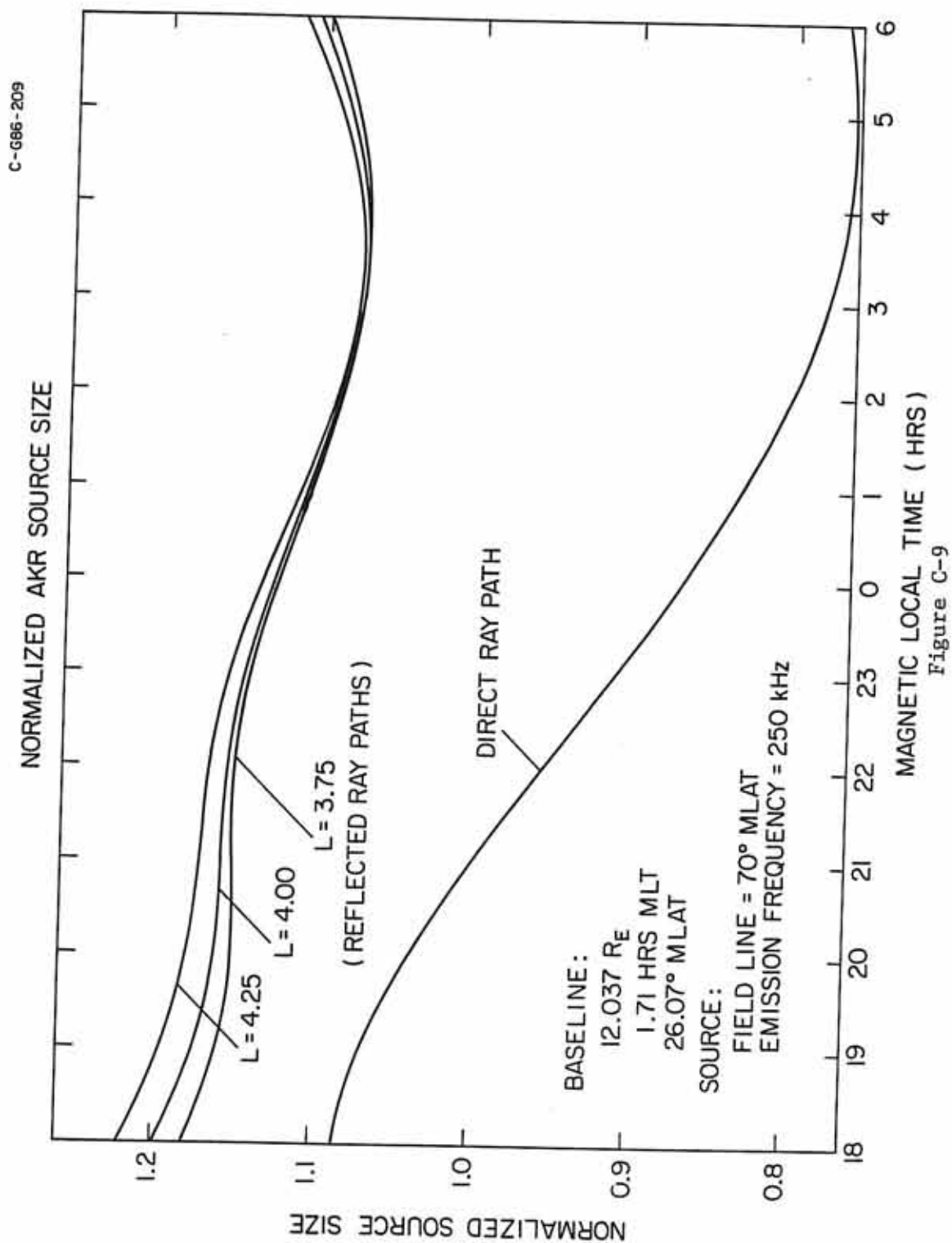


Figure C-10. This figure shows the wave-normal angle of the emitted waves which propagate directly to the spacecraft, and the wave-normal angle of the emitted waves which reflect from the plasmopause at an L-value of 4.0.

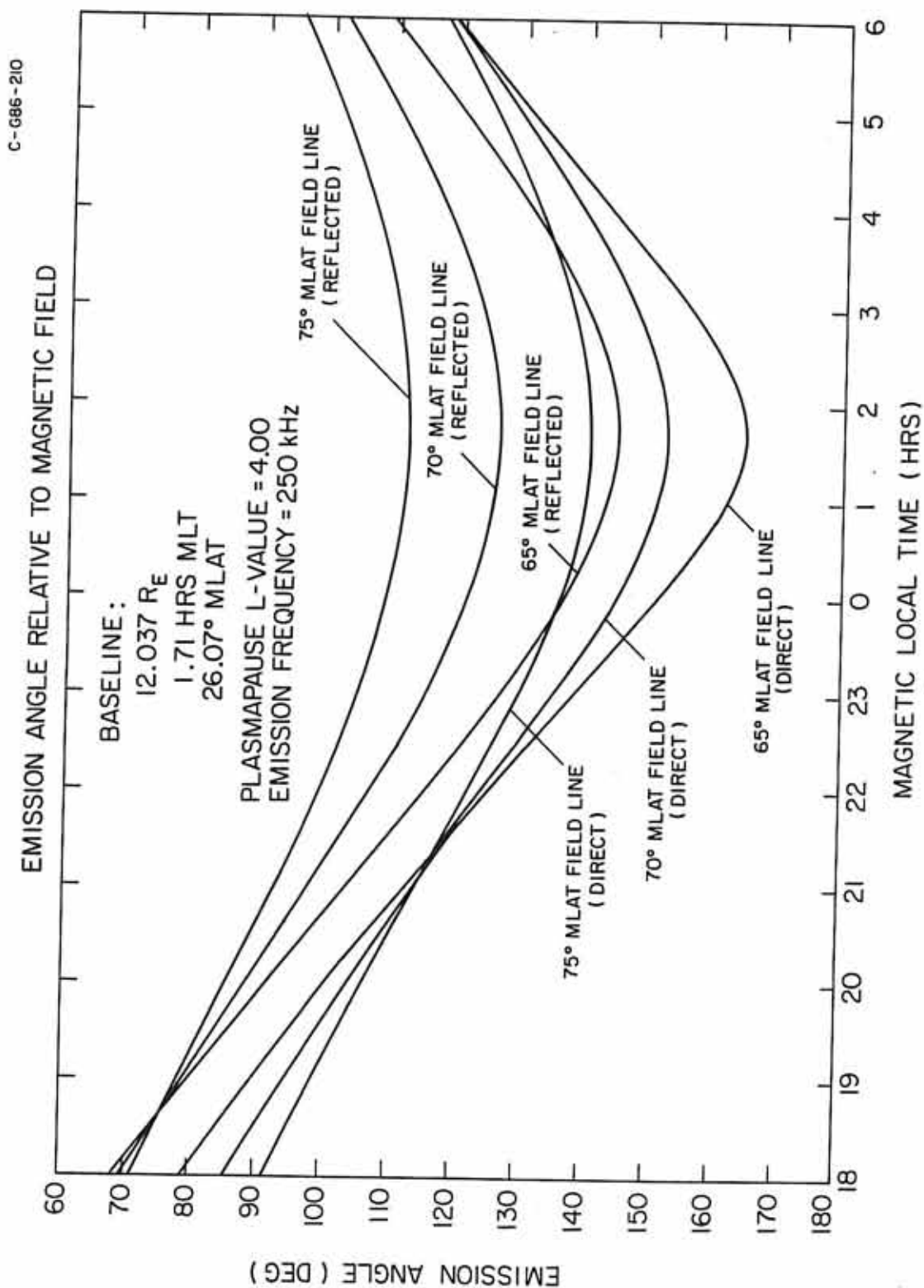


Figure C-10

Figure C-11. This figure shows the wave-normal angle of the emitted waves which reflect from the plasmopause. An increase of 0.25 in L-value causes a maximum increase in the wave-normal angle of 5° , for plasmopause L-values between 3.75 and 4.00.

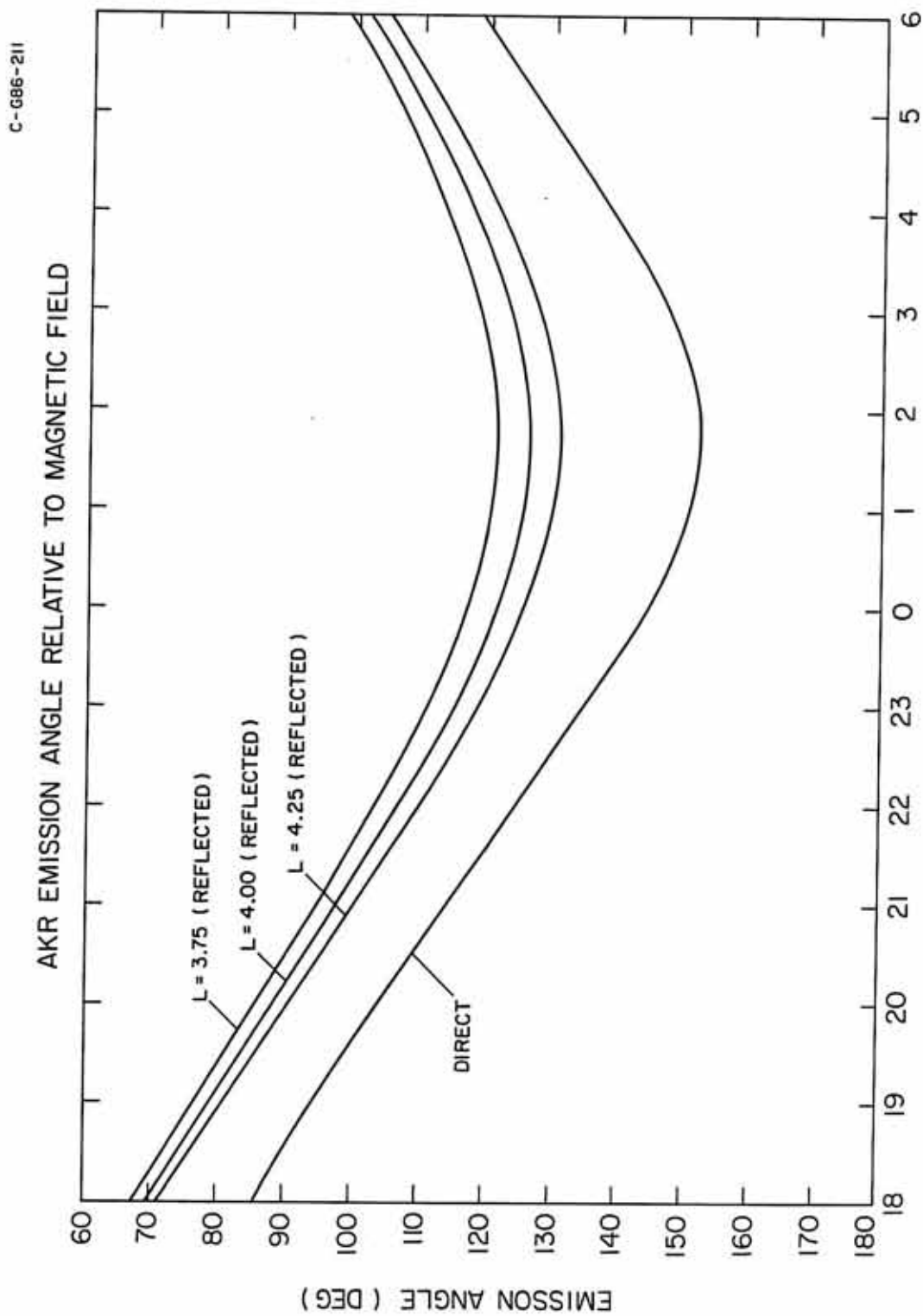


Figure C-12. This figure shows the normalized size and shape of the solid angle of amplified galactic background noise illuminating the spacecraft, for waves reflecting from the plasmopause. The radius is normalized so that a circle of radius equal to one is the solid angle of amplified galactic background noise illuminating the spacecraft when the waves propagate directly to the spacecraft.

C-G86-212

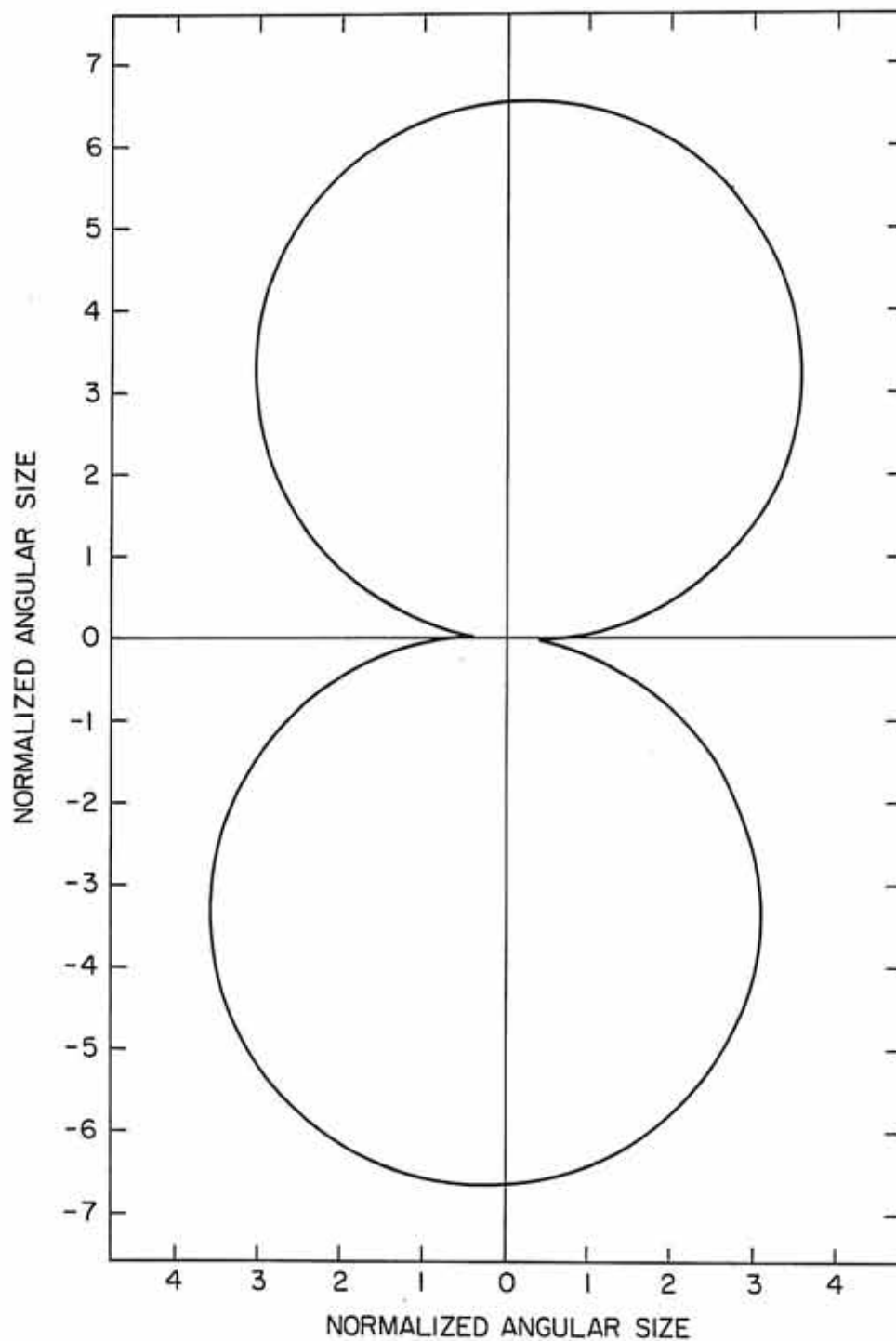
NORMALIZED SOLID ANGLE
OF GALACTIC BACKGROUND RADIATION

Figure C-12

Figure C-13. The flux density of the waves received at the spacecraft is proportional to the solid angle of amplified background noise illuminating the spacecraft. This figure is a plot of the solid angle of amplified background radiation illuminating the spacecraft. The flux density of the received signal is from 17.8 to 73.3 times greater for waves reflecting from the plasmopause than for waves propagating directly to the spacecraft.

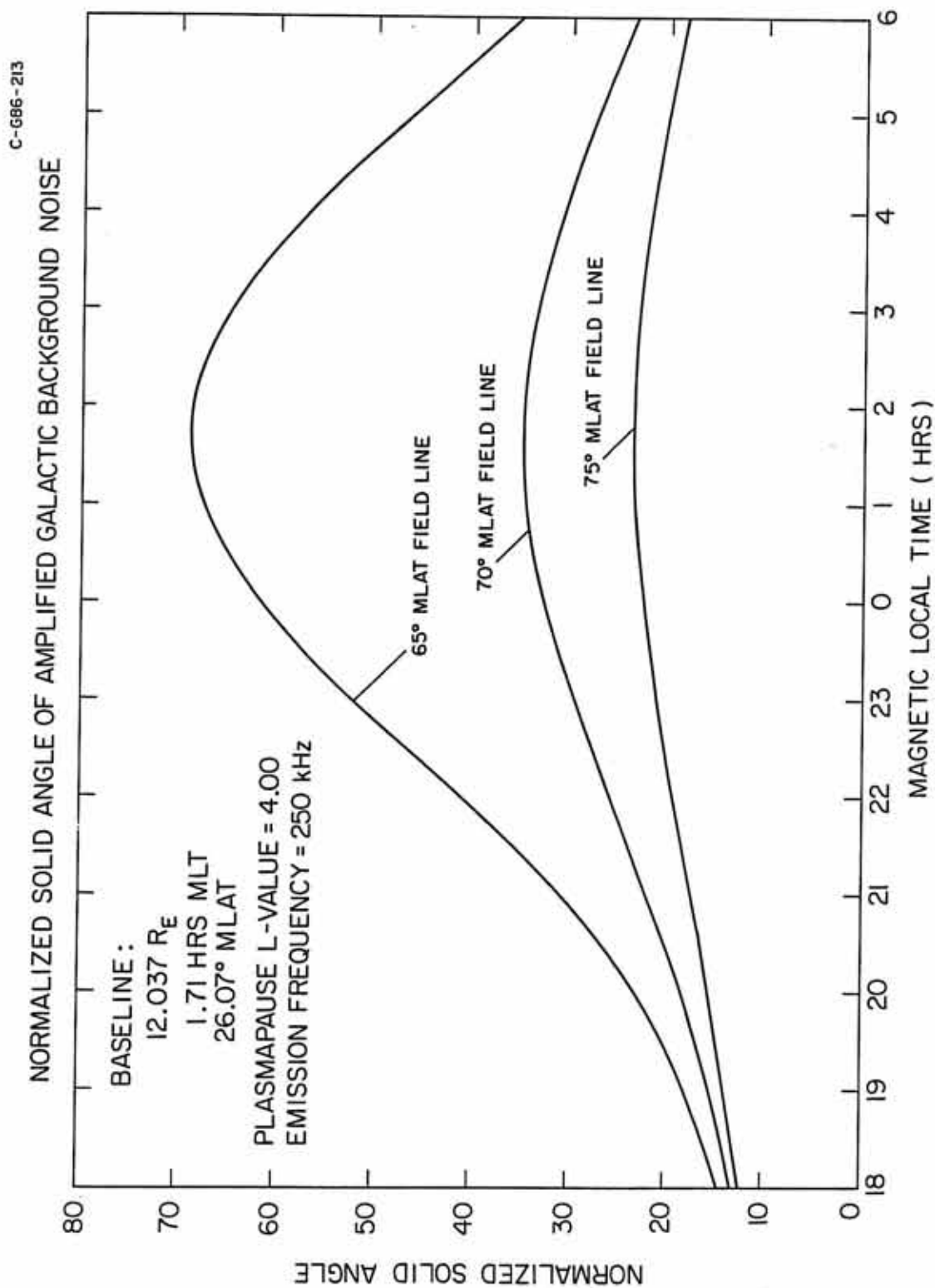


Figure C-13

REFERENCES

- Ackerson, K. L. and L. A. Frank, Correlated Satellite Measurements of Low-Energy Electron Precipitation and Ground-Based Observations of a Visible Auroral Arc, J. Geophys. Res., 77, 1128, 1972.
- Alexander, J. K., L. W. Brown, T. A. Clark, and R. G. Stone, Low Frequency Cosmic Noise Observations of the Constitution of the Local System, Astron. Astrophys., 6, 476, 1970.
- Alexander, J. K., M. L. Kaiser, and P. Rodriguez, Scattering of Terrestrial Kilometric Radiation at Very High Altitudes, J. Geophys. Res., 84, 2619, 1979.
- Benediktov, E. A., G. G. Getmantsev, N. A. Mityakov, V. O. Rapoport, and A. F. Tarasov, Relation Between Geomagnetic Activity and the Sporadic Radio Emission Recorded by the Elektron Satellites, Kosm. Issled., 6, 946, 1968.
- Benediktov, E. A., G. G. Getmantsev, Yu. A. Sazonov, and A. F. Tarasov, Preliminary Results of Measurement of the Intensity of Distributed Extraterrestrial Radio-frequency emission at 725 and 1525-kHz Frequencies by the Satellite Elektron-2, Cosmic Research, English transl., 3, 492, 1965.
(Kosm. Issled., 3, 614, 1965)
- Benson, R. F., Harmonic Auroral Kilometric Radiation of Natural Origin, Geophys. Res. Lett., 9, 1120, 1982.
- Benson, R. F., Ordinary Mode Auroral Kilometric Radiation--With Harmonics--Observed by ISIS-1, Radio Sci., 19, 543, 1984.
- Benson, R. F. and W. Calvert, ISIS 1 Observations at the Source of Auroral Kilometric Radiation, Geophys. Res. Lett., 6, 479, 1979.
- Benson, R. F., W. Calvert, and D. M. Klumpar, Simultaneous Wave and Particle Observations in the Auroral Kilometric Radiation Source Region, Geophys. Res. Lett., 7, 959, 1980.
- Block, L. P., The Magnetosphere, in Cosmical Geophysics, ed. by A. Egeland, Ø. Holter, and A. Ohmolt, p. 103, Universitetsforlaget, Oslo, 1973.

- Born, M., and E. Wolf, Principles of Optics, 3rd Edition, Pergamon Press, Oxford, 1965.
- Brown, L. W., The Galactic Radio Spectrum Between 130 kHz and 2,600 kHz, Astrophys. J., 180, 359, 1973.
- Calvert, W., The Signature of Auroral Kilometric Radiation on ISIS I Ionograms, J. Geophys. Res., 86, 76, 1981a.
- Calvert, W., The Auroral Plasma Cavity, Geophys. Res. Lett., 8, 919, 1981b.
- Calvert, W., The Stimulation of Auroral Kilometric Radiation by Type III Solar Radio Bursts, Geophys. Res. Lett., 8, 1091, 1981c.
- Calvert, W., A Feedback Model for the Source of Auroral Kilometric Radiation, J. Geophys. Res., 87, 8199, 1982.
- Calvert, W., Auroral Kilometric Radiation Triggered by Type III Solar Radio Bursts, Geophys. Res. Lett., 12, 377, 1985a.
- Calvert, W., DE-1 Measurements of AKR Wave Directions, Geophys. Res. Lett., 12, 381, 1985b.
- Carpenter, D. L., Whistler Studies of the Plasmapause in the Magnetosphere, J. Geophys. Res., 71, 693, 1966.
- Carpenter, D. L., R. R. Anderson, T. F. Bell, and T. R. Miller, A Comparison of Equatorial Electron Densities Measured by a Satellite Radio Technique, Geophys. Res. Lett., 8, 1107, 1981.
- Dulk, G. A., Characteristics of Jupiter's Decametric Radio Source Measured with Arc-Second Resolution, Astrophys. J., 159, 671, 1970.
- Dunckel, N., B. Ficklin, L. Rorden, and R. A. Helliwell, Low-Frequency Noise Observed in the Distant Magnetosphere With OGO 1, J. Geophys. Res., 75, 1854, 1970.
- Farrell, W. M., A Statistical Study of Solar Type III Bursts and Auroral Kilometric Radiation, M.S. Thesis, 48 pp., University of Iowa, Iowa City, 1984.
- Farrell, W. M., W. Calvert, and D. A. Gurnett, AKR Signal Increases Caused by Triggering, Geophys. Res. Lett., 13, 370, 1986.
- Farrell, W. M., and D. A. Gurnett, The Statistical Study of Solar Type III Bursts and Auroral Kilometric Radiation Onsets, J. Geophys. Res., 90, 9634, 1985.

- Fomalont, E. B., and M. C. H. Wright, Interferometry and Aperture Synthesis, in Galactic and Extra-Galactic Radio Astronomy, ed. by G. L. Verschuur and K. I. Kellermann, p. 256 Springer-Verlag, New York, 1974.
- Frank, L. A., and K. L. Ackerson, Observations of Charged Particle Precipitation into the Auroral Zone, J. Geophys. Res., 76, 3612, 1971.
- Gallagher, D. L., and D. A. Gurnett, Auroral Kilometric Radiation: Time-Averaged Source Location, J. Geophys. Res., 84, 6501, 1979.
- Grabbe, C. L., Auroral Kilometric Radiation: A Theoretical Review, Rev. Geophys. Space Phys., 19, 627, 1981.
- Green, J. L., and D. L. Gallagher, The Detailed Intensity Distribution of the AKR Emission Cone, J. Geophys. Res., 90, 9641, 1985.
- Green, J. L., D. A. Gurnett, and R. A. Hoffman, A Correlation Between Auroral Kilometric Radiation and Inverted V Electron Precipitation, J. Geophys. Res., 84, 5216, 1979.
- Green, J. L., D. A. Gurnett, and S. D. Shawhan, The Angular Distribution of Auroral Kilometric Radiation, J. Geophys. Res., 82, 1825, 1977.
- Gurnett, D. A., The Earth as a Radio Source: Terrestrial Kilometric Radiation, J. Geophys. Res., 79, 4227, 1974.
- Gurnett, D. A. and R. R. Anderson, The Kilometric Radio Emission Spectrum: Relationship to Auroral Acceleration Processes, in Physics of Auroral Arc Formation, ed. by S.-I. Akasofu and J. R. Kan, p. 341, Geophys. Monogr. Ser., Vol. 25, AGU, Washington, D. C., 1981.
- Gurnett, D. A., R. R. Anderson, F. L. Scarf, R. W. Fredricks, and E. J. Smith, Initial Results from the ISEE-1 and -2 Plasma Wave Investigation, Space Sci. Rev., 23, 103, 1979.
- Gurnett, D. A. and J. L. Green, On the Polarization and Origin of Auroral Kilometric Radiation, J. Geophys. Res., 83, 689, 1978.
- Gurnett, D. A., F. L. Scarf, R. W. Fredricks, and E. J. Smith, The ISEE-1 and -2 Plasma Wave Investigation, IEEE Trans. Geosci. Electron., 16, 225, 1978.

- Hanbury Brown, R., H. P. Palmer, and A. R. Thompson, A Rotating-Lobe Interferometer and its Application to Radio Astronomy, Phil. Mag., 46, 863, 1955.
- Hashimoto, K., A Reconciliation of Propagation Modes of Auroral Kilometric Radiation, J. Geophys. Res., 89, 7459, 1984.
- Hecht, E., and A. Zajac, Optics, Addison-Wesley, Reading, 1976.
- James, H. G., Direction-of-Arrival Measurements of Auroral Kilometric Radiation and Associated ELF Data from ISIS 1, J. Geophys. Res., 85, 3367, 1980.
- Kaiser, M. L., and J. K. Alexander, Source Location Measurements of Terrestrial Kilometric Radiation Obtained from Lunar Orbit, Geophys. Res. Lett., 3, 37, 1976.
- Kaiser, M. L., and J. K. Alexander, Terrestrial Kilometric Radiation 3. Average Spectral Properties, J. Geophys. Res., 82, 3273, 1977.
- Kaiser, M. L., J. K. Alexander, A. C. Riddle, J. B. Pearce, and J. W. Warwick, Direct Measurements by Voyagers 1 and 2 of the Polarization of Terrestrial Kilometric Radiation, Geophys. Res. Lett., 5, 857, 1978.
- Kaiser, M. L., and R. G. Stone, Earth as an Intense Planetary Radio Source: Similarities to Jupiter and Saturn, Science, 189, 285, 1975.
- Kraus, J. D., Radio Astronomy, McGraw-Hill, New York, 1966.
- Kurth, W. S., M. M. Baumbach, and D. A. Gurnett, Direction-Finding Measurements of Auroral Kilometric Radiation, J. Geophys. Res., 80, 2764, 1975.
- Mellott, M. M., W. Calvert, R. L. Huff, D. A. Gurnett, and S. D. Shawhan, DE-1 Observations of Ordinary Mode and Extraordinary Mode Auroral Kilometric Radiation, Geophys. Res. Lett., 11, 1188, 1984.
- Melrose, D. B., An Interpretation of Jupiter's Decametric Radiation and the Terrestrial Kilometric Radiation as a Direct Amplified Gyroemission, Astrophys. J., 207, 651, 1976.
- Moran, J. M., Very Long Baseline Interferometer Systems, in Methods of Experimental Physics, ed. by M. L. Meeks, p. 174, Vol 12: Astrophysics, Part C: Radio Observations, Academic Press, New York, 1976.

Weinreb, S., A Digital Spectral Analysis Technique and Its Application to Radio Astronomy, Tech. Rep. 412, Research Laboratory of Electronics, M.I.T., Cambridge, 1963.

Wu, C. S. and L. C. Lee, A Theory of the Terrestrial Kilometric Radiation, Astrophys. J., 230, 621, 1979.